

**MOMENTUM TRANSPORT DUE TO A SQUALL LINE SYSTEM  
OVER THE TROPICAL OCEANS**

by

**CHIA-YUNG CHANG**

B.S., National Taiwan University  
(1981)

Submitted to the Department of Earth,  
Atmospheric, and Planetary Sciences  
in partial fulfillment of the requirement  
for the Degree of

Master of Science  
in Meteorology

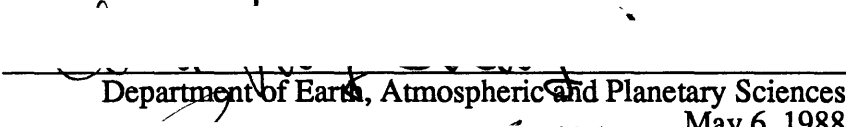
at the

Massachusetts Institute of Technology

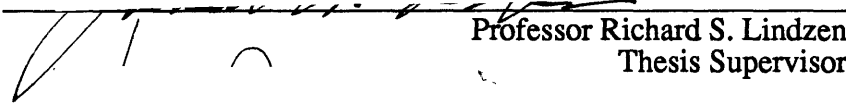
June 1988

© Massachusetts Institute of Technology 1988


Signature of Author

  
Department of Earth, Atmospheric and Planetary Sciences  
May 6, 1988

Certified by

  
Professor Richard S. Lindzen  
Thesis Supervisor

Accepted by

  
Chairman, Departmental Committee on Graduate Students

1 WITHDRAWN  
FROM  
JUL 20 1988  
MIT LIBRARIES  
Lindzen

**MOMENTUM TRANSPORT DUE TO A SQUALL LINE SYSTEM  
OVER THE TROPICAL OCEANS**

by

**CHIA-YUNG CHANG**

Submitted to the Department of Earth,  
Atmospheric, and Planetary Sciences  
on May 6, 1988 in partial fulfillment of the requirement  
for the Degree of Master of Science in Meteorology

**ABSTRACT**

Fast-moving squall lines observed in the tropical oceans are treated as a gravity wave generated by the latent heat release associated with deep cumulus convection. A simple two-dimensional diagnostic linear gravity wave model forced by a zonally propagating heat source is presented. The effect of cumulus friction, or momentum exchange due to cumulus convection, is included in the wave momentum equation. Both monochromatic and localized distributions of precipitation are considered. We will focus on the momentum transport. In the troposphere, within the context of our model, vertical transport of momentum owing to either clouds or gravity waves can be easily separated, whereas above the clouds, only gravity wave transport exists.

It is discovered that, in the cloud layer, for the scales characteristic of squall lines, mean cloud transport is the dominant mean momentum flux contributor. Compared to aircraft observations, our model is able to simulate the mean momentum flux with both the correct sign and magnitude. Within the wave momentum equation, cumulus friction, however, is found not to be a major term.

Above the cloud layer, impacts of these gravity waves due to thermal forcing from below are also inspected. In particular, the amount of energy gets radiated out of the cloud layer on a global scale, the levels where wave breakings occur, and the associated wave-induced acceleration. We find that thermally forced gravity waves are potentially as important as mountain waves (perhaps the most well known and extensively studied gravity waves in the atmosphere) at least in the lower stratosphere. Therefore, when studying the momentum budget of the middle atmosphere, roles played by gravity waves triggered by cumulus convection in troposphere cannot be overlooked.

In addition, our results indicate that only gravity waves forced by localized precipitation are subject to breaking near the tropopause where the static stability of the environment is locally low, and we think this breaking phenomenon is likely to happen in the real atmosphere. However, in terms of the final overall residual momentum flux leaked into the stratosphere, at least for the parameters chosen in this study, both monochromatic and localized precipitation seem to be able to give rise to similar results.

Thesis supervisor: Dr. Richard S. Lindzen

Title: Professor of Meteorology

## **Acknowledgments**

I happily acknowledge that this thesis would not have been possible without the help and the critical suggestions of my thesis advisor, Dr. Lindzen. Discussions with my fellow students, Lorenzo Polvani, Arlindo da Silva, Ron Miller and Wes Ebisuzaki were always encouraging and stimulating.

Finally, I want to thank my adorable wife, Mei-Lin, for her love and support during my years as a graduate student.

## Table of Contents

Title Page .....	1
Abstract .....	2
Acknowledgments .....	4
Table of Contents .....	5
Chapter 1: Introduction .....	7
Chapter 2: Background .....	13
2.1 Precipitating Cloud Systems in the Tropics. ....	13
2.2 Modulation of Precipitation and Convective Activity by the Easterly Wave .....	14
2.3 Momentum Transport by a Squall Line System in the Cloud Layer .....	16
2.4 Impacts of Gravity Waves on the Momentum Budget in the Middle Atmosphere .....	19
Chapter 3: A Gravity Wave Model .....	22
3.1 Physical Aspects .....	22
a. Cumulus parameterization .....	22
b. Determination of basic states and other related profiles .....	24
c. Nature of wave perturbations .....	26
d. Critical levels .....	27
e. Integral constraint on cumulus heating .....	27
f. Distribution of precipitation rate .....	28
g. Determination of phase speed of squall lines .....	31
3.2 Numerical Aspects .....	32
a. Formulation .....	32
b. Boundary conditions .....	37
1) Lower boundary condition .....	37
2) Upper boundary condition .....	41
c. Method of solutions .....	42
3.3 Data .....	50
Chapter 4: Results and Discussions .....	52
4.1 Monochromatic Precipitation .....	52
a. Description of solutions .....	52
1) In the cloud layer .....	52
2) Near the cloud top and/or above the cloud layer .....	54
b. Comparison with previous related studies .....	57
c. Sensitivity tests .....	58
1) Lower boundary condition .....	58
2) Upper boundary condition .....	59
3) Profiles of Q and Mc .....	61
4) Zonal wavelength .....	63
4.2 Gaussian Precipitation .....	64
a. Description of solutions .....	65

1) In the cloud layer .....	65
2) Near the cloud top and/or above the cloud layer .....	67
3) Wave breaking below the cloud top .....	69
b. Sensitivity tests .....	74
4.3 Comparison with Mountain Waves .....	75
Chapter 5: Summary and Conclusions .....	77
Appendix .....	80
A.1 Formulation and solution of the problem .....	80
A.2 Discussion .....	84
References .....	89
Figure and Table Legends .....	97

## Chapter 1: Introduction

Deep cumulus convection has long been recognized as a primary mechanism for transporting the thermodynamic quantities, such as moisture and temperature, vertically. For instance, as first pointed out by Riehl and Malkus (1958), deep cumulus clouds can carry the release of latent heat to the higher troposphere where the local vertical derivative of the moist static energy (defined as  $h = c_p T + gz + Lq$ , every symbol having its conventional meaning) is greater than zero. However, it has recently been agreed that deep convective processes are very important in determining the dynamic budgets in the tropics as well. Stevens (1979) calculated the vorticity, momentum and divergence budgets of synoptic-scale wave disturbances in the tropical eastern Atlantic. He found that each of the large-scale budgets has a significant residual imbalance, suggesting that subsynoptic-scale motions can strongly affect the wave dynamics (provided that errors of measurements are sufficiently small). As a consequence, both thermodynamically and dynamically, there is always an intimate relation between the convective-scale and large-scale motions in the tropics. To gain a better understanding of this relation was the very goal of, for example, GARP Tropical Atlantic Experiment (GATE) during the summer of 1974.

An enormous amount of literature appeared after GATE. Reed et al. (1977) looked at the structure and properties of African waves; Thompson et al. (1979) focused on the easterly waves in the Intertropical Convergence Zone (ITCZ) of the eastern Atlantic; Norquist et al. (1977) studied the energetics and origins of African waves, etc. Two excellent review papers are by Burpee and Reed (1982) concerning the synoptic-scale motions, and by Houze and Betts (1981) on the convection in GATE.

From the papers just mentioned, it is also clear that synoptic-scale is not the only scale of motion observed during GATE. As will be described immediately, the mesoscale cloud line is also one of the features which have drawn researchers' attention.

Cumulonimbi in the tropics frequently organize themselves into larger-scale patterns, mostly lines. Terms such as "squall line" (Zipser, 1977) and "squall line system" (Houze, 1977) are often used to represent those fast-moving cloud lines. In Barnes and Sieckman (1984), a cloud line whose speed relative to the ground is greater than 7 m/s is defined as "fast-moving". Squall lines are found to form ahead of the wave trough of easterly waves in GATE and to move to the vicinity of the next ridge downstream where they dissipate. Squall line passages are associated with violent weather displays such as sudden wind shift and excessive rainfall. Furthermore, squall lines always have the low-level inflow along their leading edge, amplified when they move from the east against low-level equatorial westerlies, finally they eject the air rising in cumulonimbi toward their rear suggesting that they normally move faster than the ambient flow at all heights. Figure 1.1, reproduced from Houze (1977), shows the schematic cross section of a squall line system. Payne and McGarry (1977) studied 46 squall incidents in phase III of GATE; Figure 1.2 depicts their results for the frequency distribution of the location of the leading edge at the beginning and the termination stages of squall lines. Again, it is clear from Figure 1.2 that on the average squall lines move faster than easterly waves.

The temporal and spatial scales of squall lines are less than a day and a few hundred kilometers respectively. Abrupt weather changes are associated with their passages as well. All these properties are evidently characteristic of high frequency gravity waves whose energy may come from the latent heat release when the deep convection occurs



within the system itself. This suggests that we may *model squall lines as a gravity wave phenomenon with a prescribed deep tropospheric thermal forcing due to cumulus convection.*

As was stated earlier, cumulus convection can transport both thermodynamic and dynamic quantities vertically. Nevertheless, less attention has been given to the momentum transport as opposed to the transports of moisture and heat. This is probably attributed to the difficulty of measuring pressure gradients with sufficient accuracy in the tropics. Even among the studies that focused on the momentum transport, most are on the easterly wave-scale which is about an order of magnitude greater than that of squall lines or gravity waves. The major concern in this study, therefore, will be to use a simple gravity wave model to investigate *the momentum transport* associated with a squall line system.

Stevens et al. (1977) and Stevens and Lindzen (1978) showed that the momentum exchange by cumulus convection or the so-called cumulus friction is important on the synoptic-scale easterly wave. Calculations of Rosenlof et al. (1986) indicated that the inclusion of cumulus friction will result in a more reasonable simulation of the Walker circulation. Stevens and Lindzen (1978) also demonstrated that the same physical process might not be essential for gravity waves. However, we do have reasons, which will be stated later on, to doubt this conclusion since a larger precipitation rate would usually accompany squall lines and thus increase the effect of cumulus friction. It follows that a more detailed examination is needed.

Some aircraft measurements of the mean momentum flux<sup>1</sup> by convective cloud lines have been made by LeMone (1983) and LeMone et al. (1984). Using the squall line

---

<sup>1</sup> Implicitly, the observed momentum flux contain contributions from both the cumulus convection and gravity waves.

coordinate system which is fixed to the earth with  $x$ - (and  $u$ -) axis being normal to the line, positive in its direction of movement (Figure 1.3), they found out that the sign of  $\overline{u'w'}$  is mostly negative regardless of the sign of  $\partial\bar{u}/\partial z$ . In other words, the upward motions in cloud lines always transport horizontal momentum against the direction toward which the lines are propagating. We are curious whether a simple model can generate results that are consistent with observations. Because squall lines are treated as a gravity wave phenomenon, there is, in addition to the explicit cumulus momentum transport, also gravity wave flux. Nonetheless, what one obtains from the data is always the combination of these two components. Given the fact that in the observational studies, no explicit attempt to separate the wave from the cloud contribution have been made, it remains unclear which component is the main flux contributor. With the aid of the model presented here, an answer to this problem can be provided.

Away from the cloud layer, the vertical flux of horizontal momentum due to cumulus clouds will vanish by definition, but the flux due to gravity waves continues to exist. Eliassen and Palm (1961) showed that in the absence of damping, forcing, and critical levels, the vertical momentum flux associated with wave perturbations is non-divergent, and there is no interaction between waves and the ambient flow. Since density decreases approximately like  $\exp(-z/H)$  with height,  $H$  being the scale height, each wave field grows like  $\exp(z/2H)$  in the cloud-free region (ignoring the effects of wind shear and variable static stability). An unstable breakdown of these waves will arise eventually and any further growth of wave amplitudes will be prevented by the generation of turbulence (Lindzen, 1981, 1988). It should be added that magnitudes of wave fields are a function of not only the density stratification, but also the value of  $|c - \bar{u}|$ , where  $\bar{u}$  is the flow speed and  $c$  is the phase speed of the wave. Hence, wave breaking amplitudes can occur with  $\bar{u}$

approaching  $c$  which is still an amplitude factor. When breaking occurs, the Eliassen-Palm theorems are violated and waves will deposit the momentum they were carrying into the mean flow, thus exerting drag or acceleration on the mean flow.

It has been recognized that vertically propagating internal gravity waves play a very important role in the dynamics of the middle atmosphere. One of the examples is that the breaking gravity wave-induced acceleration on the mean flow can provide an explicit source of "friction" needed to reverse the mesospheric wind shear, and to reverse the pole-to-pole temperature gradient at the mesopause according to the thermal wind relationship. Sources of atmospheric gravity waves can be orography, unstable shear zones, geostrophic adjustment, convection, etc. Most of the studies to date emphasize stationary waves attributed to orography (e.g. Klemp and Lilly, 1980; Palmer et al., 1986; Tanaka, 1986; McFarlane, 1987), very little has been mentioned concerning gravity waves triggered by convective complexes. Therefore, as these gravity waves of convective origin propagate upward, questions such as how much momentum flux can be carried into the middle atmosphere, at which level does the unstable breakdown occur subject to different mean flow profiles, and how much is the wave-induced acceleration are certainly worth investigating. It is hoped that results from this study can help us to understand more about the potential roles played by these waves, even though the direct observations are yet to be made.

To summarize, in this study, squall lines will be treated as thermally forced gravity waves, and the momentum transport in *both the troposphere and middle atmosphere* will be stressed. The purpose of the study is to address issues such as the importance of cumulus friction, the determination of the dominant component of the mean momentum transport within a squall line system, and the roles played by thermally forced gravity

waves in the middle atmosphere. In Chapter 2, the background of this study is given. Chapter 3 is devoted to describing a simple gravity wave model. Results are presented in Chapter 4. Finally, conclusions and some implications will be discussed in Chapter 5.

## **Chapter 2: Background**

### **2.1 Precipitating Cloud Systems in the Tropics.**

Precipitating clouds in the tropics occur at scales ranging from small isolated cumulus clouds to large cloud clusters. Cloud clusters are identified in satellite imagery by their mesoscale cirrus shields, each shield being ~100 to 1000 km. Cloud clusters generally have lifetimes of a day or less. Although the spatial spectrum of clouds is log-normal distributed (Houze and Betts, 1981), owing to their size, cloud clusters dominate the mean cloudiness and precipitation over the tropics. Studies using radar and aircraft show that tropical cloud clusters are often composed of several mesoscale precipitation features, also called the mesoscale convective cloud lines.

Cloud clusters in the tropics generally can be classified into two types: squall and nonsquall clusters. Squall clusters are associated with squall lines with rapid propagation (~10 - 15 m/s relative to the ground), explosive growth and the distinct oval leading edge. Nonsquall clusters tend to travel more slowly (< 3 m/s) and do not possess notable cirrus shield or the oval leading edge. However, despite the travelling speed and the outside appearance, these two types of cloud clusters, especially in GATE, exhibit strong similarities in other aspects of their structures. In Table 1 of Houze and Betts (1981), a fairly complete list of case studies of convective events during GATE was given.

Although nonsquall clusters are not as dramatic as squall clusters, on account of their sheer number, they are the predominant type of cloud clusters in the tropics. To a

first approximation, we are going to assume that *half* of the precipitation in the tropics is attributable to squall clusters. This assumption will enable us to estimate the global impact of squall clusters on the middle atmosphere.

In the composite study by Barnes and Sieckman (1984) using GATE data, mesoscale cloud lines are further classified into three groups according to their speed (relative to the ground)  $V_L$ : 1) slow-moving ( $V_L < 3$  m/s), 2) intermediate-moving ( $3 \text{ m/s} \leq V_L \leq 7 \text{ m/s}$ ) and 3) fast-moving ( $V_L > 7$  m/s). Fast moving lines are located to the west of the trough of easterly waves, moving toward the west at 11-14 m/s (with mean speed of 11.1 m/s), while the slow-moving lines are located to the east of the trough and moving eastward to southeastward at 2-3 m/s (with mean speed of 2.2 m/s).

As will be described later on, a simple two-dimensional gravity wave model is adopted in this study. Such a model is more suitable to the fast-moving cloud lines. Compared to slow-moving lines, fast-moving lines are relatively well organized, more or less move in the zonal direction, and thus more properly described by this simple model.

## **2.2 Modulation of Precipitation and Convective Activity by the Easterly Wave**

After GATE experiment, many studies (e.g. Reed et al., 1977, and Thompson et al., 1979) showed that over west Africa and the eastern Atlantic, convection<sup>1</sup> was most intense just before or at the time of the synoptic-scale wave trough passage at

---

<sup>1</sup> The convective activity mentioned here was primarily determined by the percentage cover by convective cloud defined as the white-appearing cloud in the satellite infrared images.

700 mb; while the least amount of convection occurred in advance of or at the ridge. In particular, such modulation of convection by synoptic-scale waves was most significant during phase III of GATE.

As pointed out by Thompson et al. (1979), from both the sensible heat and moisture budgets, the modulation of convective activity and precipitation by easterly waves is clearly attributed to the variation in the large-scale divergence, convergence and vertical motion fields, rather than to the thermodynamic instability. This is consistent with what was discovered by Cho and Ogura (1974) for the Reed-Recker (Reed and Recker, 1971) composite easterly waves over the equatorial western Pacific. As far as precipitation and convective cloudiness are concerned, a close positive correlation was also found; although the former generally leads the latter by a few hours indicating the spreading of the cirrus shield beyond the time when the activity of deep convection is at a maximum (Leary and Houze, 1979).

Owing to the apparent relationship between the convective activity and synoptic-scale motions, we will concentrate on squall lines that exist in the convergent phase of easterly waves. A clear scale separation between the squall line and the convergent phase of the easterly wave will also be assumed so that *the former will "see" the latter as its "basic state"*.

Finally, near the trough region, it is found that the radiative cooling ( $\sim 1$  °C/day) is small compared to the large-scale apparent heat source ( $\sim 10$  °C/day), and the surface evaporation ( $\sim 4$  mm/day) is also smaller than the precipitation ( $\sim 20$  mm/day) (Thompson et al., 1979). Strictly speaking, the above statements were all based on the budget

studies on the easterly wave scale. However, when formulating the gravity wave model, we shall subsequently neglect both the radiative cooling and the surface evaporation (see Chapter 3 for more details).

## 2.3 Momentum Transport by a Squall Line System in the Cloud Layer

Schneider and Lindzen (1976) derived a representation of cumulus friction (or the momentum exchange by cumulus convection). In particular, the effect of the momentum flux due to cumulus clouds on the large-scale momentum equation can be expressed as:

$$\rho \overline{u'w'} = M_c(u_c - \bar{u}), \quad \rho \overline{v'w'} = M_c(v_c - \bar{v}) \quad (2.1)$$

where the overbar denotes the large-scale average, the prime is the deviation (caused by the presence of cumulus clouds) from the average,  $M_c$  is the cloud mass flux,  $\bar{V} = (\bar{u}, \bar{v})$  is the large-scale horizontal velocity vector, and  $\bar{V}_c = (u_c, v_c)$  is the horizontal velocity vector within convective clouds. In order to derive (2.1), it has been assumed that the fractional area occupied by clouds is much smaller than unity. As a matter of fact, Ooyama (1971), Yanai et al. (1973) and Arakawa and Schubert (1974) have derived expressions similar to (2.1) to represent the sensible heat and moisture fluxes due to cumulus convection:

$$\rho \overline{s'w'} = M_c(s_c - \bar{s}), \quad (2.2)$$

$$\rho \overline{q'w'} = M_c(q_c - \bar{q}), \quad (2.3)$$

where  $s$  is the dry static energy and  $q$  is the mixing ratio of liquid water.

Since most of the mass flux within deep cumulus clouds originates at the cloud base, and the ascent of air parcels in clouds is rapid enough such that the pressure



gradient force does not have enough time to operate on the cloud-scale momentum, Schneider and Lindzen (1976) then suggested that  $\bar{V}_c$  is close to a conserved quantity and can be approximated by  $\bar{V}$  at the cloud base. Results obtained by Soong and Tao (1984) using a two-dimensional cloud ensemble model showed that the parameterization scheme of Schneider and Lindzen (1976) is basically correct but needs some improvements. One of the improvements is to take the entrainment effect into account in order to have a better evaluation of  $\bar{V}_c$ . In fact, in an earlier paper, Shapiro and Stevens (1980) have suggested that the momentum entrainment/detrainment rate be replaced by the mass entrainment/detrainment rate; but Cho (1985) showed that this probably incorrect. Flatau and Stevens (1987) also estimated the effect of convection-generated pressure forces on the horizontal momentum in clouds, they found that such effect is influential, especially for slow-moving lines. Because we have not come to a full knowledge of the properties of  $\bar{V}_c$ , and also for the ease of calculations, it will be assumed that  $\bar{V}_c$  is still an approximately conserved quantity.

Cumulus friction is obtained by taking the vertical derivative of (2.1), i.e.

$$\bar{F}_c = \frac{1}{\rho} \frac{\partial}{\partial z} [M_c(\bar{V} - \bar{V}_c)]. \quad (2.4)$$

Stevens et al. (1977) showed that cumulus friction is an important physical process which has to be taken into account in the perturbation momentum equation in order to simulate tropical synoptic-scale motions correctly. In a later paper, Stevens and Lindzen (1978) concluded that the same physics may not be important for high frequency gravity waves such as squall lines. However, this needs reexamination since more precipitation normally accompanies squall lines and the importance of cumulus friction will be increased. This can be explained in the following way: suppose we decompose the large-scale variables into a mean plus a wave perturbation, then, on the

right hand side of the perturbation momentum equation, the term representing cumulus friction is:

$$\frac{1}{\rho} \frac{\partial}{\partial z} [\overline{M}_c(u' - u'_c) + M'_c(\overline{u} - \overline{u}_c)]. \quad (2.5)$$

Note that the overbar and prime now denote the mean and the wave perturbation respectively. In some sense, the *time scale* of cumulus friction ( $\tau_c$ ) can be defined as  $\rho(\partial \overline{M}_c / \partial z)^{-1}$ , and this is to be compared with the time scale for the wave ( $\tau_w$ )  $L/2\pi/(c - \overline{u})$ ,  $L$  and  $c$  being the wavelength and phase speed of the wave. When  $\tau_c/\tau_w \gg 1$ , cumulus friction is negligible; but obviously, an increasing precipitation or cloud mass flux will result in a decrease in  $\tau_c/\tau_w$ .

LeMone (1983) first analyzed the mean momentum transport by one of the cloud lines observed during GATE. However, this line was a slow-moving one with speed equal to 3.0 m/s and toward the east. LeMone showed that the mean vertical transport of horizontal momentum normal to the cloud line ( $\overline{u'w'}$ ) is not successfully predicted by the traditional mixing length theory which requires that the direction of the eddy momentum flux is always down the gradient of the environmental wind profile ( $\partial \overline{u}/\partial z$ ). On the contrary, the cloud line transports the component of horizontal momentum parallel to its axis ( $\overline{v'w'}$ ) down the gradient of the environmental wind profile ( $\partial \overline{v}/\partial z$ ). LeMone also concluded that the mean momentum transport is mainly achieved by convective cores which occupy roughly 25% of the convectively active zone.

LeMone et al. (1984) further documented nine convective lines (both fast- and slow-moving) during GATE and the emphasis was placed on those cases which exhibited quasi-two-dimensional structure. Their results indicated that for quasi-2D lines, upward motions are systematically carrying front-to-rear momentum, where

"front" is defined as the direction toward which the line is moving. If expressed in terms of the convective line coordinate system as the one shown in Figure 1.3, the front-to-rear momentum transport ( $\overline{u'w'}$ ) just mentioned is then consistently negative. On the other hand, as discovered in LeMone (1983), transport of momentum parallel to the convective line axis is well explained by the traditional mixing length theory. Furthermore, the momentum flux is shown to be mostly attributable to convective (kilometer scale) updrafts originating from the undisturbed mixed layer ahead of the convective line. From what is implied by the GATE data, the contribution from downdrafts is unimportant. Finally, under the same normalization method, the magnitude of  $\overline{u'w'}$  for fast-moving lines is found to be about an order of magnitude larger than that for slow-moving lines.

It should be pointed out that the observed mean momentum flux in the aforementioned studies includes contributions from both cumulus clouds and gravity waves, any direct indication concerning the major contributor to the mean momentum transport is still in need. Given the simple model presented here, however, the separation of the cloud transport from the wave transport becomes possible.

## **2.4 Impacts of Gravity Waves on the Momentum Budget in the Middle Atmosphere**

It has been recognized that vertically propagating gravity waves play a significant role in the dynamics of the middle atmosphere through wave breaking or dissipation. In his seminal paper, Lindzen (1981) developed a theory to parameterize the turbulence and stress owing to the breakdown (or saturation) of gravity waves and atmospheric tides. The theory was refined by a series of later papers (Lindzen, 1984, 1988). It is

assumed that once the amplitude of waves becomes so large that the total (mean plus waves) temperature lapse rate is convectively unstable, waves will break and the subsequent generation of eddy diffusion will act to eliminate further growth in wave amplitude.

Following Lindzen (1981), there are numerous other studies concerning the gravity wave breaking effect on the mesospheric circulation (e.g. Holton, 1982, 1983; Holton and Zhu, 1984) together with some observational and diagnostic studies (e.g. Hamilton, 1983; Smith and Lyjak 1985) to support the theory.

There is now also an increased interest in the possible influence of the gravity wave breaking on the *stratospheric* and *tropospheric* circulation. Lilly (1972) noted the removal of the energy and momentum from the troposphere and lower atmosphere by the breaking of large amplitude mountain lee waves may be a significant factor in the evolution and maintenance of the large-scale atmospheric circulation. In Tanaka and Yamanaka (1985), the influence of the mesoscale mountain wave breakdown on the general circulation of the lower stratosphere is studied. Lindzen (1985) suggested that waves break in the mesosphere might have collapsed in the upper troposphere or lower stratosphere already, and this primary wave breaking serves as a filter to set a constraint on the maximally allowed wave amplitude in the atmosphere higher above. Mahlman and Umscheid (1984) found that successful stratospheric circulation simulation can be obtained by including smaller scale gravity waves. McFarlane (1987) also concluded that large-scale momentum sinks resulting from breaking mountain waves play a very important role in determining the structure of the general circulation of the lower stratosphere and the troposphere.

Orography, as we all know, is not the only mechanism which is capable of exciting internal gravity waves. In fact, both Holton (1982) and Matsuno (1982) suggested considering a spectrum of gravity waves (i.e. different phase speeds) in order to reasonably simulate the mesospheric general circulation. Other possible sources of gravity waves include unstable shear zones (Kelvin-Helmholtz instability), geostrophic adjustment and the development of convective complexes and squall lines.

As described earlier, squall lines can be viewed as gravity waves forced by an internal heat source due to the release of latent heat. Except for the form of the forcing function (internal vs. boundary) and the lower boundary condition of course, thermally forced gravity waves are really not physically different from waves forced by orography. However, most studies are for gravity waves having orographic origin, and thus far very little has been done concerning gravity waves triggered by thermal forcing. It is hoped that results of this analysis will provide some insights into the potential roles played by thermally forced gravity waves.

## Chapter 3: A Gravity Wave Model

### 3.1 Physical Aspects

#### *a. Cumulus parameterization*

Following Yanai et al. (1973), the large-scale (for the present case the scale characteristic of squall lines) heat source ( $Q$ , in  $^{\circ}\text{C}/\text{day}$ ) is:

$$\rho c_p Q = \rho \left( \frac{\partial \bar{s}}{\partial t} + \bar{V} \cdot \nabla \bar{s} + \bar{w} \frac{\partial \bar{s}}{\partial z} \right) = L(\bar{c} - \bar{e}) - \frac{\partial}{\partial z} \rho \overline{w' s'} + Q_R \quad (3.1)$$

where the overbar denotes the average over the cloud and non-cloud area, the prime stands for the deviation from the average,  $s = c_p + gz$  the dry static energy,  $L$  the latent heat of condensation of water substance,  $c$  the rate of condensation,  $e$  the rate of re-evaporation of cloud droplets,  $Q_R$  the radiative cooling rate, and the eddy term is due to the convergence of the cloud heat flux. The aim of the cumulus parameterization is to represent the right hand side of (3.1), except  $Q_R$ , in terms of large-scale variables. In order to achieve this task, assumptions have to be made.

Arakawa and Schubert (1974) suggested a cloud ensemble which is steady, entrains continuously but detrains only when the cloud loses its buoyancy at the cloud top.  $Q$  in (3.1) for this cloud ensemble can then be expressed as follows:

$$\rho c_p Q = M_c \frac{\partial \bar{s}}{\partial z} + D(s_D - \bar{s} - Ll_D) + Q_R \quad (3.2)$$

where  $s_D$  is the detrained static energy,  $D$  the rate of detrainment,  $l_D$  the detrained liquid water and  $M_c$  the cloud mass flux. One of major assumptions used to derive

(3.2) is that the fractional coverage area for clouds being very small. After further considering only the cumulus heating, assuming the cloud field is composed only of non-entraining deep clouds, and neglecting the re-evaporation of detrained liquid water<sup>1</sup>, Arakawa and Schubert (1974) showed that (3.2) can be further simplified as:

$$\rho c_p Q = M_c \frac{\partial \bar{s}}{\partial z}. \quad (3.3)$$

In this study, we will require that the cloud mass flux, the cumulus heating and the static stability satisfy (3.3). In other words, we cannot specify all three fields independently of one another.

Although for the time scale of squall lines, radiative cooling is not important, we have to remember, however, that in the long term only radiative cooling can balance the cumulus heating (Sarachik, 1985).

One might choose  $M_c$  to be constant in the vertical<sup>2</sup> as a first step. At the cloud top, in order for the heat flux to be continuous,  $Q$  has to vanish, from (3.3) this will then lead to a vanishing local static stability. However, by means of a simple cumulus parameterization scheme (Lindzen, 1981, 1988), we are able to determine profiles of  $M_c$  and  $Q$  which approach zero continuously; hence, such a severe constraint will not be imposed on the static stability. Nevertheless, data from both

---

**1** As implied by Yanai et al. (1973) and suggested by Sarachik (1985), the re-evaporation might be important for trade cumulus clouds. However, in this study, the re-evaporation of deep cumulus clouds will not be included.

**2** Physically this means that only air parcels originating from the lowest layer which has the highest moist enthalpy ( $h = s + Lq$ ) get entrained, and they do not detrain in the depth of the troposphere until the cloud top is reached.

Thompson et al. (1979) and Oort (1983) showed that in the tropical upper troposphere, the static stability is indeed relatively low; if expressed in terms of  $(1/c_p)(\partial\bar{s}/\partial z)$ , it is  $\sim 1$  to  $2$  °C/km.

As was just mentioned, a scheme first proposed by Lindzen (1981, 1988) will be used to parameterize profiles of  $M_c$  and  $Q$ . For the sake of illustration, we first divide the whole atmosphere into a sum of individual layers, and the total effect on the large scale variables can be expressed in terms of the sum of contributions of clouds having their roots at different layers. Following Lindzen (1981, 1988), each of these clouds has a very simple structure; it entrains only from its root layer ( $z_i$ ) which is supposedly below the trade wind inversion, detrains only when it loses its buoyancy at  $z_j$  where  $h(z_i) = s(z_j)$ , and the mass converged for one of the entraining layers,  $\delta(\rho w)$ , will give rise to a fraction of the contribution,  $\delta(M_c)$ , to the total cloud mass flux between  $z_i$  and  $z_j$ . This scheme is evidently much simpler than the one suggested by Arakawa and Schubert (1974); but is found by Geleyn et al. (1982) to have a better performance in the large-scale numerical forecast models.

### ***b. Determination of basic states and other related profiles***

On account of a clear modulation of convective activity and precipitation by easterly waves, we will treat the *convergent phase* of easterly waves as the *basic state* for squall lines. During the course of the calculation, all the prescribed basic state profiles such as mean zonal flow and mean vertical velocity will be those characteristic of the convergent phase of easterly waves.



Sarachik (1985) and Lindzen and Nigam (1987) have pointed out the importance of the relatively well mixed tropical trade cumulus layer. However, conventional meteorological measurement procedures, like those used in the Marshall Islands tests and GATE experiments, do not have vertical resolution high enough to resolve this kind of the planetary boundary layer structure. As a result, we deliberately replaced the profile of the static stability for the lowest 2 to 3 km by the trade cumulus layer measurements obtained by Augstein et al. (1974) from the Atlantic Tropical Experiment (ATEX). It is clear from (3.3) that little cumulus heating should exist for the first 2 to 3 km of the atmosphere, as a consequence.

As pointed out by Houze (1982), there is in fact a difference between the *convective* and *mesoscale* heating. The mesoscale component can be referred to as that part of the tropical cloud system which contains the mesoscale anvil circulation (cf. Fig. 1.1), while convective component consists of contributions from cumulus elements ranging from deep cumulonimbi to shallow cumulus clouds. Since the cumulus parameterization scheme used here has not really taken into account the mesoscale anvil circulation, only the heating due to deep cumulus clouds has really been parameterized.

From a practical point of view, we need to specify profiles of temperature, mixing ratio, mean zonal flow and mean vertical velocity (which is itself not directly observed but implied from the horizontal convergence field) before any calculation is performed. The static stability is calculated from the temperature profile. We then use the scheme described in the previous section together with the mean vertical velocity profile to parameterize the cloud mass flux ( $M_c$ ), and cumulus heating ( $Q$ ) (viz. (3.3)). Strictly speaking, profiles of  $M_c$  and  $Q$  thus

obtained are only representative of the basic state (synoptic-scale); however, for simplicity, we shall assume that in terms of mesoscale wave perturbations, both  $M_c$  and  $Q$  have the same distributions<sup>1</sup>.

### *c. Nature of wave perturbations*

We focus on steady wave trains; instability is not considered. Moreover, wave amplitudes are assumed to be small enough such that the dynamics is basically linear. This assumption is valid at least for the synoptic-scale waves (Stevens, 1979); its validity concerning gravity waves can be verified after solving the mesoscale wave fields.

Previous studies such as Davies (1979) and Xu and Clark (1984) have pointed out the importance of the finite adjustment time of clouds to the low level convergence for the wave-CISK calculation. In another related paper, Bolton (1980) also showed that in order for instability to occur, cumulus heating and the vertical velocity field cannot be in phase. Since a diagnostic rather than an instability analysis is of interest at present, the possible time lag between the low level convergence field and the cloud activity is not important. In other words, no time lag between  $w$  and  $M_c$  (and  $Q$ ) is assumed to exist.

---

<sup>1</sup> In principle, profiles of  $M_c$  and  $Q$  for the mesoscale wave perturbation, within the context of the cumulus parameterization scheme adopted here, are not known prior to solving the perturbation vertical velocity field. Hence, one can start with initial guesses of  $M_c$  and  $Q$ , solve for  $w$ , reparameterize  $M_c$  and  $Q$ , etc., until  $M_c$  and  $Q$  are completely consistent with  $w$ . However, such iteration process is not guaranteed to converge and is out of the scope of this simple diagnostic study. Nonetheless, one is able to check *a posteriori* whether the prescribed profiles of  $M_c$  and  $Q$  for the wave perturbation are far from being consistent with  $w$ . It turns out that the consistency is roughly achieved, thus the specification of  $M_c$  and  $Q$  profiles is justified.

Finally, it is also postulated that there is no vertical tilt of cumulus heating, thus the vertical structure of cumulus heating is represented by a real function.

#### *d. Critical levels*

We shall assume that no critical level, where the phase speed of the wave equals to the mean flow, is encountered. In the troposphere, observations show that this criterion is usually met because squall lines normally propagate faster than the mean flow (Barnes and Sieckman, 1984).

It is well known that the mean zonal flow in the lower tropical stratosphere alternates between the easterly and westerly regimes with a period from 24 to 30 months and an amplitude of about 20 m/s. This phenomenon is known as the quasi-biennial oscillation (Lindzen and Holton, 1968; Holton and Lindzen, 1972). From the work of Booker and Bretherton (1967), the existence of a critical level will result in almost total absorption of vertically propagating waves. Therefore, owing to this filtering process in association with the mean zonal flow, only under favorable conditions (namely the nonexistence of the critical level) can gravity waves excited in the troposphere manage to escape into the middle atmosphere.

#### *e. Integral constraint on cumulus heating*

We require that the net cumulus heating ( $Q$ ) due to the net precipitation ( $P$ ) satisfies the following integral constraint,

$$\int_{z_c}^{z_t} \rho c_p Q dz = L_v P, \quad (3.4)$$

where  $z_c$  and  $z_t$  denote levels of the cloud base and cloud top, and  $L_v$  is the latent heat of condensation. Therefore, after obtaining profiles of  $M_c$  and  $Q$  by the cumulus parameterization scheme, their magnitudes are then normalized according to a specified precipitation rate.

#### *f. Distribution of precipitation rate*

Both monochromatic and localized precipitation will be used in this study.

First, consider the case of monochromatic waves. Figure 3.1 shows the distribution of precipitation as a function of easterly wave category<sup>1</sup> during phase III of GATE (Thompson et al., 1979). It is clear that on the synoptic-scale the distribution of rainfall is close to a single wave train superimposed on a constant basic state whose precipitation magnitude is equal to that associated with the wave perturbation amplitude. On the mesoscale, in a similar manner, we assume that a monochromatic precipitation will be superimposed on a basic state (i.e. the convergent phase of easterly waves) whose magnitude ( $\bar{P}$ ) is equal to that associated with the wave perturbation ( $P'$ ). Owing to the fact that the "total" precipitation is always positive, the requirement of no "negative" clouds will then no longer introduce any harmonic distortion.

Figure 3.2 is used to illustrate our viewpoint just described. In that figure, two scales of motions are presented. The first one is the synoptic-scale easterly wave, in which case the ITCZ serves as its basic state. The second one is the mesoscale gravity wave, with the convergent phase of the easterly wave serving as its basic

---

<sup>1</sup> Refer to the legend of Figure 1.3 for the definition of easterly wave category.

state. From Figure 3.2, it seems that the amplitude of the mesoscale perturbation precipitation should be equal to 2.4 cm/day (the zonal variation of  $\bar{P}$  will be ignored due to the relatively short spatial scale of squall lines compared to that of the convergent phase of easterly waves). However, the fact that the average precipitation which is about 1.2 cm/day over the ITCZ where most of easterly waves are observed is only a result of a long term average, in which case the appearance of the ITCZ is "blurred" into a broader band. We think that at any particular moment, the extent of the ITCZ should be narrower and a more intense rainfall rate should be associated with it. Therefore, a monochromatic precipitation with amplitude equal to  $2 \cdot 2.4 = 4.8$  cm/day will be assumed in this study.

Although the choice of the amplitude of the precipitation has been made somewhat subjectively, we can nevertheless conduct a test to see whether it is reasonable or not. Houze (1977) studied the structure and dynamics of the 4-5 September 1974 tropical squall line system. According to his definition, a "squall line system" refers to the entire disturbance consisting of the line of cumulonimbus clouds and the trailing anvil cloud region. The large-scale area encompassing the system is typically  $10^5$  km<sup>2</sup>, and  $4.6 \cdot 10^{12}$  kg of total water fell during its lifetime (0900 9/4/74 - 0800 9/5/74). After a simple calculation, the average precipitation for such a system is incidentally also 4.8 cm/day. Hence, we feel that the choice of 4.8 cm/day is at least not too far from reality.

The slow and moderate speed cloud lines are a few hundred km long and 50-100 km wide (active convective region plus stratiform region), while the

fast-moving ones have similar lengths but with widths extending up to 250 km. If we were to approximate cloud lines with gravity waves, given the typical width of 100 km for squall lines, a wavelength equal to 200 km seems plausible.

The monochromatic wave is by no means a correct description of the precipitation. In a typical squall line system, there is a convective region of intense, cellular precipitation and a mesoscale region of lighter, horizontally uniform rain. In the case studied by Houze (1977), 60% of precipitation falling over the convective region and 40% over the mesoscale region. The mesoscale rain can be generated in two ways: 1) water is first condensed in the convective region and subsequently incorporated (mostly by advection) into mesoscale region, and/or 2) water is simply generated by the mesoscale lifting itself. For simplicity, we shall adopt the first case, hence all the latent heat should have been released in the much localized convective region.

In the following calculation, whenever a localized precipitation is under consideration, a Gaussian distribution  $P_0 \cdot \exp[-(x/x_0)^2]$  will be used with  $x_0=10$  km and  $P_0=60$  cm/day. The choices of  $x_0$  and  $P_0$  were inferred from the idealized mesoscale cloud system by Leary and Houze (1980). It should be pointed out that from the five GATE cases studied by Leary and Houze (1979), precipitation rates ranging from 20 to 200 cm/day for the convective region were all observed; hence  $P_0=60$  cm/day is like a geometric mean. Considering a hypothetical domain of 200 km (equal to the wavelength of the monochromatic wave), the Gaussian rainfall chosen here corresponds to a mean precipitation of 5.3 cm/day which is not too different from 4.8 cm/day for the monochromatic precipitation.

### *g. Determination of phase speed of squall lines*

During GATE, both fast- and slow-moving mesoscale convective cloud lines were observed, and the term "squall line system" is referred to the fast-moving ones. Barnes and Sieckman (1984) showed that fast-moving lines typically move east to west at an average speed of 11 m/s. However, if we are concerned with the amount of the radiation out of the cloud region, a range of phase speed should be taken into account (see Appendix). It is thus assumed in our model that the phase speed of squall lines or gravity waves is 10 ~ 13 m/s toward west. Given the phase speed at this range and wavelength of 200 km, the Doppler-shifted period of the wave is about 10 hr which is quite typical for the lifetime of squall line systems.

The range of the phase speed chosen here is suggested not only by observations, but also by the wave-CISK theory (Lindzen, 1974). According to the wave-CISK theory, in order for the gravity wave to maximize the low level convergence that is supposed to take place within the trade cumulus layer, one quarter of the gravity wave's vertical wavelength ( $L$ ) should be approximately equal to the depth of trade cumulus layer which is about 2~3 km. From the simple dispersion relationship for gravity waves,

$$\left(\frac{2\pi}{L}\right)^2 = \frac{N^2}{(c - \bar{u})^2},$$

and the mean zonal wind profiles used in this study, phase speeds are also found roughly in the range of 10 ~ 13 m/s.

## 3.2 Numerical Aspects

### *a. Formulation*

Since the structure of squall lines is essentially two-dimensional, and the local pendulum day is much longer than the time scale of squall lines, the gravity wave model will be two-dimensional ( $x$ - $z$ ) and on a non-rotating frame. Each field is decomposed as usual into a mean (overbarred quantity) plus a wave perturbation (primed quantity). Log-pressure coordinates will be used (Holton, 1979). The linearized governing equations in the cloud layer,  $z \in (z_c, z)$ , for the hydrostatic gravity wave around a rather general basic state (only varies with height) with cumulus friction being taken into account (viz. section 1.3) are:

$$\frac{du'}{dt} + \bar{w} \frac{\partial u'}{\partial z} + w' \frac{d\bar{u}}{dz} = -\frac{\partial \phi'}{\partial x} + \frac{g}{P_0} e^z \frac{d}{dz} [\bar{M}_c (u' - u_c') + M_c' (\bar{u} - \bar{u}_c)] + \nu \frac{\partial^2 u'}{\partial z^2}, \quad (3.5a)$$

$$\frac{\partial u'}{\partial x} + \frac{\partial w'}{\partial z} - w' = 0, \quad (3.6a)$$

$$\frac{dT'}{dt} + w' \Gamma = Q', \quad (3.7a)$$

$$\frac{1}{R} \frac{\partial \phi'}{\partial z} = T', \quad (3.7b)$$

The equations above are the momentum equation, continuity equation, thermodynamic or heat equation, and hydrostatic equation respectively, where

$$z = -\ln(p/p_0),$$

$$p = \text{pressure (mb)},$$

$$p_0 = 1000\text{mb},$$



$w$  = vertical velocity in the log-pressure coordinates,  
 $u$  = horizontal velocity,  
 $T$  = temperature,  
 $\phi$  = geopotential height,  
 $M_c$  = cloud mass flux,  
 $u_c$  = horizontal momentum characteristic of clouds (=constant),  
 $Q$  = cumulus heating,  
 $\nu$  = eddy viscosity = 0.1 m<sup>2</sup>/sec (in the geometric coordinates),  
 $\Gamma = (d/dz + R/c_p)T$ , and  
 $\hat{d}/dt = \partial/\partial t + \bar{u}(\partial/\partial x)$ .

When cumulus friction is included in the model, one may think that since the mean cloud activity ( $\bar{M}_c$ ) comes from the low level convergence which is associated with the mean vertical velocity ( $\bar{w}$ ), it will be inconsistent to consider only one of them as part of the basic state while ignoring the other one. This statement is in fact not strictly true. Following Yanai et al. (1973) and Arakawa and Schubert (1974), one can always partition the large scale variable into the cloud and the environmental (cloud free) contributions. For instance, the large scale vertical mass flux can be written as:

$$\rho w = M_c + \tilde{M}$$

where  $M_c$  and  $\tilde{M}$  denote contributions from the cloud and the cloud-free environment respectively. Considering the mean part (i.e. average over the convergent phase of easterly waves) of the equation above, as one can see, on account of the contribution from the environment, the presence of  $\bar{M}_c$  does not really guarantee the existence of  $\bar{w}$ . If  $\bar{w}$  is omitted from the basic state, what follows is that although no low level convergence takes part in the convection, *surface evaporation* will in turn play an

active role in supplying the moisture. Therefore,  $\overline{M}_c$  and  $\overline{w}$  do not have to be coexistent simultaneously. True, but nevertheless, as we have stated in section 2.2, contribution from the surface evaporation is negligible compared to the precipitation at least for scales smaller than easterly waves. As a consequence, in the following calculation, *if cumulus friction were to be taken into account, we will treat  $\overline{M}_c$  as being attributed completely to low level  $\overline{w}$* , contribution from the surface evaporation will be ignored. This point proves to be important in the later discussion.

The inclusion of the eddy diffusion term in (3.5a) is for the sake of removing an inherent singularity for the system (3.5a)-(3.7a). Without the eddy diffusion term, the system (3.5a)-(3.7a) can be consolidated into a single third order<sup>1</sup> ordinary differential equation for one of the variables. However, according to the way that cumulus parameterization works (see section 3.1.a), in the lowest 2 to 3 km of the atmosphere,  $\overline{w}$  is balanced by  $A\overline{M}_c$  exactly in (3.5a). What follows then is a decrease of the order of the system and a singularity problem arises. If the singularity only occurs at one point, we probably can get around with this with a local analysis by expanding the solution in terms of a Frobenius series around the singular point (Bender and Orszag, 1978); however, what is involved at present is a region rather than a point. In order to have a smooth transition from the lower region where  $A\overline{M}_c = \overline{w}$  to the higher region, it is convenient to include an eddy diffusion term of momentum so as to raise the order of the system from three to four, the problem of singularity is then solved naturally. In the following calculations, the value of eddy viscosity  $\nu$  is chosen to be sufficiently small such that the eddy diffusion will not contaminate the major physics within a squall line system.

---

<sup>1</sup> The "order" here refers to the order of the highest derivative in  $z$  for the ordinary differential equation.

When  $\bar{w}(z)$  becomes part of the basic state as well as  $\bar{u}$ , the existence of  $\bar{v}$  and the y-dependence of  $\bar{u}$  are inevitably implied. Their associated effects can only be checked *a posteriori* when a more complete model is under consideration, i.e., we also have to consider the transverse wave momentum equation.

Assuming the forcing  $Q' = Q(z) \exp[ik(x - ct)]$ , all other fields will have similar functional form such as  $u' = u(z) \exp[ik(x - ct)]$  and  $w' = w(z) \exp[ik(x - ct)]$ . The governing equations for wave perturbations can be written, with primes omitted, as:

$$-i\hat{\omega}u + \bar{w} \frac{du}{dz} + w \frac{d\bar{u}}{dz} = -ik\phi + A \frac{d}{dz} [\bar{M}_c(u - u_c) + M_c(\bar{u} - \bar{u}_c)] + v \frac{d^2 u}{dz^2}, \quad (3.5)$$

$$iku + \frac{dw}{dz} - w = 0, \quad (3.6)$$

$$-\frac{i\hat{\omega}d\phi}{R dz} + w\Gamma = Q, \quad (3.7)$$

where

$$A = (g/p_0) \exp(z)$$

and

$$\hat{\omega} = k(c - \bar{u}) \quad (3.8)$$

is the intrinsic frequency.

In the following, we shall use the term "viscous" to represent the gravity wave system when cumulus friction is included (that is, (3.5)-(3.7)). The viscous results

are to be compared with those due to a traditional simple gravity wave system, hereafter referred to as "inviscid", without cumulus friction but forced by the identical cumulus heating<sup>1</sup>.

If we use (3.7) to eliminate  $w$ , (3.5) and (3.6) can be written as the following:

$$\begin{aligned} \frac{d^2 u}{dz^2} + \frac{1}{v}(A\bar{M}_c - \bar{w})\frac{du}{dz} - \frac{1}{v}\frac{d\bar{u}}{dz}\frac{i\hat{\omega}}{R\Gamma}\frac{d\phi}{dz} + \frac{1}{v}\left(A\frac{d\bar{M}_c}{dz} + i\hat{\omega}\right)u - \frac{ik}{v}\phi \\ = \frac{A}{v}\frac{d\bar{M}_c}{dz}u_c - \frac{A}{v}\frac{dM_c}{dz}(\bar{u} - \bar{u}_c) - \frac{A}{v}M_c\frac{d\bar{u}}{dz} + \frac{1}{v}\frac{d\bar{u}}{dz}\frac{Q}{\Gamma} \end{aligned} \quad (3.9)$$

$$\frac{d^2 \phi}{dz^2} + \left[ \frac{\Gamma}{\hat{\omega}} \frac{d}{dz} \left( \frac{\hat{\omega}}{\Gamma} \right) - 1 \right] \frac{d\phi}{dz} + \left( R\Gamma \frac{k}{\hat{\omega}} \right) u = -\frac{R\Gamma}{i\hat{\omega}} \left[ \left( \frac{d}{dz} - 1 \right) \frac{Q}{\Gamma} \right]. \quad (3.10)$$

(3.9) and (3.10) can be combined into a more compact form using the matrix notation, namely,

$$\frac{d^2}{dz^2} \underline{f} + \underline{X} \frac{d}{dz} \underline{f} + \underline{Y} \underline{f} = \underline{Z} u_c \quad (3.11)$$

where

$$\underline{X} = \begin{pmatrix} \frac{1}{v}(A\bar{M}_c - \bar{w}) & -\frac{1}{v}\frac{d\bar{u}}{dz}\frac{i\hat{\omega}}{R\Gamma} \\ 0 & \frac{\Gamma}{\hat{\omega}}\frac{d}{dz}\left(\frac{\hat{\omega}}{\Gamma}\right) - 1 \end{pmatrix}$$

$$\underline{Y} = \begin{pmatrix} \frac{1}{v}\left(A\frac{d\bar{M}_c}{dz} + i\hat{\omega}\right) & -\frac{ik}{v} \\ R\Gamma\frac{k}{\hat{\omega}} & 0 \end{pmatrix}$$

---

<sup>1</sup> In other words, (3.5) is replaced by:

$$-i\hat{\omega}u + w\frac{d\bar{u}}{dz} = -ik\phi + v\frac{d^2 u}{dz^2},$$

while (3.6) and (3.7) remain the same.

$$\underline{Z} = \begin{pmatrix} \frac{A}{v} \frac{d\bar{M}_c}{dz} & \frac{1}{v} \left( \frac{d\bar{u}}{dz} \frac{Q}{\Gamma} - A \frac{dM_c}{dz} (\bar{u} - \bar{u}_c) - AM_c \frac{d\bar{u}}{dz} \right) \\ 0 & -\frac{R\Gamma}{i\hat{\omega}} \left[ \left( \frac{d}{dz} - 1 \right) \frac{Q}{\Gamma} \right] \end{pmatrix}$$

$$\underline{f} = \begin{pmatrix} u \\ \phi \end{pmatrix}, \quad \underline{u}_c = \begin{pmatrix} u_c \\ 1 \end{pmatrix}.$$

## ***b. Boundary conditions***

### ***1) Lower boundary condition***

The ultimate lower boundary condition is that the vertical velocity on the geometric coordinates vanishes at the ground. The linearized version of this condition on the log-pressure coordinates is:

$$w = \frac{i\hat{\omega}}{gH_0} \phi \quad \text{at } z = 0, \quad (3.12)$$

where  $H_0$  is the scale height associated with the temperature at the surface.

A surface mixed layer extending from ground to 600 m is assumed. Surface drag in the form of linear damping will be taken into account. The potential temperature and the horizontal velocity of the environment are well mixed in the surface layer as indicated by, say, the observational study of Augstein et al., (1974). Because there are no clouds, both cumulus heating and cloud mass flux vanish in this layer. It follows that the perturbations of geopotential and horizontal velocity are independent of height and are simply equal to their respective values at the cloud base. Moreover, from the wave heat equation, there is no temperature perturbation in the surface layer.

We have to emphasize that as suggested by Sarachik (1985), in the tropical atmosphere the mixing is present not only in the mixed layer but also in the trade cumulus layer which caps the mixed layer and extends to about 2~3 km where the trade wind inversion is. The mechanism of mixing for the two layers, however, are different from each other. Due to the occurrence of the phase change of water in the trade cumulus layer, not all the thermodynamic quantities are as well-mixed as in the mixed layer. In fact, Augstein et al. (1974) did observe a moisture profile which is almost independent of height in the trade cumulus layer but the same thing is not true for the potential temperature. Knowing the presence of mixing, the effects of surface drag in principle should also be taken into account in the trade cumulus layer. However, as will be explained later, the way the surface drag has its influence on the solution is through the lower boundary condition which is itself mainly a function of the damping rate associated with surface drag and the depth of the layer. We shall show that as long as the depth of the layer (in the log-pressure coordinates) is much smaller than one, and the linear damping time scale is much longer than the gravity wave time scale, the effective lower boundary condition is not sensitive to the parameters just mentioned. Therefore, for simplicity, the drag effects up to the trade inversion will not be considered in the following; since we believe that the solution will not be affected by such an assumption.

The bulk aerodynamic formula for the surface drag is:

$$\tau_s = \rho C_D |\vec{v}| \vec{v}. \quad (3.13),$$

where  $C_D$  is the surface drag coefficient of the ocean. The time rate of change of  $u$  owing to the surface drag is

$$\frac{1}{\rho} \frac{\partial}{\partial z} \tau_s \sim \frac{C_D |u_0|}{\Delta z} u,$$

where  $u_0$  is the gustiness parameter and  $\Delta z$  is the depth of mixed layer. Given

$$C_D = 1.5 \cdot 10^{-3},$$

$$u_0 = 8 \text{ m/s, and}$$

$$\Delta z = 600 \text{ m,}$$

the linear damping rate in association with the surface drag is:

$$D = \frac{C_D |u_0|}{\Delta z} = 2 \cdot 10^{-5} s^{-1} \sim \frac{1}{14hr}. \quad (3.14)$$

Therefore, in the mixed layer, the wave momentum equation becomes:

$$-i\hat{\omega}u_m = -ik\phi_m - Du_m, \quad (3.15)$$

where the subscript "m" denotes the value characteristic of the mixed layer.

Moreover, from the continuity equation, we have:

$$iku_m + \frac{dw_m}{dz} - w_m = 0$$

$$\Rightarrow w_m(z) = iku_m + (w(0) - iku_m)e^z. \quad (3.16)$$

With the aid of (3.12) and (3.15), (3.16) can be rewritten as:

$$\frac{w_m(z)}{\phi_m} = \frac{i\hat{\omega}}{gh_m} \left[ 1 - \left( 1 - \frac{h_m}{H_0} \right) e^z \right] \quad (3.17)$$

in the mixed layer, where

$$h_m = \frac{1}{g} \frac{\hat{\omega}(\hat{\omega} + iD)}{k^2}. \quad (3.18)$$

If one quantifies (3.17) at the top of the mixed layer ( $z_c^-$ ), the following equation will be yielded:

$$\frac{w_m}{\phi_m} = \frac{1}{C_b} \quad \text{at} \quad z = z_c^- \quad (3.19)$$

where

$$C_b = \frac{g h_m}{i \hat{\omega} \left[ 1 - \left( 1 - \frac{h_m}{H_0} \right) e^{z_c} \right]}.$$

Because the continuity of  $w$  and  $\phi$  across the interface between the mixed layer and the cloud layer are required, as a result, we expect that (3.19) should hold at the bottom of the cloud layer ( $z_c^+$ ) as well.

It proves appropriate at this point to study the sensitivity of results to the choice of the depth of the surface mixed layer. For simplicity, simple gravity waves without cumulus friction and eddy viscosity will be considered. Applying the continuity equation at the top of the mixed layer with the help of (3.15) and (3.19), the following equation which serves as the effective lower boundary condition for  $w$  at the cloud base is obtained:

$$\frac{dw}{dz} + \left( \frac{ik^2 C_b}{\hat{\omega} + iD} - 1 \right) w = 0 \quad \text{at} \quad z = z_c. \quad (3.20)$$

Typically,  $z_c \sim 0.1$ ,  $D/\hat{\omega} \ll 1$  (the damping time scale associated with the surface drag is much longer than the time scale for the gravity wave), and  $H_0 \sim 8000$  m, we can show that

$$C_b \sim \frac{(c - \bar{u})^2}{\hat{\omega} z_c} \left( -\frac{D}{\hat{\omega}} + i \right). \quad (3.21)$$



With the above equation, (3.20) can be further simplified to the following:

$$\frac{dw}{dz} - \left(\frac{1}{z_c}\right)w \sim 0 \quad \text{at } z = z_c. \quad (3.22)$$

As one can see that under such a condition only the depth of the surface mixed layer will affect the form of the lower boundary condition. It can be further demonstrated (see section 4.1.c.1)) that (3.22) is in fact not too different from the case of simply letting  $w=0$  at  $z=z_c$  as the effective lower boundary condition (owing to the fact that  $1/z_c \gg 1$ ). Therefore, as long as the depth of the surface mixed layer is such that  $z_c \ll 1$ , we argue that our results will not be sensitive to its actual value.

## 2) Upper boundary condition

Above the cloud layer, a radiating wave which carries energy upward with constant vertical wavelength will be assumed, in mathematical terms, this means:

$$\frac{d}{dz}(\quad) \sim (i\lambda_s + 0.5)(\quad) \quad (3.23)$$

where

$$\lambda_s = \frac{\sqrt{R\Gamma_s}}{u_s - c} = \text{constant}. \quad (3.24)$$

The term 0.5 in (3.23) is caused by the density stratification,  $\Gamma_s$  and  $\bar{u}_s$  represent values of the static stability and the mean zonal flow in the stratosphere. Thus far, the zonal wavenumber ( $k$ ) has been assumed to be positive without any loss of generality, if  $k$  is negative, then a change of sign in (3.24) is necessary in order for (3.23) to remain valid.

With (3.23), the continuity equation in the stratosphere becomes

$$u = \frac{i}{k}(i\lambda_s - 0.5)w, \quad (3.25)$$

together with the momentum equation in the stratosphere,

$$-i\hat{\omega}u = -ik\phi, \quad (3.26)$$

the following relationship which is similar to (3.19) can be derived,

$$\frac{w}{\phi} = \frac{1}{C_i} \quad \text{for } z > z_i \quad (3.27)$$

where

$$C_i = \frac{i\hat{\omega}}{k^2}(i\lambda_s - 0.5).$$

In a like manner, by arguing the continuity of  $w$  and  $\phi$ , we require that (3.27) still holds across the interface between the cloud layer and the stratosphere.

### *c. Method of solutions*

This section is devoted to the description of the method of solution which includes the numerical scheme and the implementation of the boundary conditions.

The numerical scheme of Lindzen and Kuo (1969) will be used with slight modification since part of the forcing depends on the solution<sup>1</sup> (Stevens et al., 1977). We can write down (3.11) in the finite difference form:

$$\underline{A}_n f_{n-1} + \underline{B}_n f_n + \underline{C}_n f_{n+1} = \underline{D}_n u_c \quad (3.28)$$

---

<sup>1</sup> Namely,  $u_c$  in (3.11), which is part of the forcing, is not known prior to the solving of the equations. As a matter of fact, the reason that the forcing term in (3.11) having been decomposed into the product of two matrices is to facilitate the later dealing of this problem.

where

$$\underline{A}_n = \frac{1}{\Delta z^2} \underline{I} - \frac{1}{2\Delta z} \underline{X},$$

$$\underline{B}_n = \frac{-2}{\Delta z^2} \underline{I} + \underline{Y},$$

$$\underline{C}_n = \frac{1}{\Delta z^2} \underline{I} + \frac{1}{2\Delta z} \underline{X},$$

$$\underline{D}_n = \underline{Z},$$

$$\underline{I} = \begin{pmatrix} 1 & 0 \\ 0 & 1 \end{pmatrix}.$$

Assume further that the solution has the form of

$$\underline{f}_n = \underline{\alpha}_n \underline{f}_{n+1} + \underline{\beta}_n \underline{u}_c, \quad (3.29)$$

or equivalently

$$\underline{f}_{n-1} = \underline{\alpha}_{n-1} \underline{f}_n + \underline{\beta}_{n-1} \underline{u}_c. \quad (3.30)$$

Eliminating  $\underline{f}_{n+1}$  between (3.28) and (3.29), and comparing the resultant equation with (3.30) yields the following recurrence relations:

$$\begin{aligned} \underline{\alpha}_{n-1} &= -\underline{A}_n^{-1} (\underline{B}_n + \underline{C}_n \underline{\alpha}_n^{-1}), \\ \underline{\beta}_{n-1} &= \underline{A}_n^{-1} (\underline{D}_n + \underline{C}_n \underline{\alpha}_n^{-1} \underline{\beta}_n). \end{aligned} \quad (3.31)$$

The numerical scheme can also be called the up-down sweep method since only two "sweeps" over the domain are necessary to obtain the solution. Due to the fact that  $\underline{u}_c$  is unknown *a priori*, it appears that we should start the first sweep from the top. When the bottom is reached, by using the consistency condition, i.e.  $\underline{u}(z_0) = \underline{u}_c$ ,  $\underline{u}_c$  will then be obtained.

To begin with, how do we implement (3.27)? Let  $L$  denote the level where the cloud top is. Our primary goal is to obtain a relationship between  $f_L$  and  $f_{L-1}$ , which in turn will give us information about  $\alpha_{L-1}$  and  $\beta_{L-1}$ , then march downward with (3.31) to obtain  $\alpha$ 's and  $\beta$ 's for the rest of the levels.

Above the cloud top, the radiation condition is applied such that

$$\phi_{L+1} = \phi_L \exp[(i\lambda_s + 0.5)\Delta z]$$

(cf. (3.23)). Furthermore, from the momentum equation,

$$u_{L+1} = (k/\hat{\omega})\phi_{L+1}.$$

We thus have

$$u_{L+1} = \varepsilon\phi_L, \quad (3.32)$$

where

$$\varepsilon = (k/\hat{\omega}) \exp[(i\lambda_s + 0.5)\Delta z].$$

Substituting (3.27) and (3.32) into the finite difference form of (3.5) at level  $L$  yields

$$\begin{aligned} u_{L-1} = & \frac{1}{\xi} \left[ 2 - \frac{\Delta z^2}{v} \left( A \frac{d\bar{M}_c}{dz} + i\hat{\omega} \right) \right] u_L + \frac{1}{\xi} \left[ -\varepsilon - \varepsilon \frac{\Delta z}{2} \frac{1}{v} (A\bar{M}_c - \bar{w}) + \frac{\Delta z^2}{v} \left( ik + \frac{1}{C_i} \frac{d\bar{u}}{dz} \right) \right] \phi_L \\ & + \left[ \frac{1}{\xi} \frac{\Delta z^2}{v} A \frac{d\bar{M}_c}{dz} \right] u_c + \frac{1}{\xi} \left[ -\frac{\Delta z^2}{v} A \left( \frac{dM_c}{dz} (\bar{u} - \bar{u}_c) + M_c \frac{d\bar{u}}{dz} \right) \right] \end{aligned} \quad (3.33)$$

where

$$\xi = 1 - \frac{\Delta z}{2} \frac{1}{v} (A\bar{M}_c - \bar{w}).$$

Applying (3.29) at level  $L-1$  gives

$$f_{L-1} = \alpha_{L-1} f_L + \beta_{L-1} u_c,$$

---

**1** Or more specifically, we want to be able to express  $u$  and  $\phi$  at level  $L-1$  in terms of linear combinations of  $\phi_L$ ,  $u_L$  and  $u_c$ .

or this can be rewritten as

$$\begin{pmatrix} u_{L-1} \\ \phi_{L-1} \end{pmatrix} = \begin{pmatrix} \alpha_1 & \alpha_2 \\ \alpha_3 & \alpha_4 \end{pmatrix} \begin{pmatrix} u_L \\ \phi_L \end{pmatrix} + \begin{pmatrix} \beta_1 & \beta_2 \\ \beta_3 & \beta_4 \end{pmatrix} \begin{pmatrix} u_c \\ 1 \end{pmatrix}. \quad (3.34)$$

Comparing (3.33) with (3.34), the following is obtained:

$$\begin{aligned} \alpha_1 &= \frac{1}{\xi} \left[ 2 - \frac{\Delta z^2}{v} \left( A \frac{d\bar{M}_c}{dz} + i\hat{\omega} \right) \right], \\ \alpha_2 &= \frac{1}{\xi} \left[ -\epsilon - \epsilon \frac{\Delta z}{2} \frac{1}{v} (A\bar{M}_c - \bar{w}) + \frac{\Delta z^2}{v} \left( ik + \frac{1}{C_t} \frac{d\bar{u}}{dz} \right) \right], \\ \beta_1 &= \frac{1}{\xi} \frac{\Delta z^2}{v} A \frac{d\bar{M}_c}{dz}, \\ \beta_2 &= \frac{1}{\xi} \left[ -\frac{\Delta z^2}{v} A \left( \frac{dM_c}{dz} (\bar{u} - \bar{u}_c) + M_c \frac{d\bar{u}}{dz} \right) \right]. \end{aligned} \quad (3.35)$$

The finite difference form of the continuity equation (3.6) at level L is

$$iku_L + \frac{1}{2\Delta z} (w_{L+1} - w_{L-1}) - w_L = 0. \quad (3.36)$$

The next question concerns with how to relate  $w$ 's in (3.36) to  $u$  and  $\phi$  at levels L and L-1. From (3.27) we have,

$$w_{L+1} = \frac{1}{C_t} \phi_{L+1} = \frac{1}{C_t} \exp[(i\lambda_s + 0.5)\Delta z] \phi_L \quad (3.37)$$

as well as

$$w_L = \frac{1}{C_t} \phi_L. \quad (3.38)$$

In addition, the heat equation (3.7) applied at level L-1 yields

$$w_{L-1} = \frac{1}{\Gamma_{L-1}} \left[ Q_{L-1} + \frac{i\hat{\omega}}{R2\Delta z} (\phi_L - \phi_{L-2}) \right]. \quad (3.39)$$

Our task then becomes an attempt to relate  $\phi_{L-2}$  to  $u$  and  $\phi$  at levels L and L-1. This can be accomplished by a somewhat tedious way. The procedure is described in the following. Given that

$$\underline{f}_{L-2} = \underline{\alpha}_{L-2} \underline{f}_{L-1} + \underline{\beta}_{L-2} \underline{u}_c, \quad (3.40.a)$$

$$\underline{\alpha}_{L-2} = -\underline{A}_{L-1}^{-1} (\underline{B}_{L-1} + \underline{C}_{L-1} \underline{\alpha}_{L-1}^{-1}), \quad (3.40.b)$$

$$\underline{\beta}_{L-2} = \underline{A}_{L-1}^{-1} (\underline{D}_{L-1} + \underline{C}_{L-1} \underline{\alpha}_{L-1}^{-1} \underline{\beta}_{L-1}), \quad (3.40.c)$$

we first express  $\underline{\alpha}_{L-2}$  and  $\underline{\beta}_{L-2}$  in terms of  $\underline{\alpha}_{L-1}$  and  $\underline{\beta}_{L-1}$ , knowing that half of the last two matrices are still unknown. As a second step, from (3.40.a) one has

$$\phi_{L-2} = \alpha_{L-2,2,1} u_{L-1} + \alpha_{L-2,2,2} \phi_{L-1} + \beta_{L-2,2,1} u_c + \beta_{L-2,2,2},$$

where  $\alpha_{L,i,j}$  represents the (i,j)th element of the matrix  $\underline{\alpha}$  at level L. With the information given in (3.33), we are then able to write down the above equation in another form:

$$\phi_{L-2} = E_1 u_L + E_2 \phi_L + E_3 \phi_{L-1} + E_4 u_c + E_5 \quad (3.41)$$

where  $E_1, E_2, E_3, E_4,$  and  $E_5$  are functions of  $\alpha_3, \alpha_4, \beta_3$  and  $\beta_4$  which are defined in (3.34). With (3.37), (3.38), (3.39) and (3.41), (3.36) becomes

$$\begin{aligned} \phi_{L-1} = & -[(ik2\Delta z + FE_1)/(FE_3)]u_L - \{[G/C_t - F(1 - E_2)]/(FE_3)\}\phi_L \\ & - (E_4/E_3)u_c + (Q_{L-1}\Gamma_{L-1} - FE_5)/(FE_3), \end{aligned} \quad (3.42.a)$$

where

$$F = \frac{1}{\Gamma_{L-1}} \frac{i\hat{\omega}}{R2\Delta z}, \quad G = \exp[(i\lambda_s + 0.5)\Delta z] - 2\Delta z.$$

From (3.34) we have

$$\phi_{L-1} = \alpha_3 u_L + \alpha_4 \phi_L + \beta_3 u_c + \beta_4. \quad (3.42.b)$$

Given the following:

$$\underline{A}_{L-1} = \begin{pmatrix} A_1 & A_2 \\ A_3 & A_4 \end{pmatrix}, \quad \underline{B}_{L-1} = \begin{pmatrix} B_1 & B_2 \\ B_3 & B_4 \end{pmatrix}, \quad \underline{C}_{L-1} = \begin{pmatrix} C_1 & C_2 \\ C_3 & C_4 \end{pmatrix}, \quad \underline{D}_{L-1} = \begin{pmatrix} D_1 & D_2 \\ D_3 & D_4 \end{pmatrix}, \quad (3.43)$$

then, after equating (3.42.a) with (3.42.b), we have

$$\begin{aligned} \alpha_3 &= \{R4\Delta z^2 \Gamma_{L-1} k \hat{\omega}^{-1} - \alpha_1(A_3 B_1 + A_4 B_3) - (A_3 C_1 + A_4 C_3)\} (A_3 B_2 + A_4 B_4)^{-1}, \\ \alpha_4 &= [-iR2\Delta z \Gamma_{L-1} (\hat{\omega} C_i)^{-1} G - 1 - \alpha_2(A_3 B_1 + A_4 B_3) - (A_3 C_2 + A_4 C_4)] (A_3 B_2 + A_4 B_4)^{-1}, \\ \beta_3 &= \{-(A_3 B_1 + A_4 B_3) \beta_1 + A_3 D_1 + A_4 D_3\} (A_3 B_2 + A_4 B_4)^{-1}, \\ \beta_4 &= \{iR2\Delta z \hat{\omega}^{-1} Q_{L-1} - (A_3 B_1 + A_4 B_3) \beta_2 + A_3 D_2 + A_4 D_4\} (A_3 B_2 + A_4 B_4)^{-1}. \end{aligned} \quad (3.44)$$

Our goal of specifying  $\underline{\alpha}_{L-1}$  and  $\underline{\beta}_{L-1}$  is achieved by (3.44) together with (3.35).

Finally, all  $\underline{\alpha}$ 's and  $\underline{\beta}$ 's in the lower layers will be obtained with the help of (3.31).

Regarding the implementation of the lower boundary condition, first let "0" denote the level where the cloud base is, and "1" and "-1" one level above and below the cloud base respectively. Prior to any formal calculation, the following expressions are worth mentioning:

$$u_c = u_0, \quad (3.45)$$

$$u_{-1} = \frac{k}{\hat{\omega} + iD} \phi_{-1} = \frac{k}{\hat{\omega} + iD} \phi_0, \quad (3.46)$$

$$w_0 = \frac{1}{C_b} \phi_0. \quad (3.47)$$

(3.45) is by definition (refer to section 3.1.a), (3.46) is due to the fact that  $\phi$  is not a function of height in the surface mixed layer and is continuous across the cloud base, and (3.47) is simply another form of (3.19). The finite difference form of

(3.5) applied at the cloud base with the information contained in (3.45) to (3.47) is:

$$\begin{aligned}
& \left(-2 + \frac{\Delta z^2}{\nu} i \hat{\omega}\right) u_0 + \left[-1 - \frac{\Delta z}{2\nu} (A \bar{M}_c - \bar{w})\right] u_1 \\
& + \left\{ \frac{k}{\hat{\omega} + iD} \left[1 + \frac{\Delta z}{2\nu} (A \bar{M}_c - \bar{w})\right] - \frac{\Delta z^2}{\nu} \left(ik + \frac{1}{C_b} \frac{d\bar{u}}{dz}\right) \right\} \phi_0 \\
& = -\frac{\Delta z^2}{\nu} A \left[ \frac{dM_c}{dz} (\bar{u} - \bar{u}_c) + M_c \frac{d\bar{u}}{dz} \right]. \tag{3.48}
\end{aligned}$$

Also, the continuity equation applied at the cloud base gives:

$$ik2\Delta z u_0 - \left\{ w_1 - \frac{i \hat{\omega}_m}{g h_m} \left[1 - \left(1 - \frac{h_m}{H_0}\right) e^{z_c - \Delta z}\right] \phi_0 \right\} - \frac{2\Delta z}{C_b} \phi_0 = 0. \tag{3.49}$$

At this point, we have encountered the same problem as before concerning how to relate  $w$  to  $u$  and  $\phi$  at levels 0 and 1.

To achieve this, first write down the heat equation at level 1:

$$w_1 = \frac{1}{\Gamma_1} \left[ Q_1 + \frac{i \hat{\omega}_1}{R 2\Delta z} (\phi_2 - \phi_0) \right]. \tag{3.50}$$

In addition, we have the following:

$$\begin{aligned}
& \mathcal{L}_2 = \underline{\alpha}_1^{-1} (\mathcal{L}_1 - \underline{\beta}_1 u_c) \\
& \Rightarrow \begin{pmatrix} u_2 \\ \phi_2 \end{pmatrix} = \begin{pmatrix} \alpha_1 & \alpha_2 \\ \alpha_3 & \alpha_4 \end{pmatrix} \begin{bmatrix} u_1 \\ \phi_1 \end{bmatrix} - \begin{pmatrix} \beta_1 & \beta_2 \\ \beta_3 & \beta_4 \end{pmatrix} \begin{pmatrix} u_0 \\ 1 \end{pmatrix} \\
& \Rightarrow \phi_2 = \alpha_3 (u_1 - \beta_1 u_0 - \beta_2) + \alpha_4 (\phi_1 - \beta_3 u_0 - \beta_4) \tag{3.51}
\end{aligned}$$

where we have let

$$\underline{\alpha}_1^{-1} = \begin{pmatrix} \alpha_1 & \alpha_2 \\ \alpha_3 & \alpha_4 \end{pmatrix}, \quad \underline{\beta}_1 = \begin{pmatrix} \beta_1 & \beta_2 \\ \beta_3 & \beta_4 \end{pmatrix}.$$



Note that the definitions above are not to be confused with those in (3.34).

Substitute (3.51) into (3.50), then substitute the resultant equation into (3.49) yields

$$\begin{aligned}
& \left[ ik2\Delta z - \frac{i\hat{\omega}_1}{R\Gamma_1 2\Delta z} (\alpha_3\beta_1 + \alpha_4\beta_3) \right] u_0 + \left[ \frac{i\hat{\omega}_1}{R\Gamma_1 2\Delta z} \alpha_3 \right] u_1 \\
& + \left\{ -\frac{i\hat{\omega}_m}{g h_m} \left[ 1 - \left( 1 - \frac{h_m}{H_0} \right) e^{z_c - \Delta z} \right] - \frac{2\Delta z}{C_b} - \frac{i\hat{\omega}_1}{R\Gamma_1 2\Delta z} \right\} \phi_0 + \left[ \frac{i\hat{\omega}_1}{R\Gamma_1 2\Delta z} \alpha_4 \right] \phi_1 \\
& = \frac{i\hat{\omega}_1}{R\Gamma_1 2\Delta z} (\alpha_3\beta_2 + \alpha_4\beta_4) - \frac{Q_1}{\Gamma_1}
\end{aligned} \tag{3.52}$$

As a consequence, (3.48), (3.52) together with

$$f_0 = \alpha_0 f_1 + \beta_0 u_c \tag{3.53}$$

form a system of four equations and four unknowns ( $u_0$ ,  $\phi_0$ ,  $u_1$  and  $\phi_1$ ). After solving  $u$  and  $\phi$  at levels 0 and 1, the numerical integration will be formally complete following another up-sweep using (3.29).

Given the seemingly complex approach of carrying out the boundary conditions, it is consistent at least in the following senses:

- 1) Both boundary conditions are converted to finite difference forms with second order accuracy which is consistent with the equations themselves.
- 2)  $w$  and  $\phi$  are required to be continuous across both the upper and lower interfaces.
- 3) When implementing the boundary conditions, momentum and continuity equations are always used first, then the heat equation.

Nevertheless, one may still wonder about the accuracy of the way the boundary conditions were carried out. A good method of verifying this is to consider a simple gravity wave case without cumulus friction. In this case, the eddy

viscosity term is no longer necessary and the whole problem, i.e. (3.11), can be reformulated into a second order ordinary differential equation while still being subject to the same boundary conditions (3.19) and (3.27). For this simple case, the boundary conditions are implemented very easily. Results thus obtained are to be compared with the ones from the full version of the model but with cumulus friction being turned off. It is found that, as long as the eddy viscosity stays much smaller than the other terms in the momentum equation, results obtained from two versions of the model are almost identical. As a consequence, we are quite confident about the accuracy of the numerical scheme just described.

### 3.3 Data

We shall mainly use data obtained from two experiments conducted over the tropical oceans, namely, that of GATE (the eastern Atlantic, e.g. Thompson et al. 1979) and of the Marshall Islands tests (the western Pacific, e.g. Reed and Recker, 1971). As explained previously, fields characteristic of *the convergent phase of easterly waves* will be used as the basic states for squall lines. Figure 3.3 shows vertical distributions of mean zonal flow ( $\bar{u}$ ) and mean vertical velocity ( $\bar{w}$ ) observed during GATE. The corresponding profiles of the static stability parameter and dry and moist static energy are displayed in Figure 3.4. The counterparts of Figures 3.3 and 3.4 for Marshall Islands tests are shown in Figures 3.5 and 3.6 respectively. In order to resolve the trade cumulus layer whose depth is around the order of 2 to 3 km, we have deliberately replaced the static stability parameter field in that region with the one observed by Augstein et al. (1974) from ATEX (Atlantic Tradewind Experiment). Figure 3.7 displays profiles of the cloud mass flux and cumulus heating for GATE using the

parameterization scheme described in section 3.1.a. A normalization corresponding to a precipitation rate of 4.8 cm/day (viz. (3.4)) has been made. Figure 3.8 is similar to Figure 3.7 except that it is for Marshall Islands tests. In order to make the parameterization scheme completely consistent, the cloud top ( $z_c$ ) is determined as the height where the surface air parcel loses its buoyancy, namely

$$C_p T(0) + Lq(0) = C_p T(z_c) + g z_c, \quad (3.54)$$

with "0" representing the ground. Finally, phase speeds of -10, -11, -12, and -13 m/s are used in the calculation.

## Chapter 4: Results and Discussions

### 4.1 Monochromatic Precipitation

As already noted, the wavelength of the monochromatic gravity wave is chosen to be 200 km, and the mean ( $\bar{P}$ ) and the amplitude of the perturbation ( $P'$ ) precipitation are both taken to be 4.8 cm/day.

#### *a. Description of solutions*

##### *1) In the cloud layer*

Results of two typical viscous cases are shown in Figure 4.1 (Marshall Islands profiles, with  $c = -10$  m/s) and Figure 4.3 (GATE profiles, with  $c = -11$  m/s). Their respective inviscid counterparts are shown in Figures 4.2 and 4.4. Fields shown include the vertical distributions of both the amplitude and the phase of  $T$ ,  $u$  and  $w$ <sup>1</sup> (frames (a), (b) and (c)), and all possible components of the momentum flux (frames(d)), *averaged over one wavelength*, associated with a squall line system. When presenting  $w$ , in addition to the usual amplitude and the phase, we have also drawn the direct response of  $w$  to cumulus heating which is equal to  $Q/\Gamma$  from (3.7). It is obvious that the response of  $w$  is dominated by the direct response to cumulus heating.

---

<sup>1</sup> It should be kept in mind that the final solution is the real part of the product of the vertical structure and  $\exp(ikx)$ .

From frames (d) in both Figures 4.1 and 4.3, most of the mean momentum flux in the troposphere is accounted for by cloud transports<sup>1</sup> which include the following two components:

$$-\overline{M_c}(\overline{u} - \overline{u_c}) - \overline{(M_c')}(u' - u'_c). \quad (4.1)$$

Gravity wave transport only has a very minor effect. Furthermore, between the two components in (4.1), it is the mean cloud activity,  $-\overline{M_c}(\overline{u} - \overline{u_c})$ , which is the dominant mean momentum transport contributor.

In the wave momentum equation, the perturbation convergence of the momentum flux by clouds<sup>2</sup> is found to be small compared to the inertial term ( $-i\hat{\omega}u$ ) which is to be balanced chiefly by the pressure gradient force ( $-ik\phi$ ). Therefore, cumulus friction is not important physically to the gravity wave itself.

If we calculate the magnitude of each term in the wave momentum equation (3.5), we see that the dominant terms are  $-i\hat{\omega}u$ ,  $-ik\phi$ ,  $\overline{w} \cdot (du/dz)$  and  $A\overline{M_c} \cdot (du/dz)$ ; but since the last two terms roughly cancel each other out, the effect of cumulus friction is almost eliminated. If we had included  $\overline{M_c}$  but not  $\overline{w}$ , the role of cumulus friction might have been misrepresented.

Although it cannot be denied that for individual cases, minor differences do exist between viscous and inviscid runs (compare Figure 4.1 with 4.2, and Figure 4.3 with 4.4), especially in the T and u fields, those differences do not

---

<sup>1</sup> According to (2.1), after decomposing each field into a mean (overbarred quantity) and a perturbation (primed quantity), momentum transport due to clouds should be equal to:

$$-\overline{M_c}(\overline{u} - \overline{u_c}) - \overline{M_c}(u' - u'_c) - M_c'(\overline{u} - \overline{u_c}) - M_c'(u' - u'_c).$$

However, after averaging, only the first and the last terms remain.

<sup>2</sup> Namely, from (3.5), it is the vertical derivative of

$$\overline{M_c}(u' - u'_c) + M_c'(\overline{u} - \overline{u_c}).$$

exhibit a consistent pattern. A comparison of the composite of all viscous cases with that of all inviscid cases shows little difference. Table 4.1 summarizes the average and range (or variation) of the typical amplitude for each field in the interior of troposphere for all cases that have been investigated. Since  $w$  is mainly determined by the thermal forcing which is always normalized according to a fixed precipitation rate, it displays little variation. As one can see, there is almost no difference between viscous and inviscid cases; however, the presence of cumulus friction seems to be able to reduce the variation among different cases.

Although the perturbation rainfall has an amplitude which is as large as the mean, linearization is found to be a good approximation still. This can be verified, for instance, by the fact that the term  $-i\hat{\omega}u$  is much larger than the term  $u\partial u/\partial x$ .

## *2) Near the cloud top and/or above the cloud layer*

The first thing to notice from Figures 4.1-4.4 is that above 12 km where the cloud top is, all fields exhibit a simple structure with the amplitude increasing with height and the phase varying linearly with height. This is simply an indication of the imposed upper radiation boundary condition.

Because clouds vanish above the cloud layer, momentum can now only be transported by gravity waves. Our numerical solutions show that the wave momentum flux actually does not vary with height above the cloud top. This is

consistent with the theorem by Eliassen and Palm (1960) stating that in the absence of forcing, damping and critical levels, the momentum flux is non-divergent.

In the upper troposphere and the stratosphere where the thermal forcing ceases, the leakage of the wave becomes a very delicate and sensitive matter (this will be explained in more details in Appendix). There is substantial variation between the cases. Table 4.2 is similar to Table 4.1 except that statistics in the lower stratosphere (~15 km) are presented. Larger variations between the case are evident.

The quantity  $(\rho u w)_{\text{global}}$  in Table 4.2, which is obtained by multiplying the average of the momentum flux at the cloud top due to gravity waves over one wavelength  $(\overline{\rho u' w'})$  by the *intermittency factor* ( $f$ ), represents the momentum flux, out of the cloud top, associated with tropical squall lines on a global basis. This intermittency factor arises because gravity waves are episodic both in time and space. The intermittency factor is estimated as:

$$f = r \frac{P_{\text{ave}} A_e}{\bar{P} L_x} \frac{L_x}{A_e} = r \frac{P_{\text{ave}}}{\bar{P}}, \quad (4.2)$$

where  $A_e$  is the length of the latitude circle,  $P_{\text{ave}}$  the global mean precipitation,  $\bar{P}$  the nonzero mean precipitation associated with a monochromatic gravity wave and  $r$  the fraction of  $P_{\text{ave}}$  accounted for by squall lines. So  $(P_{\text{ave}} A_e)/(\bar{P} L_x)$  represents the number of lines needed to account for the global precipitation while  $L_x/A_e$  is the fractional coverage of the latitude circle by a single squall line. Given  $P_{\text{ave}} = 0.6$  cm/day for the tropical region as a whole,  $\bar{P} = 4.8$  cm/day, and  $r = 0.5$ ,  $f \approx 0.0625$ .

Since there is a large variation in the static stability parameter across the cloud top, while  $w$  and  $\phi$  are required to be continuous, we expect, from the heat equation, that there should also be a large variation in  $T$  across the interface between the cloud layer and the cloud-free layer. This can be seen from frames (a) of Figures 4.1-4.4.

The lapse rate of perturbation temperature ( $|dT/dz|$ ) immediately below the cloud top for both viscous and inviscid cases has an average of  $0.24\text{ }^\circ\text{C/km}$  and a range of  $0.04$  to  $0.6\text{ }^\circ\text{C/km}$ . Moreover, in that region where cumulus heating vanishes and the radiation condition holds,  $|dT/dz|$  is found to be approximately equal to the product of the characteristic local vertical wavenumber  $\lambda$ , which is defined as  $(R\Gamma)^{1/2}/(\bar{u}-c)$  in the log-pressure coordinates, and  $|T|$ .

Lindzen (1981) pointed out that when the total temperature lapse rate becomes convectively unstable, wave breaking and turbulence are expected. However,  $|dT/dz|$  of  $0.24\text{ }^\circ\text{C/km}$  below the cloud top is still far from the breaking criterion, even though the local static stability parameter ( $d\bar{T}/dz+g/c_p$ , in the geometric coordinates) is low, say,  $1\text{ }^\circ\text{C/km}$ . In fact, if we further focus on individual cases, none satisfies the breaking condition. Therefore, at least for the precipitation rate chosen here, monochromatic waves do not seem to break at the cloud top. As will be seen later, the same conclusion is not true when a localized precipitation is assumed.



### ***b. Comparison with previous related studies***

Within the context of our model, two components of momentum flux can be distinguished, the one due to gravity waves  $\overline{\rho u' w'}$ , and the other one caused by cumulus clouds which is given by (4.1). From model results, we have shown that cloud transport is the major momentum flux contributor within a squall line system whose maximum total momentum flux (averaged over one wavelength) is about 0.4 Pa (see Figure 4.3.(d)). Because of the dominance of the term  $-\overline{M_c(\bar{u} - \bar{u}_c)}$  in (4.1), and the fact that  $\bar{u}$  profiles for both GATE and Marshall Islands tests generally have easterly shear with height (i.e.,  $(\bar{u} - \bar{u}_c) < 0$ ), the total mean momentum flux within a squall line in our model is consistently positive. Here, a positive value of the momentum flux implies that upward motions always transport horizontal momentum in a direction against the movement of a squall line; since, as mentioned earlier, observations suggest that fast-moving convective lines normally travel toward the west.

In their study using aircraft observations, LeMone et al. (1984) found out that for quasi-two-dimensional convective lines, upward motions do indeed systematically carry the front-to-rear momentum, where "front" is defined as the direction toward which the line is moving. The maximum mean momentum flux values for cases investigated by them vary from 0.2 to 2 Pa. The value of 0.4 Pa (the total mean momentum flux due to clouds and waves) obtained in our calculation falls within this range; although tends toward the smaller side. However, it has to be stressed that the averaging methods used are different between our study and LeMone et al. (1984). In our case, it is the average over one wavelength (200 km), while in LeMone et al. (1984), the mean momentum flux values were obtained after

normalizing to 100 km flight legs. Moreover, monochromaticity is by no means a correct depiction of the precipitation. If one considers a localized distribution, which will be treated later, and does the averaging over an accordingly smaller area, the value of the mean momentum flux associated with a squall line can be easily increased, and a better agreement with observations obtained.

As suggested in LeMone (1983) and LeMone et al. (1984), the momentum flux is concentrated in the leading 25 km of the convective line where the convective activity is most intense and is primarily associated with updraft cores<sup>1</sup>. LeMone et al. (1984) derived a simple expression for estimating the mean momentum flux:

$$\overline{\rho u'w'} \sim \rho f_c w_c u_c, \quad (4.3)$$

where  $f_c$  is the fractional coverage of updraft cores,  $w_c$  the median core vertical velocity and  $u_c$  is the core horizontal velocity relative to the surface. Interestingly enough, (4.3) is in some sense similar to (2.1), after assuming that  $\rho f_c w_c \sim M_c$ . It is evident that the implication from aircraft measurements also confirms our finding about the important role played by cumulus convection concerning the mean momentum transport.

### *c. Sensitivity tests*

#### *1) Lower boundary condition*

For simplicity, inviscid cases will be considered here. We have shown in

---

<sup>1</sup> The updraft cores here are required to have a vertical motion  $> 1$  m/s for at least 500 m, and according to GATE observations, they typically occupy 5% of a total flight leg penetrating a convective line (Zipser and LeMone, 1980).

the previous chapter that the appropriate lower boundary condition which is to be applied at the cloud base for this simple case is (viz. (3.20)):

$$\frac{dw}{dz} + \left( \frac{ik^2 C_b}{\hat{\omega} + iD} - 1 \right) w = 0 \quad \text{at } z = z_c, \quad (4.4)$$

where  $D$  is the constant linear damping rate associated with the surface drag (see (3.14)),  $k$  the zonal wave number,  $\hat{\omega}$  the intrinsic frequency, and  $C_b$  defined in (3.19) is the ratio between  $\phi$  and  $w$  at the cloud base. It has also been shown that with scales characteristic of gravity waves, (4.4) can be further approximated as (viz. (3.22)):

$$dw/dz - (1/z_c)w = 0 \quad \text{at } z = z_c. \quad (4.5)$$

Results using this particular lower boundary condition were used to compare against the ones using

$$dw/dz - (1/(2z_c))w = 0. \quad (4.6)$$

The difference in solutions is found to be negligible. This is because as long as  $z_c \ll 1$ , both (4.5) and (4.6) are not too different from simply letting  $w=0$  at  $z_c$ . Physically, using (4.6) in place of (4.5) means doubling the depth of the surface mixed layer. The insensitivity of solutions to different forms of the lower boundary condition indicates that the choice of the depth of the surface mixed layer only has a negligible effect.

## ***2) Upper boundary condition***

The upper boundary condition used here is the radiation condition. The way this condition is implemented is to assume a simple environment above the heating region so that the gravity wave has a constant vertical wave number  $\lambda = (R\Gamma)^{1/2}/(\bar{u} - c)$  (in the log-pressure coordinates). Tests are conducted to see the

degree of sensitivity of solutions outside the forcing region to choices of  $\bar{u}$  and  $\Gamma$ . Because constant  $\lambda$  is all that matters, we choose to use different values of  $\Gamma$  only. In the following calculation,  $\Gamma = 80 \text{ }^\circ\text{C}$  ( $\sim 12 \text{ }^\circ\text{C/km}$  in the geometric coordinates) is used for the control runs, and cases using  $\Gamma = 30 \text{ }^\circ\text{C}$  ( $\sim 4.5 \text{ }^\circ\text{C/km}$ ) will serve as a test. In addition, both GATE and Marshall Islands profiles and phase speeds of -11 and -12 m/s will be considered. Magnitude of  $w$  (cm/sec) at 16 km (already above the cloud top) is chosen for the purpose of comparison. Table 4.3 shows results of inviscid cases, those for viscous cases are displayed in Table 4.4. As one may see, smaller value of  $\Gamma$  consistently yields larger response outside the cloud layer.

This can be explained by a simple two-layer model (Eliassen and Palm, 1960) with a wave maker at the lower boundary, and each layer having a constant index of refraction ( $\lambda$ ). The solution for  $w$  in the lower layer may be written as

$$w_1 = A_1 \exp(i\lambda_1 z) + B_1 \exp(-i\lambda_1 z), \quad (4.7)$$

where  $A_1$  is the amplitude factor of the incident wave, and  $B_1$  is the amplitude factor of the reflected wave. In the upper layer which is semi-infinite, radiation condition is applied so the solution is:

$$w_2 = A_2 \exp(i\lambda_2 z). \quad (4.8)$$

*Transmission coefficient* ( $t$ ) is defined as  $|A_2/A_1|^2$ . By requiring both  $w$  and  $w_z$  to be continuous at the interface enables us to write

$$t = \left( \frac{2\lambda_1}{\lambda_1 + \lambda_2} \right)^2. \quad (4.9)$$

In the troposphere (layer 1),  $\Gamma$  and  $|c - \bar{u}|$  have average values of 22 °C and 5 m/s respectively, so  $\lambda_1 \approx 16$  °C. In the stratosphere (layer 2),  $|c - \bar{u}| \approx 3$  m/s, hence for  $\Gamma = 80$  °C,  $\lambda_2 \approx 51$  °C, and  $t \approx 0.68$ ; while for  $\Gamma = 30$  °C,  $\lambda_2 \approx 31$  °C and  $t \approx 0.48$ . We see that using  $\Gamma = 80$  °C leads to about 40% increase of the transmission coefficient compared to the case with  $\Gamma = 30$  °C. 40% increase of the transmission coefficient in turn implies roughly 20% increase of wave amplitudes. On the other hand, results (using varying basic state profiles) shown in Tables 4.3 and 4.4 indicate an average of 30% increase of wave amplitudes, which we think is quite consistent with our previous simple estimate.

Because by changing  $\Gamma$  in the stratosphere to almost one third of its original value only introduces about 30% of the change in the response; as a result, as long as  $\Gamma$  and  $\bar{u}$  stays within their reasonable ranges, solutions in the stratosphere will not be too sensitive to their respective values.

### ***3) Profiles of Q and Mc***

Two sets of profiles were used in this study. In order to test the sensitivity of results to the distributions of  $M_c$  and Q, several cases are run with either  $M_c$  or Q "switched" to the profile of the other region while leaving everything else unchanged.

We found that in the troposphere, the switching of  $M_c$  has only a small effect on the solution. We think this is an indirect proof to show that cumulus friction is not important for gravity waves; since if it were not the case, any change in  $M_c$  should translate its influence onto the solution. On the other hand, switching Q produced larger changes in T and u. This is due to the fact that as

long as the vertical scale of Q is broader than that of the gravity wave, solution of w is dominated by the direct response to Q (see Appendix), from the wave heat equation, the rate of temperature change (and temperature consequently) is the small residual between those two larger terms which nearly cancel each other out (hence the sensitivity of T to Q). u is approximately proportional to dw/dz, its sensitivity to Q's distribution is also expected (since a vertical derivative of w is involved).

Near the cloud top and in the stratosphere, response of smaller amplitude generally occurs when  $M_c$  of GATE is used. This is probably owing to the fact that for the GATE profile,  $dM_c/dz$  is larger (compare Figure 3.7 with 3.8) near the cloud top; therefore exerting more friction on the solution than the other profile does. Note that, however, one can not in a similar fashion claim that the viscous case should have smaller response at the cloud top than the inviscid case. Consider the horizontal wave momentum equation (viz. (3.5)):

$$-i\hat{\omega}u + \bar{w}\frac{du}{dz} + w\frac{d\bar{u}}{dz} = -ik\phi + A\frac{d}{dz}[\bar{M}_c(u - u_c) + M_c(\bar{u} - \bar{u}_c)] + \nu\frac{d^2u}{dz^2}. \quad (4.10)$$

It is obvious that the term behaving physically like Rayleigh friction,  $(dM_c/dz)u$ , is not the only extra term associated with cumulus friction, there also exist other terms such as  $M_c(du/dz)$  which may affect the solution as well. Under this circumstance, a prediction concerning the magnitude of responses near the cloud top based only on the presence or absence of a "Rayleigh friction term" is likely to be incorrect.

#### 4) Zonal wavelength

We again consider the inviscid hydrostatic gravity wave as an illustrating example. The vertical structure equation of  $w$ , which is

$$\frac{d^2w}{dz^2} - \frac{dw}{dz} + \left[ \frac{R\Gamma}{(c-\bar{u})^2} + \frac{(\bar{u}_{zz} + \bar{u}_z)}{(c-\bar{u})} \right] w = \frac{RQ}{(c-\bar{u})^2}, \quad (4.11)$$

does not depend on the zonal wavelength ( $L_x$ ). Moreover, both the lower (see (4.5)) and the upper<sup>1</sup> boundary conditions do not depend on  $L_x$  either. Therefore, the vertical structure of  $w$  should be independent of  $L_x$ . From the heat equation (3.7), the time rate of temperature change is also independent of  $L_x$ .

However, amplitudes of  $u$  and  $T$  are proportional to  $L_x$ , and this can be shown from the continuity equation (3.6),

$$u \sim \frac{i}{k} \frac{dw}{dz} \Rightarrow u \propto L_x. \quad (4.12)$$

It follows that the momentum flux averaged over one wavelength is also proportional to  $L_x$  on account of the dependence of  $u$  on  $L_x$ . Since from (4.2) the intermittency factor for the monochromatic wave is only a function of  $P_{sw}$  and  $\bar{P}$ ,  $(\rho u w)_{\text{global}}$  should also be proportional to  $L_x$ .

The above statements, which are based on the inviscid gravity wave, are still found approximately correct for the viscous case, when weakly  $L_x$ -dependence will be introduced into the vertical structure equation (viz. (3.11)).

---

<sup>1</sup> The radiation upper boundary condition depends only on the values of the static stability and  $lc-\bar{u}$ .

## 4.2 Gaussian Precipitation

Assume the precipitation to have the following localized Gaussian distribution:

$$P = P_0 \exp[-(x/x_0)^2]. \quad (4.13)$$

The approach here is still to consider the problem linear, Fourier decompose the precipitation, consider the response to individual harmonics, and through the resynthesis to obtain the final result. There are two ways of doing the decomposition, namely, Fourier transform and Fourier series methods. The first method reckons the precipitation as a single bump in an infinite domain, a continuous spectrum of harmonics will be obtained in the Fourier space. However, in the following calculation, the second approach will be adopted because it is relatively easier and more economical to be carried out. For the Fourier series method, a hypothetical domain ( $M$ ) which is much larger than  $x_0$  is imposed, a discrete, infinite spectrum of harmonics are obtained; however, for practical reason, the series is truncated. How many terms to keep before the truncation depends on the ratio between  $M$  and  $x_0$ .

A note of warning is in order if the method of Fourier series is to be used, because for some fields, results using  $M \rightarrow \infty$  do not necessarily converge to those obtained from the Fourier transform method. To begin with, since the forcing still dominates the response of  $w$  in the interior of the troposphere, it should be anticipated that the horizontal structure of  $w$  is also very close to a Gaussian distribution. From the mass continuity equation, the horizontal structure of  $u$  is close to an Error function which is the integral of a Gaussian distribution. If properly normalized, an Error function will assume values of  $+1$  and  $-1$  respectively when  $+\infty$  and  $-\infty$  are approached. However, one of the basic assumptions of Fourier series is the implied periodicity of the field over  $M$ . Therefore,  $u$ , and  $T$  in a similar way, obtained from the Fourier series method



will be distorted and should not be taken seriously for regions away from the center of the precipitation. Fortunately,  $w$  does not suffer from the same problem, it is always very concentrated about the center of the precipitation. When the momentum flux, which is a quantity of considerable interest here, is calculated, it will not be affected by the distortion in the  $u$  field.

### *a. Description of solutions*

#### *1) In the cloud layer*

As previously described, we will use (4.13) with  $P_0 = 60$  cm/day and  $x_0 = 10$  km to define the precipitation distribution.

Two typical viscous cases were chosen to be displayed in Figure 4.5 (Marshall Islands profiles, with  $c = -13$  m/s) and Figure 4.7 (GATE profiles, with  $c = -11$  m/s). Their respective inviscid counterparts are shown in Figures 4.6 and 4.8. Unlike the monochromatic case, full solutions as opposed to only the vertical structures are shown in an  $x$ - $z$  plane. In addition to the fields of  $T$ ,  $u$  and  $w$ , (frames (a), (b) and (c)), we have also included the streamline pattern *relative to the squall line* (frames (d)).

We notice that results using the localized precipitation have magnitudes noticeably larger, especially in the stratosphere, than those of the monochromatic case; although, over either one wavelength of the monochromatic precipitation

or the hypothetical domain of the localized precipitation, roughly the same horizontally integrated precipitation is realized. This is because that there exists a larger local variance for the present case.

One is not surprised that, because  $w$  more or less reflects the heat source directly, its horizontal distribution follows closely to that of the precipitation. For  $u$  and  $T$ , there seems always a dipole structure in the horizontal which is roughly antisymmetric about the center of the precipitation. This is reminiscent of the Error function described earlier. Again, associated with this is a note of warning that, because of the distortion resulting from trying to satisfy the periodic boundary condition, we should not take results for  $u$  and  $T$  too seriously away from the center of the precipitation.

The streamline patterns relative to the squall line shown in frames (d) of Figures 4.5-4.8 bear a rough resemblance to that for the idealized case shown in Figure 1.1 (thin dashed lines); although a better agreement will have been obtained if the value of  $P_0$  were increased.

Table 4.5 shows the composite of the result in the interior of the troposphere for all cases investigated. As before, for each field we have presented its average amplitude and the associated range. Owing to the fact that in the cloud layer  $w$  is mainly determined by the forcing, variation in  $w$  among different cases has been omitted. From the statistics shown in Table 4.5, it is evident that the inclusion of cumulus friction again does not introduce any significant or consistent change to the solution. Nevertheless, it is also found that within a squall line system, most (typically 80%) of the mean momentum

transport in the troposphere can be explained by the cloud transport which was defined in (4.1). The most prominent mean flux contributor is, as before, attributable to the mean cloud activity  $(-\overline{M}_c(\overline{u} - \overline{u}_c))$ .

Given such a concentrated precipitation, validity of linearization is under doubt and has to be checked *a posteriori*. This is done by comparing the amplitudes of  $(\partial/\partial t + \overline{u}\partial/\partial x)u$  and  $u\partial u/\partial x$  after obtaining the linear solution. It is found out that as a rule the first term is still larger than the other (although not as significantly as in the monochromatic case).

## ***2) Near the cloud top and/or above the cloud layer***

A more regular structured and more closely spaced contours compared to the ones in the cloud layer are observed above the cloud layer from frames (a) and (b) of Figures 4.5-4.8. This is an indication of the radiation boundary condition and an obviously more stable environment in the stratosphere which tends to make the vertical scale of waves shorter.

Table 4.6 summarizes the the same information<sup>1</sup> as in Table 4.5, except that it is now for the lower stratosphere (~15 km). Because of the sensitive nature of the leakage, larger variations among different cases were observed in the above-cloud region. We will, however, soon show that accounting for wave breaking near the cloud top will reduce the variations.

---

<sup>1</sup> It should be emphasized that the statistics shown in Table 4.6 are all *unmodified*. In other words, results, being obtained directly from the gravity wave calculation, have not been subject to any modifications due to other possible physical processes such as wave breaking.

When calculating the *global* effect of the momentum flux leakage associated with these waves into the stratosphere, we must again take into account the *intermittency factor* ( $f$ ). To be more specific,  $(\rho w)_{\text{global}}$  in Table 4.6 is obtained by taking the average of  $\rho w$  over the hypothetical domain ( $M$ ) and multiplying by  $f$  to obtain the final result. The intermittency factor for the Gaussian precipitation is defined as (cf. (4.2)):

$$f = r \frac{P_{\text{ave}} A_e}{P_0 x_0 \sqrt{\pi}} \frac{M}{A_e}, \quad (4.14)$$

where  $A_e$  is the length of the latitude circle,  $P_{\text{ave}}$  is the global mean precipitation,  $P_0$  and  $x_0$  are defined in (4.13), and  $r$  is the fraction of  $P_{\text{ave}}$  accounted for by squall lines. Therefore,  $(P_{\text{ave}} A_e)/(P_0 x_0 \sqrt{\pi})$  represents the number of lines needed to account for  $P_{\text{ave}}$ , while  $(M/A_e)$  denotes the fractional coverage of the latitude circle by a single squall line. Given  $r = 0.5$ ,  $P_{\text{ave}} = 0.6$  cm/day,  $P_0 = 60$  cm/day,  $x_0 = 10$  km, and  $M = 200$  km,  $f \approx 0.0564$ .

Because of the presence of a large variation of the static stability across the cloud top, temperature ( $T$ ) also has a large variation across that interface. Therefore, statistics of  $T$  shown in Table 4.6 are not representative of those immediately below the cloud top. Below the cloud top, the average magnitude of  $T$  is  $1$  °C and the associated range is  $0.6 \sim 1.8$  °C. Again, we will soon come back to the implications of this and the possible modification of the result shown in Table 4.6.

### 3) *Wave breaking below the cloud top*

In order to simplify the discussion, geometric coordinates will be used in the following.

Following Lindzen (1981), when the total (mean plus perturbation) temperature lapse rate becomes convectively unstable, namely,

$$\frac{dT}{dz} \geq \frac{d\bar{T}}{dz} + \frac{g}{c_p} \equiv \Gamma, \quad (4.15)$$

one expects the breaking of waves and the onset of turbulence. Wave breaking effectively limits any further growth of wave amplitudes (Lindzen, 1981, 1988). Associated with wave breaking is the wave momentum convergence or divergence and the mean flow acceleration. It should be emphasized that in order for waves to break, (4.15) does not have to be satisfied everywhere in the domain; however, the influence of the associated stress and the mean flow acceleration will conceivably be spread to a much broader area and not to be limited to regions where (4.15) is satisfied.

As mentioned previously, the localized precipitation results in larger temperature perturbations. In addition, the low mean static stability is normally observed in the tropical upper troposphere. These lead inevitably to *wave breaking in some local areas*.

In regions near and below the cloud top where the thermal forcing vanishes and the radiation boundary condition holds, we can estimate the vertical derivative of T as the product of T itself and the characteristic local vertical wave number  $\lambda = N / |c - \bar{u}|$ , where  $N^2 = (g/\bar{T})\Gamma$  and  $\Gamma$  is defined in (4.15). There-

fore, (4.15) can be rewritten as:

$$\lambda |T| \geq \Gamma \Rightarrow \frac{N}{|c - \bar{u}|} |T| \geq \frac{\bar{T} N^2}{g} \Rightarrow |T| \geq \frac{\bar{T}}{g} |c - \bar{u}| N. \quad (4.16)$$

In the tropical upper troposphere,  $N$  is  $\approx 5 \cdot 10^{-3} \text{ s}^{-1}$  ( $\Gamma \approx 1 \text{ }^\circ\text{C/km}$ ), and an easterly jet with magnitude around 8 m/s is frequently observed; hence, a reasonable range of  $|c - \bar{u}|$  for squall lines is from 2 to 5 m/s. Using (4.16), one sees that the upper bound of  $|T|$  for breaking to occur is between 0.2 and 0.6  $^\circ\text{C}$  with a typical value of 0.4  $^\circ\text{C}$ . Most values of  $T$  below the cloud top (0.6 ~ 1.8  $^\circ\text{C}$ ) obtained from our model results are beyond this limit, implying that wave breaking will have occurred before waves propagated into the stratosphere. It has to be stressed that the above estimate concerning the upper bound of  $|T|$  depends very much on the value of  $|c - \bar{u}|$ , and obviously, the smaller the value of  $|c - \bar{u}|$  is, the easier for waves to break.

Although the total field satisfies the condition for wave breaking, *individual Fourier components do not*. Recall that for the single wave case, wave amplitudes were not large enough to break near the cloud top as well. Schoeberl (1985) also discussed the importance of wave superposition when studying the wave breaking phenomenon.

If gravity waves forced by the localized precipitation do break in the upper troposphere, one can further estimate the accompanying acceleration on the mean flow. Near the cloud top where cumulus heating ceases, if the breakdown of gravity waves is temporarily ignored, according to the Eliassen-Palm theorem, the momentum flux density is non-divergent. From Table 4.6, we, therefore, argue that the average of  $(\rho u w)_{\text{global}}$  below the cloud top is also ~

$10^{-3}$  Pa. The dissipation associated with wave breaking is assumed to limit any further growth of wave amplitudes, i.e.

$$\frac{d}{dz} \overline{u'w'} = 0. \quad (4.17)$$

In regions where wave breaking occurs, the mean flow acceleration to a first approximation can then be expressed as:

$$-\frac{1}{\rho} \frac{d}{dz} \overline{\rho u'w'} \sim \frac{1}{H} \overline{u'w'}, \quad (4.18)$$

$H$  being the scale height. As a result, it is estimated that the *zonally averaged* acceleration associated with breaking gravity waves below the cloud top is  $\sim 0.05$  m/s/day. As far as the *local* acceleration due to a single squall line is concerned (namely, not taking into account the intermittency), it can be as large as 1 m/s/day. It should again be stressed that this acceleration in the upper troposphere is under a great deal of variation attributed to the delicate nature of the leakage of wave activity outside the forcing region.

Knowing that gravity waves resulting from the localized precipitation do break below the cloud top before they propagate into the stratosphere forces us to reconsider the results shown in Table 4.6. In particular, even though, due to the delicate nature of the the response outside the forcing region (because of interference, see Appendix), it is difficult to predict exactly how much energy can escape out of the cloud layer; however, invoking the breaking mechanism reduces the degree of variation since breaking limits the possible amplitudes.

As previously mentioned, one of the basic assumptions in Lindzen (1981, 1988) shows that once the breaking condition is satisfied, turbulence and the

accompanying wave dissipation will act in such a way as to limit any further growth of wave amplitudes<sup>1</sup>. According to our previous estimate, 0.4 °C is probably the typical upper bound of  $|T|$  limited by wave breaking. Compared to the average  $|T|$  of 1 °C, which was obtained directly from numerical results for regions below the cloud top, only about 40% of the original wave being able to get through the breaking region is implied. Because the momentum flux is a quadratic quantity, it follows that 16% out of  $-10 \cdot 10^4$  Pa for  $(\rho w)_{\text{global}}$  (see Table 4.6) will be actually realized in the stratosphere. As a consequence, we estimate that  $-1.6 \cdot 10^4$  Pa is a reasonable climatological measure of the stress observed in the stratosphere on a global scale caused by thermally forced gravity waves (or squall lines) originating from the troposphere. Interestingly enough, this is not too different from the value of  $(\rho w)_{\text{global}}$ , which is  $-1.3 \cdot 10^4$  Pa (see Table 4.2), for the monochromatic precipitation without the presence of wave breaking near the cloud top. In view of this, we are going to assume *in this study* that immediately above the cloud top, the appropriate amplitude for the vertical velocity perturbation ( $w$ ) can be described as about 1.0 cm/sec (see Table 4.2) with a horizontal scale of 200 km. Given the amplitude and the scale, one can further calculate the possible secondary breaking level and the associated mean flow acceleration using the linear parameterization scheme of Lindzen (1981) for the monochromatic wave.

Our results also show that although breaking may have occurred below the cloud top, once waves escape into regions immediately above the cloud layer

---

<sup>1</sup> Strictly speaking, Lindzen (1988) points out due to the supersaturation of the vertically propagating internal gravity wave, the cessation of wave growth with height is gradual rather than instant.



with a typical  $|w|$  of 1.0 cm/sec and a wavelength of 200 km, the breaking condition is no longer satisfied. Lindzen (1985) pointed out that an increase of  $|c - \bar{u}|$  may sometimes be able to *locally* counteract the effect of the density stratification in such a way as to make the breaking gravity wave cease breaking. In this study, however, the main reason for gravity waves to stop breaking as they leave the troposphere is probably attributed to the sudden increase of static stability in the lower stratosphere.

The mean zonal flow in the tropical lower stratosphere is subject to the influence of the quasi-biennial oscillation (QBO), and only under favorable condition, namely, in the absence of critical level, can gravity waves propagate higher up into the middle atmosphere. Some characteristic stratospheric mean zonal wind profiles are shown in Figure 4.9, corresponding to different phases of QBO. These  $\bar{u}$  profiles have been used to study where the gravity wave leaving the troposphere breaks for the second time. Among cases<sup>1</sup> investigated, the secondary breaking levels for the gravity wave range from 20 to 35 km or so, some of them are due to the density stratification (e.g. profile A of Figure 4.9), and some are simply due to the proximity to a critical level (e.g. profile B of Figure 4.9). The associated zonally averaged mean flow acceleration ranges from 0.1 to 0.8 m/s/day. For instance, given a gravity wave leaving the cloud top with  $|w| = 1$  cm/s, wavelength = 200 km, and  $c = -11$  m/s; for profile A of Figure 4.9, the gravity wave breaks around 36 km with the associated acceleration on the mean flow of 0.8 m/s/day toward the west; for profile D, wave breaking occurs at 22 km with the acceleration of 0.2 m/s/day; and for profile E,

---

<sup>1</sup> Again, we have considered a range of phase speeds (10 to 13 m/s).

wave breaking takes place at 32 km with the acceleration of 0.3 m/s/day. Again, these secondary breaking statistics depend very much on the distribution of mean zonal flow.

### ***b. Sensitivity tests***

The choices of parameters  $P_0$ ,  $x_0$  and  $M$  are not unique, not mentioning even the functional form of the distribution of the precipitation itself. Hence, there is a need as to understand the possible variation of results associated with different choices of parameters.

First of all, since the momentum flux is proportional to  $P_0^2$ , and the intermittency factor  $f$  is proportional to  $1/P_0$ ,  $(\rho w)_{\text{global}}$  is proportional to  $P_0$  (given the rest of the parameters unchanged).

An hypothetical domain of finite width ( $M$ ) has been introduced in order to facilitate the calculation. Our results,  $(\rho w)_{\text{global}}$  in particular, should not be dependent on the choice of  $M$  as long as it is much larger than the scale of the precipitation. According to the discussion earlier, it is expected that while the numerical solution of  $w$  is reasonably accurate, the same is not true for  $u$  and  $T$  away from the center of the precipitation. In order to understand whether  $(\rho w)_{\text{global}}$  is really affected by the value of  $M$ , we have considered viscous cases with  $M = 200$  and 400 km. When  $M=200$  km, only the first 10 harmonics are kept, when  $M=400$  km, the series is truncated after the first 30 harmonics. In addition, both GATE and Marshall Islands profiles and  $c = -11$  m/s are used in the calculation. It is

discovered that different values of  $M$  do not cause any difference in  $w$ ; the same is also true for  $u$  and  $T$  not too far from the center of the precipitation. Table 4.7 shows that  $(\rho u w)_{\text{global}}$ , to a first approximation, is unaffected by the value of  $M$ .

### 4.3 Comparison with Mountain Waves

Using conventional large-scale meteorological observations, Newton (1971) calculated the torques produced by topography upon the atmosphere due to pressure differences between the eastern and the western sides of mountain ranges. The average yearly mountain torque from  $20^\circ\text{N}$  to  $20^\circ\text{S}$  is found to be of 0.5 "Hadley" units<sup>1</sup> which, after being converted to stress, is equivalent to  $3.5 \cdot 10^{-3}$  Pa. As previously noted that *in the upper troposphere* the zonally averaged stress caused by thermally forced gravity waves<sup>2</sup> before the breakdown is about  $10^{-3}$  Pa. In addition, in our model the zonally averaged mean flow acceleration associated with breaking gravity waves in the upper troposphere, 0.05 m/s/day, tends to be small as well. Therefore, we conclude that in the tropical upper troposphere, thermally forced gravity waves are probably not as dynamically important as mountain waves; although, the momentum flux due to the former is of the same order of magnitude as that due to the latter.

Similarly, the number of  $-1.6 \cdot 10^4$  Pa, which is the estimated value of the momentum flux being carried into the middle atmosphere on a global scale, probably does not mean very much by itself unless some kind of comparison is made. Lindzen (1984) has considered hydrostatic mountain waves where topography is characterized

---

<sup>1</sup> One "Hadley" unit is defined as  $10^{18}$  kg m<sup>2</sup> sec<sup>-2</sup> per  $5^\circ$  latitude belt which can be converted to stress in Pa by dividing by  $141 \cos^2\phi$ ,  $\phi$  being the latitude.

<sup>2</sup> Recall that near the cloud top, stress due to clouds is negligible.

by a single harmonic with an amplitude of 20 m/s and a wavelength around 1600 km. After further assuming that the Brunt-Väisälä frequency =  $2\pi/300$  sec and the surface mean wind  $\sim 10$  m/s, from equation (19) of Lindzen (1984), one can estimate the same quantity,  $(\rho u w)_{\text{global}}$ , due to mountain waves. It is found that for mountain waves the value of  $(\rho u w)_{\text{global}}$  at the tropopause is  $\sim 2.0 \cdot 10^4$  Pa. This is almost equal to we obtained from thermally forced gravity waves.

McFarlane (1987) examined the influence of large-scale momentum sinks due to the breaking of orographically excited gravity waves on the Northern Hemisphere wintertime circulation in the troposphere and the lower stratosphere using the Canadian Climate Center general circulation model (GCM). His results suggested that in the tropical troposphere and lower stratosphere, the zonally averaged westerly wind acceleration due to the orographic wave drag should be smaller than 0.5 m/s/day. Palmer et al. (1986) have also independently conducted an analysis somewhat similar to McFarlane (1987) using the British Meteorological Office general circulation and numerical weather prediction (GCM/NWP) models. His results indicated that in the tropical lower stratosphere, the acceleration on the mean flow resulting from the breaking of orographic gravity waves is smaller than 0.2 m/s/day. Using various mean zonal flow profiles, we have obtained values of the acceleration on the mean flow due to thermally excited gravity waves ranging from 0.1 to 0.8 m/s/day. This suggests that in the tropical lower stratosphere squalls may be a comparably important source compared to the topography.

## Chapter 5: Summary and Conclusions

Fast-moving cloud lines, or squall lines, in the tropics are treated as a gravity wave phenomenon generated by the latent heat release associated with the deep cumulus convection. Presented in this study is a simple diagnostic linear gravity wave model forced by a zonally propagating heat source with prescribed vertical distribution. Within such a system, attention has been paid especially to the momentum transport which takes place in both the troposphere and the stratosphere. In the troposphere in particular, this model, unlike the conventional aircraft measurements, enables us to isolate momentum transport contribution due to clouds from that due to gravity waves.

The physical process of cumulus friction (Schneider and Lindzen, 1976) is included in the wave momentum equation. The profile of cloud mass flux is obtained from the cumulus parameterization scheme of Lindzen (1981, 1988).

Due to both the modulation of convective activity by easterly waves and to the scale separation between squall lines and easterly waves, in our gravity wave model, we have assumed that the convergent phase of easterly waves to serve as the basic state for squall lines. Both the monochromatic and the localized distributions of precipitation are considered. With regard to the monochromatic precipitation, we have assumed that the amplitude of the perturbation precipitation and the mean precipitation both being equal to 4.8 cm/day. For the localized precipitation, a Gaussian distribution  $P_0 \cdot \exp[-(x/x_0)^2]$  with  $P_0 = 60$  cm/day and  $x_0 = 10$  km is used. It is found out *a posteriori* that for both distributions of the rainfall, linearity is basically a good approximation.

The following similar results from both the monochromatic and the localized precipitation are found:

1) In the troposphere, most of the mean momentum transport is accounted for by the mean cloud activity ( $-\overline{M_c(\bar{u} - \bar{u}_c)}$ ), the gravity wave transport ( $\overline{\rho \bar{u} \bar{w}}$ ) is found to be negligible.

2) Model results of the combined mean momentum fluxes in the troposphere by clouds and gravity waves are consistent, in both sign and magnitude, with the total mean momentum flux observed from the aircraft measurements for fast-moving cloud lines (LeMone, et al., 1984). In addition, the implication from those aircraft measurements indicating that most momentum flux in the cloud layer is achieved by the mean cloud activity is also confirmed in our analysis.

3) Partly due to the relatively short time scale associated with gravity waves (compared to that associated with cumulus friction), cumulus friction is not an important term in the wave momentum equation. This is verified by the almost identical results with and without cumulus friction. Through a more detailed examination, it is discovered that the unimportance of cumulus friction is also partly attributed to the fact that in the cloud layer the vertical advection of horizontal momentum by the mean cloud activity and that by the mean vertical velocity largely cancel each other out.

For the parameters chosen here, the perturbation temperature lapse rate for the case of the monochromatic precipitation has an average of 0.24 °C/km below the cloud base. This is far smaller than the local static stability parameters ( $d\bar{T}/dz + g/c_p$ ) which is  $\sim 1$  °C/km. Hence, gravity waves generated by the monochromatic precipitation do not break below the cloud base. For the localized precipitation, however, perturbations of larger amplitudes occur especially below the cloud top and in the stratosphere. For all cases investigated, it is noticed that the breakdown of gravity waves, i.e. the perturbation temperature lapse rate being greater than 1 °C/km, always takes place *somewhere* below the cloud top. As a result, gravity waves forced by the localized precipitation are subject

to breaking before they can escape to the stratosphere. However, similar to Schoeberl (1985), it is the synthesized wave field which satisfies the breaking condition, not the individual Fourier components. It is estimated that the mean flow acceleration associated with wave breaking below the cloud top has a *zonal average* of 0.05 m/s/day after considering the so-called intermittency factor for squall lines.

In the Appendix, we show that the momentum flux above the forcing region is very sensitive to small changes in the distribution of heating. However, assuming that the presence of wave breaking effectively limits the possible wave amplitudes (Lindzen, 1981 1988), the degree of variation of the leakage is greatly reduced. Interestingly enough, we found that at least for the parameters chosen in this study, both the localized precipitation (with wave breaking below the cloud top) and the monochromatic precipitation (without wave breaking below the cloud top) give rise to similar estimates for the possible gravity wave momentum flux escaping from the troposphere on a global scale. Assuming monochromatic waves, it is straightforward to calculate the secondary breaking level and the accompanying mean flow acceleration due to the vertically propagating gravity wave.

Compared to the mountain torques observations and other GCM/NWP studies, it is found out that thermally forced gravity waves have dynamic importance comparable to that of the topographic gravity waves; this seems to be particularly true for the lower stratosphere.

Therefore, despite the crudeness of the present model and the obvious uncertainty in various parameters, our results suggest strongly that the fluxes of momentum associated with squalls are likely to be important within the tropical stratosphere.

## Appendix

### Relation of Wave Leakage to the Distribution of Forcing

#### A.1 Formulation and solution of the problem

In this appendix, we examine in details how interference prevents significant leakage when forcing depth exceeds the vertical scale of gravity waves. Two previous related studies are by Green (1965) and Lindzen (1966).

Consider a thermally forced two-dimensional hydrostatic gravity wave in a static Boussinesq atmosphere with constant temperature stratification. The shape of the thermal forcing applied on the heat equation will be a simple sinusoidal profile in order to simplify the analytic solution. Log-pressure coordinates ( $z = -\log(p/p_0)$ ) will be used. The u-momentum, mass continuity and thermodynamic equations are:

$$\frac{\partial u}{\partial t} = -\frac{\partial \phi}{\partial x}, \quad \frac{\partial u}{\partial x} + \frac{\partial w}{\partial z} = 0, \quad \frac{1}{R} \frac{\partial}{\partial t} \frac{\partial \phi}{\partial z} + w\Gamma = Q,$$

respectively, where  $\Gamma = (d/dz + R/c_p)T$  is the constant static stability parameter, and  $Q$  is the heat source whose profile will be assumed to be sinusoidal. After assuming wavelike behavior in both time and the horizontal direction ( $\sim \exp[ik(x - ct)]$ ), the vertical structure equation for  $w$  can be easily derived. The radiation condition is applied above the forcing region, and the lower boundary condition will be assumed to have a fairly general form. In mathematical form, the equation and the associated boundary



conditions are:

$$\frac{d^2w}{dz^2} + \lambda^2 w = F, \quad z_c \leq z \leq z_t \quad (\text{A.1})$$

$$\frac{dw}{dz} + aw = 0, \quad z = z_c \quad (\text{A.2})$$

$$\frac{dw}{dz} - i\lambda w = 0, \quad z = z_t \quad (\text{A.3})$$

where

$\lambda$  : vertical wavenumber =  $(R\Gamma/c^2)^{1/2}$  = constant,

$c$  : phase speed (relative to a constant ambient flow),

$a$  : some constant depending on the kind of the lower boundary condition,

and  $F$  has the following form:

$$F = \lambda^2 \cdot \sin \frac{\pi}{\Delta} (z - z_a) \quad \text{for} \quad (z_c \leq z_a \leq z \leq z_b \leq z_t) \quad (\text{A.4})$$

and vanishes elsewhere, where  $\Delta = z_b - z_a$ . Strictly speaking, if  $Q = A \cdot \sin[\pi(z-z_a)/\Delta]$ ,

where  $A$  is some arbitrary amplitude constant,  $F$  should be equal to  $(\lambda^2/\Gamma)Q$ . However,

since  $\Gamma$  is a constant as well, thus both  $A$  and  $\Gamma$  are dropped completely in (A.4).

Our approach will be to construct the Green's function  $G(z;\xi)$  which satisfies the following:

$$\frac{d^2G}{dz^2} + \lambda^2 G = \delta(z;\xi), \quad z_c \leq z \leq z_t \quad (\text{A.5})$$

$$\frac{dG}{dz} + aG = 0, \quad z = z_c \quad (\text{A.6})$$

$$\frac{dG}{dz} - i\lambda G = 0, \quad z = z_i, \quad (\text{A.7})$$

together with the matching conditions at  $z = \xi$ :

$$G(\xi_+; \xi) = G(\xi_-; \xi), \quad (\text{A.8})$$

$$\frac{dG}{dz}(\xi_+; \xi) - \frac{dG}{dz}(\xi_-; \xi) = 1, \quad (\text{A.9})$$

such that the solution to (A.1)-(A.3) will be

$$w = \int_{z_c}^{z_i} G(x; \xi) F(\xi) d\xi \quad (\text{A.10})$$

where  $\delta$  is the Dirac delta function.

For  $z > \xi$  (region I),

$$G_I = A_1 e^{i\lambda z}, \quad (\text{A.11})$$

and for  $z < \xi$  (region II),

$$G_{II} = A_2 e^{i\lambda z} + B_2 e^{-i\lambda z}. \quad (\text{A.12})$$

Apply two matching conditions (A.8) and (A.9), following equations are obtained:

$$A_1 e^{i\lambda \xi} = A_2 e^{i\lambda \xi} + B_2 e^{-i\lambda \xi}, \quad (\text{A.13})$$

and

$$i\lambda A_1 e^{i\lambda \xi} - i\lambda A_2 e^{i\lambda \xi} + i\lambda B_2 e^{-i\lambda \xi} = 1. \quad (\text{A.14})$$

(A.13), (A.14) together with (A.6) yield

$$A_1 = \frac{i}{2\lambda} \left[ \frac{-i\lambda + a}{i\lambda + a} e^{i\lambda \xi} e^{-i2\lambda z_c} - e^{-i\lambda \xi} \right],$$

$$A_2 = \frac{i}{2\lambda} \frac{-i\lambda + a}{i\lambda + a} e^{i\lambda \xi} e^{-i2\lambda z_c},$$

$$B_2 = \frac{-i}{2\lambda} e^{i\lambda\xi}. \quad (\text{A.15})$$

Therefore, the solution for  $w$  from (A.10) is:

$$\begin{aligned} w &= \int_{z_a}^{z_b} G(z;\xi)F(\xi)d\xi \\ &= \int_{z_a}^z G_I F d\xi + \int_z^{z_b} G_{II} F d\xi \quad \text{for } z_a \leq z \leq z_b \end{aligned} \quad (\text{A.16})$$

$$= \int_{z_a}^{z_b} G_{II} F d\xi \quad \text{for } z_c \leq z \leq z_a \quad (\text{A.17})$$

$$= \int_{z_a}^{z_b} G_I F d\xi \quad \text{for } z_b \leq z \leq z_t \quad (\text{A.18})$$

After some manipulations, (A.16), (A.17) and (A.18) become

$$\begin{aligned} w &= \frac{\lambda^2}{\lambda^2 - (\frac{\pi}{\Delta})^2} \sin \frac{\pi}{\Delta} (z - z_a) \\ &+ \frac{\lambda}{2i} \frac{\frac{\pi}{\Delta}}{\lambda^2 - \frac{\pi^2}{\Delta}} \left\{ \left( e^{i\lambda z_b} + e^{i\lambda z_a} \right) \left( \frac{a - i\lambda}{a + i\lambda} e^{-2i\lambda z_c} \right) e^{i\lambda z} - e^{-i\lambda z_a} \left[ e^{i\lambda(z_a + z_b)} e^{-i\lambda z} + e^{i\lambda z} \right] \right\}, \\ &\quad \text{for } z_a \leq z \leq z_b \end{aligned} \quad (\text{A.19})$$

$$\begin{aligned} w &= \frac{\lambda}{2i} \frac{\frac{\pi}{\Delta}}{\lambda^2 - (\frac{\pi}{\Delta})^2} \left\{ \left( e^{i\lambda z_b} + e^{i\lambda z_a} \right) \left( \frac{a - i\lambda}{a + i\lambda} e^{-2i\lambda z_c} \right) e^{i\lambda z} - \left( e^{i\lambda z_b} + e^{i\lambda z_a} \right) e^{-i\lambda z} \right\}, \\ &\quad \text{for } z_c \leq z \leq z_a \end{aligned} \quad (\text{A.20})$$

$$\begin{aligned} w &= \frac{\lambda}{2i} \frac{\frac{\pi}{\Delta}}{\lambda^2 - (\frac{\pi}{\Delta})^2} \left\{ \left( e^{i\lambda z_b} + e^{i\lambda z_a} \right) \left( \frac{a - i\lambda}{a + i\lambda} e^{-2i\lambda z_c} \right) e^{i\lambda z} - \left( e^{-i\lambda z_b} + e^{-i\lambda z_a} \right) e^{i\lambda z} \right\} \\ &\quad \text{for } z_b \leq z \leq z_t \end{aligned} \quad (\text{A.21})$$

respectively. It is obvious from (A.21) that because the radiation condition has been applied, amplitude of  $w$  above  $z_b$  will not change with height. The two terms on the right of (A.19) represent contributions from the particular and homogeneous solutions respectively. Solution at  $z_b$ , which is an indicator of the wave activity outside the source region, can be obtained from either (A.19) or (A.21), and is

$$w(z_b) = \frac{\lambda}{2i} \frac{\frac{\pi}{\Delta}}{\lambda^2 - (\frac{\pi}{\Delta})^2} \left( e^{i\lambda z_b} + e^{i\lambda z_a} \right) \left[ \frac{a - i\lambda}{a + i\lambda} e^{i\lambda(z_b - 2z_c)} - e^{-i\lambda z_a} \right]. \quad (\text{A.22})$$

Equations (A.19), (A.20) and (A.21) have been derived using a rather general lower boundary condition (A.2). If one decides to consider a rigid bottom such that the lower boundary condition is  $w=0$ , (A.19)-(A.21) can be proved to be still valid after letting the parameter "a" approach to  $\infty$ . In fact, when "a" becomes very large, (A.2) can be simply approximated as  $w=0$ . Another possibility is that if energy is to be radiated away from the lower boundary (and in a direction away from the source region of course), the proper solution will then be given by (A.19)-(A.21) after replacing "a" with  $i\lambda$ .

## A.2 Discussion

Consider cases when

$$\lambda^2 \gg (\pi/\Delta)^2. \quad (\text{A.23})$$

Physically, this means that the vertical scale of the forcing is much broader than the vertical scale that a free gravity wave would have. In the tropics,  $\Gamma$  is  $\sim 20^\circ\text{C}$  which corresponds to a Brunt-Väisälä frequency of  $2\pi/10\text{min}$ , and the scale of the heating  $\Delta$  is typically 1.5 corresponding to a heat source extending over the depth of the troposphere. It can then be shown that as long as the phase speed is much smaller than

36 m/s, (A.23) will be valid. For tropical squall lines,  $c < 36$  m/s is easily satisfied. Furthermore, it is evident that if (A.23) holds, in the interior of the forcing region, the first term on the right of (A.19) will dominate over the second term, and (A.19) can be approximated as

$$w \sim \sin \frac{\pi}{\Delta} (z - z_a). \quad (\text{A.24})$$

(A.24) is simply the solution to (A.1) without considering the curvature term, or from another point of view, it indicates the balance between the adiabatic ascent and the diabatic heating in the heat equation<sup>1</sup>. Therefore, as long as the scale of the forcing is broad compared to that of the wave, one anticipates that in the interior of the forcing region, to a first approximation, the solution for  $w$  follows closely to the distribution of the forcing.

When (A.23) holds, (A.22) shows that the wave activity outside the forcing region will be very small due to the presence of the interference. As a matter of fact, we have to take this opportunity to point out that the interference is a very delicate and sensitive process. To illustrate this point in more details, consider the simple case when  $w=0$  is the lower boundary condition, and focus on the solution at  $z_b$  (viz. (A.22)). The controlling factor of (A.22) can be written as

$$E(\lambda, \Delta) = (\lambda\pi/\Delta)/[\lambda^2 - (\pi/\Delta)^2]. \quad (\text{A.25})$$

As long as (A.23) holds,  $E$  decreases monotonically with increasing value of  $\lambda$  (or decreasing value of the gravity wave vertical scale). In other words, the broader scale the forcing has, the less the leakage will be. However,  $E$  is not the only factor which

---

<sup>1</sup> Strictly speaking, this means that  $w\Gamma = \sin(\pi(z-z_a)/\Delta)$ . Since  $\Gamma$  is a constant, and is therefore omitted from the discussion.

determines the result. For instance, there is another term  $\exp(i\lambda z_b) + \exp(i\lambda z_a)$  on the right of (A.22), and this term vanishes under the following condition:

$$\lambda(z_b - z_a) = (2n + 1)\pi \quad n = 0, \pm 1, \pm 2, \dots \quad (\text{A.26})$$

Physically, this means that a perfect cancellation of wave activity outside the forcing region. As a result, the monotonic dependence of the leakage on the gravity wave vertical scale ((A.25)) is distorted by the presence of the other terms.

Let's now consider the case when the heat source is defined as  $Q = \sin(\pi(z-2\text{km})/10\text{km})$  for  $z \in (2, 12 \text{ km})$ , and vanishes otherwise<sup>1</sup>, Figure A.1 shows the magnitudes of  $w$  at the top of the domain (60 km in the present case) for different gravity wave vertical scales<sup>2</sup> ( $L_z$ , in km) relative to the case when  $L_z/10 \text{ km} = 0.1$ , in which case the magnitude of  $w$  at 60 km is set arbitrarily to one. It is obvious that, for increasing value of  $L_z/10 \text{ km}$ , while still keeping (A.23) valid, larger leakage is not necessarily yielded. As a consequence, if a typical magnitude of the wave activity outside the forcing region were required, in view of the oscillations shown in Figure A.1, choosing a single value of  $c$  (or a single vertical scale of the gravity wave accordingly) instead of a range will be sometimes misleading.

The presence of oscillations can in fact be shown to be partly due to the no-slip lower boundary condition  $w=0$ . Figure A.2 shows the same experiment but with the radiation condition imposed at the lower boundary. Most oscillations are gone! Owing to the fact that the lower boundary condition in the analysis of squall lines is indeed

---

**1** Distribution of the heat source will all be expressed in the geometric coordinates for the sake of ease of discussion.

**2** From (A.1), if expressed in the log-pressure coordinates,  $L_z$  is simply  $1/\lambda$ .

close to  $w=0$ ; therefore, it is concluded that a range of phase speeds has to be considered in order to have a reasonable representation of the leakage in the stratosphere.

A sinusoidal heating profile is by no means the only choice, another choice will be a Gaussian profile  $\exp[-((z-z_0)/\Delta)^2]$  which was used by Lindzen (1966). He showed that as long as (A.23) holds and the major part of the forcing does not intersect with the boundaries, the wave activity outside the source region will be very small as well. As a matter of fact, assuming the response in the source region is  $\sim O(1)$ , for the sinusoidal heating profile, responses away from the forcing region are  $\sim O(L_s/\Delta)$  (viz. (A.22)), while for the Gaussian heating profile, they can be shown to be  $\sim O(\exp[-(\Delta/L_s)^2/4])$ . It is evident that for the latter case, the leakage detected outside the source region will be even smaller. Nevertheless, the oscillatory phenomenon in leakage as  $L_s/\Delta$  varies still exists. In a similar fashion, the oscillation is almost completely removed by imposing the radiation lower boundary condition. Figure A.3, which is similar to Figure A.1, shows the result with a heat source  $Q = \exp(-((z-7\text{km})/4\text{km})^2)$ . Note that both the definition and range of the abscissa are somewhat different from Figure A.1. Figure A.4 shows the case when the radiation lower boundary condition is applied. Another more dramatic example with heat source  $Q = \exp(-((z-30\text{km})/10\text{km})^2)$  is presented in Figures A.5 (no-slip lower boundary condition) and A.6 (radiation lower boundary condition). Ignoring different scales of the ordinate (or under a proper normalization in other words), results from both Figures A.4 and A.6 show the identical functional dependence on  $L_s/\Delta$ . Moreover, a closer look of those two figures indicates that the maximum leakage always occurs at  $L_s/\Delta = 1/\sqrt{2}$ , this is consistent with what has been predicted by Lindzen (1966).

We have also conducted similar experiments using real heating profiles such as those presented in Figures 3.7 and 3.8, and even with vertically varying zonal winds. It is found out that as long as the effective lower boundary condition is close to  $w=0$ , the same oscillatory phenomenon always occurs; although it might not be as severe as the sinusoidal or the Gaussian cases. In any event, in order to have smaller radiation out of the source region, following rules of thumb still hold:

1. Broader scale of the source compared to the scale of waves.
2. Heating is as symmetric as possible.

Finally, it has already been stated that in the interior of the forcing region,  $w$  is dominated by the direct response to the forcing as long as the scale of the forcing is reasonably broad. Another way of looking at this is by observing the ratio between the two terms, which represent the particular and homogeneous solutions, on the right of (A.19),

$$w_h/w_p \sim O(\lambda\pi/\Delta). \quad (\text{A.27})$$

It is obvious that the above ratio is much smaller than unity when (A.23) is satisfied. However, the same conclusion is not equally true for the other fields such as horizontal velocity ( $u$ ) and temperature ( $T$ ). Take  $u$  for example. From the continuity equation,

$$u \propto dw/dz. \quad (\text{A.28})$$

Then from (A.19) and (A.28), the analogue to (A.27) for  $u$  is:

$$u_h/u_p \sim O(1). \quad (\text{A.29})$$

Same result for  $T$  can also be derived. As a consequence, although for the broad forcing,  $w$  is dominated by the direct response to the forcing; but for the other fields such as  $u$  and  $T$ , equally important contributions from both the particular and homogeneous parts of the solution are expected.



## References

- Arakawa, A. and W. H. Schubert, 1974: Interaction of a cumulus cloud ensemble with the large scale environment, Part I. *J. Atmos. Sci.*, **31**, 674-701.
- Augstein, E., H. Schmidt and F. Ostapoff, 1974: The vertical structure of the atmospheric planetary boundary layer in undisturbed trade winds over the Atlantic ocean. *Boundary-Layer Meteor.*, **6**, 129-150.
- Barnes, G. M. and K. Sieckman, 1984: The environment of fast- and slow-moving tropical mesoscale convective cloud lines. *Mon. Wea. Rev.*, **112**, 1782-1794.
- Bender, C. M. and S. A. Orszag, 1978: *Advanced mathematical methods for scientists and engineers*. McGraw-Hill Inc., 593pp.
- Bolton, D., 1980: Application of the Miles theorem to forced linear perturbations. *J. Atmos. Sci.*, **37**, 1639-1642.
- Booker, J. R. and F. P. Bretherton, 1967: The critical layer for internal gravity waves in a shear flow. *J. Fluid Mech.*, **27**, 513-539.
- Burpee, R. W. and R. J. Reed, 1982: Chapter 4, Synoptic-scale motions. *GARP publication series*, No.25, 61-120.
- Cho, H.-R. and Y. Ogura, 1974: A relationship between cloud activity and the low-level convergence as observed in Reed-Recker's composite easterly waves. *J. Atmos. Sci.*, **31**, 2058-2065.
- Cho, H.-R., 1985: Rates of entrainment and detrainment of momentum of cumulus clouds. *Mon. Wea. Rev.*, **113**, 1920-1932.

- Davies, H. C., 1979: Phase-lagged wave-CISK. *Quart. J. Roy. Meteor. Soc.*, **105**, 325-353.
- Eliassen, A. and E. Palm, 1960: On the transfer of energy in stationary mountain waves. *Geophys. Norvegica*, **22**, 1-23.
- Flatau, M. and D. E. Stevens, 1987: The effect of horizontal pressure gradients on the momentum transport in tropical convective lines. Part I. *J. Atmos. Sci.*, **44**, 2074-2087.
- Geleyn, J.-F., C. Girard, J.-F. Louis, 1982: A simple parameterization of moist convection for large-scale atmospheric models. *Beitr. Phys. Atmos.*, **55**, 325-334.
- Green, J. S. A., 1965: Atmospheric tidal oscillations: an analysis of the mechanics. *Proc. Roy. Soc.*, **A288**, 564-574.
- Hamilton, K. 1983: Diagnostic study of the momentum balance in the northern hemisphere winter stratosphere. *Mon. Wea. Rev.*, **111**, 1434-1441.
- Holton, J. R. and R. S. Lindzen, 1972: An updated theory of the quasi- biennial cycle of the tropical stratosphere. *J. Atmos. Sci.*, **29**, 1076-1080.
- Holton, J. R., 1979: *An introduction of dynamic meteorology*. Academic Press. 391pp.
- Holton, J. R., 1982: The role of gravity wave induced drag and diffusion in the momentum budget of the mesosphere. *J. Atmos. Sci.*, **39**, 791-799.
- Holton J. R., 1983: The influence of gravity wave induced drag and diffusion in the momentum budget of the mesosphere. *J. Atmos. Sci.*, **39**, 2497-2507.

- Holton J. R., and X. Zhu, 1984: A further study of gravity waves induced drag and diffusion in the mesosphere. *J. Atmos. Sci.*, **41**, 2653-2662.
- Houze, R. A. Jr., 1977: Structure and dynamics of a tropical squall-line system. *Mon. Wea. Rev.*, **105**, 1540-1567.
- Houze, R. A. Jr. and A. K. Betts, 1981: Convection in GATE. *Rev. of Geophys. and Space Phys.*, **19**, 541-576.
- Houze, R. A. Jr., 1982: Cloud clusters and large-scale vertical motions in the tropics. *J. Meteor. Soc. Japan*, **60**, 396-410.
- Klemp and Lilly, 1980: Mountain waves and momentum flux. *Orographic Effects in Planetary Flows*, GARP publication series, No. 23, Chapter 4. World Meteorological Organization.
- Leary, C. A. and R. A. Houze Jr., 1979: Melting and evaporation of hydrometeors in precipitation from the anvil clouds of deep tropical convection. *J. Atm. Sci.*, **36**, 669-679.
- Leary, C. A. and R. A. Houze Jr., 1980: The contribution of mesoscale motions to the mass and heat fluxes of an intense tropical convective system. *J. Atmos. Sci.*, **37**, 784-796.
- LeMone, M. A., 1983: Momentum transport by a line of cumulonimbus. *J. Atmos. Sci.*, **40**, 1815-1834.
- LeMone, M. A., G. M. Barnes and E. J. Zipser, 1984: Momentum flux by lines of cumulonimbus over the tropical oceans. *J. Atmos. Sci.*, **41**, 1914-1932.

Lilly, D. K., 1972: Wave momentum flux - a GARP problem. *Bull. Amer. Meteor. Soc.*, **53**, 17-23.

Lindzen, R. S., 1966: On the relation of wave behavior to source strength and distribution in a propagating medium. *J. Atmos. Sci.*, **23**, 630-632.

Lindzen, R. S. and J. R. Holton, 1968: A theory of the quasi-biennial oscillation. *J. Atmos. Sci.*, **25**, 1095-1107.

Lindzen, R. S. and H.-L. Kuo, 1969: A reliable method for the numerical integration of a large class of ordinary and partial differential equations. *Mon. Wea. Rev.*, **97**, 732-734.

Lindzen, R. S., 1974: Wave-CISK in the tropics. *J. Atmos. Sci.*, **31**, 156-179.

Lindzen, R. S., 1981: Some remarks on cumulus parameterization. *Report for GISS/Climate workshop*, NASA-GISS, New York, 42-51.

Lindzen, R. S., 1981: Turbulence and stress due to gravity wave and tidal breakdown. *J. Geophys. Res.*, **86**, 9707-9714.

Lindzen, R. S., 1984: Gravity waves in the mesosphere. *Dynamics of the Middle Atmosphere*, J. R. Holton and T. Matsuno Eds., Terra Pub., 542pp.

Lindzen, R. S., 1985: Multiple gravity-wave breaking levels. *J. Atmos. Sci.*, **42**, 301-305.

Lindzen, R. S. and S. Nigam, 1987: On the role of sea surface temperature gradients in forcing low-level winds and convergence in the tropics. *J. Atmos. Sci.*, **44**, 2440-2458.

- Lindzen, R. S., 1988: Supersaturation of vertically propagating internal gravity waves. *J. Atmos. Sci.*, **45**, in press.
- Lindzen, R. S., 1988: Some remarks on cumulus parameterization. *PAGEOPH*, **126**, 123-135.
- Mahlman, J. D. and L. J. Umscheid, 1984: Successes and problems of the GFDL "SKYHI" general circulation model. *Dynamics of the Middle Atmosphere*. J. R. Holton and T. Matsuno Eds., Terra Pub., 542pp.
- Matsuno T., 1982: Q quasi-one dimensional model of the middle atmosphere circulation interacting with internal gravity waves. *J. Meteor. Soc. Japan*, **60**, 215-226.
- McFarlane, N. A., 1987: The effect of orographically excited gravity wave drag on the general circulation of the lower stratosphere and troposphere. *J. Atmos. Sci.*, **44**, 1775-1800.
- Newton, C. W., 1971: Mountain torques in the global angular momentum balance. *J. Atmos. Sci.*, **28**, 623-628.
- Norquist, D.C., E. E. Recker and R. J. Reed, 1977: The energetics of African wave disturbances as observed during phase III of GATE. *Mon. Wea. Rev.*, **105**, 334-342.
- Oort, A. H., 1983: *Global Atmospheric Circulation Statistics, 1958-1973*. NOAA professional Paper 14, 180pp.
- Ooyama K., 1971: A theory on parameterization of cumulus convection. *J. Meteor. Soc. Japan*, **49**, special issue, 744-756.

- Palmer, T. N., G. J. Shutts and R. Swinbank, 1986: Alleviation of a systematic westerly bias in general circulation and numerical weather prediction models through an orographic gravity wave drag parameterization. *Quart. J. Roy. Meteor. Soc.*, **112**, 1001-1040.
- Payne, S. W. and M. M. McGarry, 1977: The relationship of satellite inferred convective activity to easterly waves over west Africa and the adjacent ocean during phase III of GATE. *Mon. Wea. Rev.*, **105**, 414-420.
- Reed, R. J. and E. E. Recker, 1971: Structure and properties of synoptic-scale wave disturbances in the equatorial western Pacific. *J. Atmos. Sci.*, **28**, 1117-1131.
- Reed, R. J., D. C. Norquist and E. E. Recker, 1977: The structure and properties of African wave disturbances as observed during phase III of GATE. *Mon. Wea. Rev.*, **105**, 317-333.
- Riehl, H. and J. Malkus, 1958: On the heat balance in the equatorial trough zone. *Geophysica*, **6**, 505-537.
- Rosenlof, K, D. E. Stevens, J. R. Anderson and P. E. Ciesielski, 1986: The Walker circulation with observed zonal winds, a mean Hadley cell and cumulus friction. *J. Atmos. Sci.*, **43**, 449-467.
- Sarachik, E. S., 1985: A simple theory for the vertical structure of the tropical atmosphere. *PAGEOPH*, **123**, 261-271.
- Schneider, E. K. and R. S. Lindzen, 1976: A discussion of the parameterization of momentum exchange by cumulus convection. *J. Geophys. Res.*, **81**, 3158-3160.
- Schoeberl, M. R., 1985: The penetration of mountain waves into the middle atmosphere. *J. Atmos. Sci.*, **42**, 2856-2864.

- Shapiro, L. L. and D. E. Stevens, 1980: Parameterization of convective effects on the momentum budget of synoptic-scale Atlantic tropical waves. *Mon. Wea. Rev.*, **108**, 1816-1826.
- Smith A. K. and L. V. Lyjak, 1985: An observational estimate of gravity wave drag from the momentum balance in the middle atmosphere. *J. Geophys. Res.*, **90**, No. D1, 2233-2241.
- Soong, S.-T. and W.-K. Tao, 1984: A numerical study of the vertical transport of momentum in a tropical rainband. *J. Atmos. Sci.*, **41**, 1049-1061.
- Stevens, D. E., R. S. Lindzen and L. J. Shapiro, 1977: A new model of tropical waves incorporating momentum mixing by cumulus convection. *Dynamics of Atmos. and Ocean*, **1**, 365-425.
- Stevens, D. E. and R. S. Lindzen, 1978: Tropical wave-CISK with a moisture budget and cumulus friction. *J. Atmos. Sci.*, **35**, 940-961.
- Stevens, D. E., 1979: Vorticity, momentum and divergence budgets of synoptic scale wave disturbances in the tropical eastern Atlantic. *Mon. Wea. Rev.*, **107**, 535-550.
- Tanaka H. and M. D. Yamanaka, 1985: Atmospheric circulation in the lower stratosphere induced by the mesoscale mountain wave breakdown. *J. Meteor. Soc. Japan*, **63**, 1047-1054.
- Tanaka, H., 1986: A slowly varying model of the lower stratospheric zonal wind minimum induced by mesoscale mountain wave breakdown. *J. Atmos. Sci.*, **43**, 1881-1892.

Thompson, R. M., S. W. Payne, E. E. Recker and R. J. Reed, 1979: Structure and properties of the synoptic-scale wave disturbances in the intertropical convergence zone of the eastern Atlantic. *J. Atmos. Sci.*, **36**, 53-72.

Wallace, J. M., 1973: General circulation of the tropical lower stratosphere. *Rev. Geophys. and Space Phys.*, **11**, 191-222.

Xu, Q. and J. H. E. Clark, 1984: Wave CISK and mesoscale convective systems. *J. Atmos. Sci.*, **41**, 2089-2107.

Yanai, M., S. Esbensen and J.-H. Cho, 1973: Determination of bulk properties of tropical cloud clusters from large-scale heat and moisture budgets. *J. Atmos. Sci.*, **30**, 611-627.

Zipser, E. J., 1977: Mesoscale and convective-scale downdrafts as distinct components of squall-line circulation. *Mon. Wea. Rev.*, **105**, 1568-1589.

Zipser, E. J. and M. A. LeMone, 1980: Cumulonimbus vertical velocity events in GATE. Part II: Synthesis and model core structure. *J. Atmos. Sci.*, **37**, 2458-2469.

Zipser, E. J., R. J. Meitin and M. A. LeMone, 1981: Mesoscale motion fields associated with a slowly-moving GATE convective band. *J. Atmos. Sci.*, **38**, 1725-1750.



## Figure and Table Legends

**Figure 1.1:** Schematic cross section through a squall line system. Streamlines show flow relative to the squall line. Dashed streamlines show updraft circulation, thin solid streamlines show convective-scale downdraft circulation associated with the mature squall line element, and wide arrows show mesoscale downdraft below the base of the anvil cloud. Dark shading shows strong radar echo in the melting band and in the heavy precipitation zone of the mature squall line element. Light shading shows weaker radar echoes. Scalloped line indicates visible cloud boundaries. (After Houze, 1977).

**Figure 1.2:** Frequency distribution of the location of the leading edge of squall line clusters vs. easterly wave phase category for 46 squall episodes at the beginning (solid line) and termination (dashed line) of each squall episode during GATE. (After Payne and McGarry, 1977)

According to Reed et al. (1977), easterly waves were divided into eight east-west categories on the basis of the location of wave features at the reference latitude ( $11^{\circ}\text{N}$  over the continent and  $12^{\circ}\text{N}$  over the ocean). At the reference latitude, category 4 is defined as the 700-mb trough, category 8 as the 700-mb ridge and categories 2 and 6 as the maximum northerly and southerly wind components, respectively. The intermediate regions of the waves were designated by categories 1, 3, 5, and 7.

**Figure 1.3:** Squall line coordinate system. It is right-handed, with  $U$  normal to the convective line, positive in the direction of line movement. Wind speeds are relative to the earth. The schematic radar echoes are based on the Day 257 case study of Zipser et al. (1981). (After LeMone et al., 1984)

**Figure 3.1:** Distribution of the precipitation as a function of the easterly wave category during phase III of GATE. (After Thompson et al., 1979). See legend of Figure 1.2 for the definition of the wave category.

Figure 3.2: Relationship between the mesoscale monochromatic precipitation and the convergent phase of easterly waves.

Figure 3.3: Vertical distributions of (a) Mean zonal flow (in m/sec), and (b) Mean vertical p-velocity (in  $10^{-5}$  mb/sec) for the convergent phase of easterly waves observed during GATE. (After Thompson et al., 1979).

Figure 3.4: Vertical distributions of (a) Static stability parameter ( $dT/dz+g/c_p$ , in  $^{\circ}\text{C}/\text{km}$ ), and (b) Dry static energy (solid,  $s=c_p+gz$ , in kJ/kg) and moist static energy (dashed,  $h=s+Lq$ , in kJ/kg) for the convergent phase of easterly waves observed during GATE. (After Thompson et al., 1979 and Augstein et al., 1974).

Figure 3.5: Same as Figure 3.3 but for the Marshall Islands tests. (After Reed and Recker, 1971).

Figure 3.6: Same as Figure 3.4 but for the Marshall Islands tests. (After Reed and Recker, 1971).

Figure 3.7: Vertical distributions of (a) cloud mass flux (in mb/sec), and (b) cumulus heating (in  $^{\circ}\text{C}/\text{day}$ ) obtained from the cumulus parameterization scheme described in text for GATE. Magnitudes of (a) and (b) are normalized according to precipitation rate = 4.8 cm/day.

Figure 3.8: Same as Figure 3.7 but for the Marshall Islands tests.

Figure 4.1: Results using the monochromatic precipitation for Marshall Islands profiles, with phase speed = -10 m/s, wavelength = 200 km, and mean and perturbation precipitation = 4.8 cm/day. Cumulus friction and  $\bar{w}$  are included.

(a) Amplitude (solid, scale shown at the bottom) and phase (short dashed, scale shown at the top) for the vertical structure of T (in °C).

(b) Same as (a), but for u (in m/s).

(c) Same as (a), but for w (in cm/sec), plus the direct response of w (long dashed) to cumulus heating (see text).

(d) Different components of momentum fluxes (in Pa) averaged over one wavelength (200 km), including that due to gravity waves ( $\overline{\rho u' w'}$ , solid), perturbation cloud transport ( $-\overline{M'_c(u' - u'_c)}$ , short dashed), mean cloud transport ( $-\overline{M_c(\bar{u} - \bar{u}_c)}$ , long dashed) and the sum of all three components (medium dashed).

Figure 4.2: Same as Figure 4.1, but without cumulus friction and  $\bar{w}$ . Thus in (d) only a solid line is drawn.

Figure 4.3: Same as Figure 4.1, except that GATE profiles are used with phase speed = -11 m/s.

Figure 4.4: Same as Figure 4.3, but without cumulus friction and  $\bar{w}$ . Thus in (d) only a solid line is drawn.

Figure 4.5: Results using the Gaussian precipitation for Marshall Islands profiles, with phase speed = -13 m/s, hypothetical domain = 200 km,  $P_0 = 60$  cm/day and  $x_0 = 10$  km. Cumulus friction and  $\bar{w}$  are included.

(a) Full solution of T (in °C) on an x-z plane. The contour interval is 0.5 °C.

Figure 4.5(b): Same as Figure 4.5(a), but for u (in m/s). The contour interval is 1 m/s.

Figure 4.5(c): Same as Figure 4.5(a), but for w (in cm/sec). The contour interval is 20 cm/s.

Figure 4.5(d): Streamline pattern relative to the the squall line.

Figure 4.6(a): Same as Figure 4.5(a), but without cumulus friction and  $\bar{w}$ . The contour interval is 0.5 °C.

Figure 4.6(b): Same as Figure 4.6(a), but for u (in m/s). The contour interval is 1 m/s.

Figure 4.6(c): Same as Figure 4.6(a), but for w (in cm/sec). The contour interval is 20 cm/s.

Figure 4.6(d): Streamline pattern relative to the the squall line.

Figure 4.7(a): Same as Figure 4.5(a), except that GATE profiles are used with phase speed = -11 m/s. The contour interval is 1.0 °C.

Figure 4.7(b): Same as Figure 4.7(a), but for u (in m/s). The contour interval is 3 m/s.

Figure 4.7(c): Same as Figure 4.7(a), but for w (in cm/sec). The contour interval is 20 cm/s.

Figure 4.7(d): Streamline pattern relative to the the squall line.

Figure 4.8(a): Same as Figure 4.7(a), but without cumulus friction and  $\bar{w}$ . The contour interval is 0.5 °C.

Figure 4.8(b): Same as Figure 4.7(a), but for u (in m/s). The contour interval is 1 m/s.

Figure 4.8(c): Same as Figure 4.7(a), but for w (in cm/sec). The contour interval is 20 cm/s.

Figure 4.8(d): Streamline pattern relative to the the squall line.

Figure 4.9: Mean zonal wind profiles (with annual cycle removed) representing different phases of the quasi-biennial oscillation used for calculate the second breaking levels of the gravity wave generated by cumulus convection. (After Wallace, 1973).

Figure A.1: Responses ( $w$ ) at the top of the domain for different vertical scales ( $L_z$ ) of the gravity wave. The domain of calculation is (0, 60 km). The thermal forcing is  $= \sin(\pi(z-2\text{km})/10\text{km})$  for  $z \in (2, 12 \text{ km})$ , and vanishes otherwise. The abscissa shows the ratio of  $L_z/10 \text{ km}$ . The ordinate shows responses relative to the case when  $L_z/10 \text{ km} = 0.1$  where the amplitude of the response is set arbitrarily to one. Radiation boundary condition is applied at the top, and no-slip boundary condition is applied at the bottom. Note that the wavelength of the gravity wave is defined as  $2\pi L_z$ .

Figure A.2: Same as Figure A.1, except that radiation condition is also applied at the bottom.

Figure A.3: Same as Figure A.1, except that the thermal forcing is  $= \exp(-((z-7\text{km})/4\text{km})^2)$ , and the abscissa shows the ratio of  $L_z/4 \text{ km}$ .

Figure A.4: Same as Figure A.3, except that radiation condition is applied at the bottom.

Figure A.5: Same as Figure A.3, except that the thermal forcing is  $= \exp(-((z-30\text{km})/10\text{km})^2)$ , and the abscissa shows the ratio of  $L_z/10 \text{ km}$

Figure A.6: Same as Figure A.5, except that radiation condition is applied at the bottom.

Table 4.1 Composites of results (both viscous and inviscid) in the interior of the troposphere for the monochromatic precipitation with  $\bar{P} = P' = 4.8$  cm/day and wavelength = 200 km.

Table 4.2 Same as Table 4.1 but for the lower stratosphere. See text for the definition of  $(\rho w)_{\text{global}}$ .

Table 4.3  $w$  (cm/sec, enclosed by double-solid lines) at 16 km using different values of  $\Gamma$  (static stability, in °C) in the stratosphere, no cumulus friction is considered. Phase speeds of -11 and -12 m/s and profiles for both GATE and Marshall are considered here.

Table 4.4 Same as Table 4.3, but with cumulus friction.

Table 4.5 Composites of results (both viscous and inviscid) in the interior of the troposphere for the localized precipitation with  $P_0 = 60$  cm/day,  $x_0 = 10$  km, and the hypothetical domain = 200 km.

Table 4.6 Same as Table 4.5 but for the lower stratosphere. Note that the statistics shown here have not taken into account the possible wave breaking below the cloud top. See text for the definition of  $(\rho w)_{\text{global}}$ .

Table 4.7  $(\rho w)_{\text{global}}$  (in  $10^4$  Pa) for different values of the hypothetical domain ( $M$ ). Two values of  $M$  (200 and 400 km), two profiles (GATE and Marshall Islands), together with  $c = -11$  m/s are used for the calculations. Cumulus friction is included.

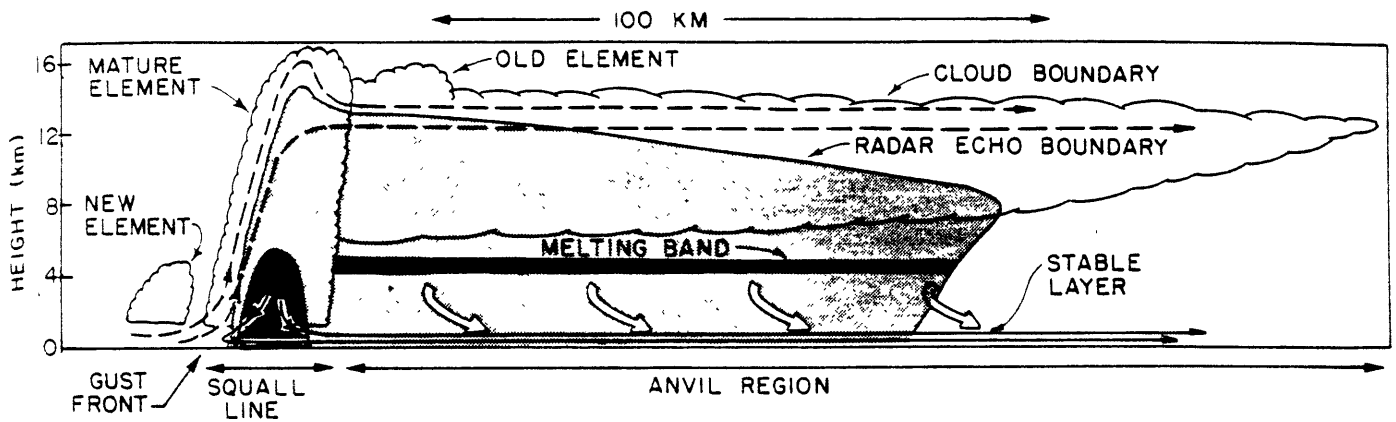


Figure 1.1: Schematic cross section through a squall line system. Streamlines show flow relative to the squall line. Dashed streamlines show updraft circulation, thin solid streamlines show convective-scale downdraft circulation associated with the mature squall line element, and wide arrows show mesoscale downdraft below the base of the anvil cloud. Dark shading shows strong radar echo in the melting band and in the heavy precipitation zone of the mature squall line element. Light shading shows weaker radar echoes. Scalloped line indicates visible cloud boundaries. (After Houze, 1977).

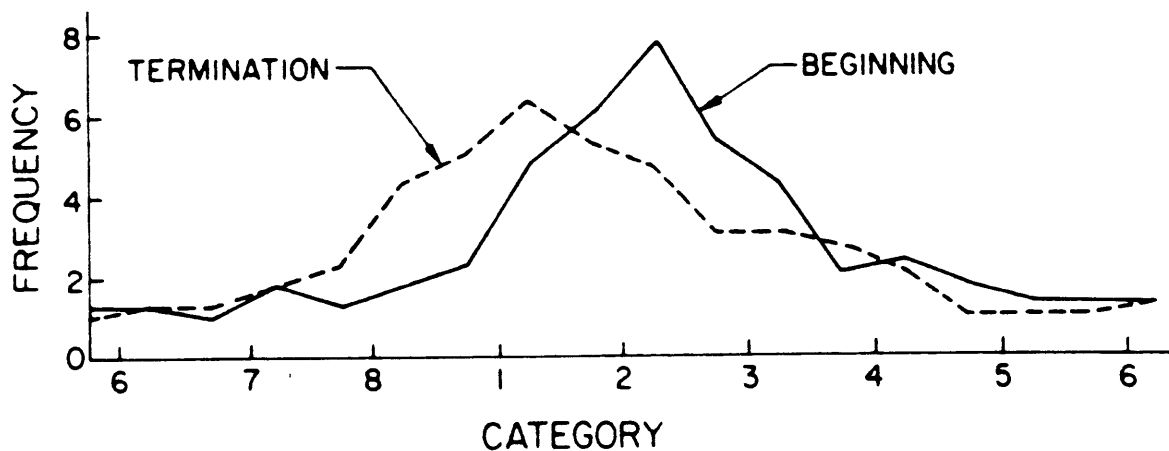


Figure 1.2: Frequency distribution of the location of the leading edge of squall line clusters vs. easterly wave phase category for 46 squall episodes at the beginning (solid line) and termination (dashed line) of each squall episode during GATE. (After Payne and McGarry, 1977)

According to Reed et al. (1977), easterly waves were divided into eight east-west categories on the basis of the location of wave features at the reference latitude ( $11^{\circ}\text{N}$  over the continent and  $12^{\circ}\text{N}$  over the ocean). At the reference latitude, category 4 is defined as the 700-mb trough, category 8 as the 700-mb ridge and categories 2 and 6 as the maximum northerly and southerly wind components, respectively. The intermediate regions of the waves were designated by categories 1, 3, 5, and 7.



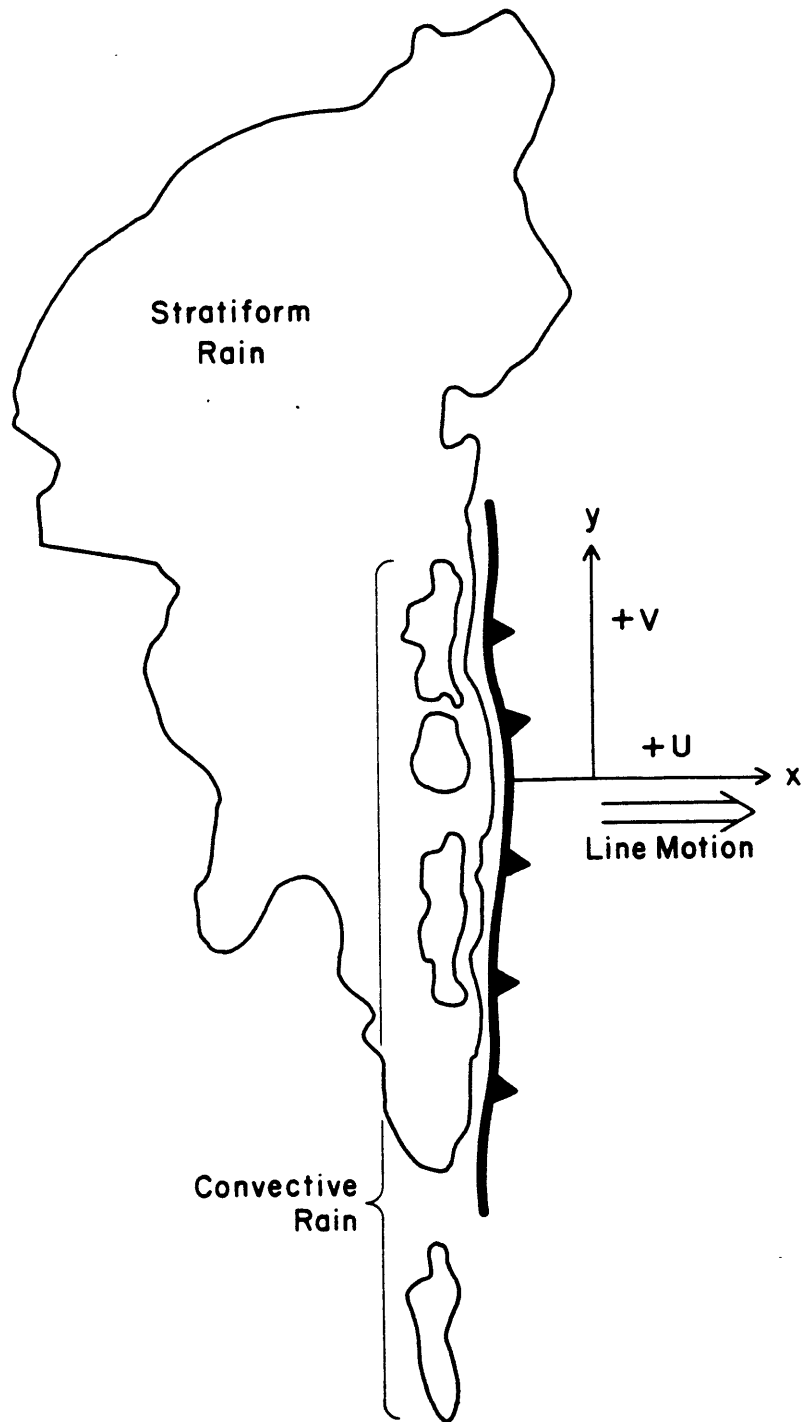


Figure 1.3: Squall line coordinate system. It is right-handed, with  $U$  normal to the convective line, positive in the direction of line movement. Wind speeds are relative to the earth. The schematic radar echoes are based on the Day 257 case study of Zipser et al. (1981). (After LeMone et al., 1984)

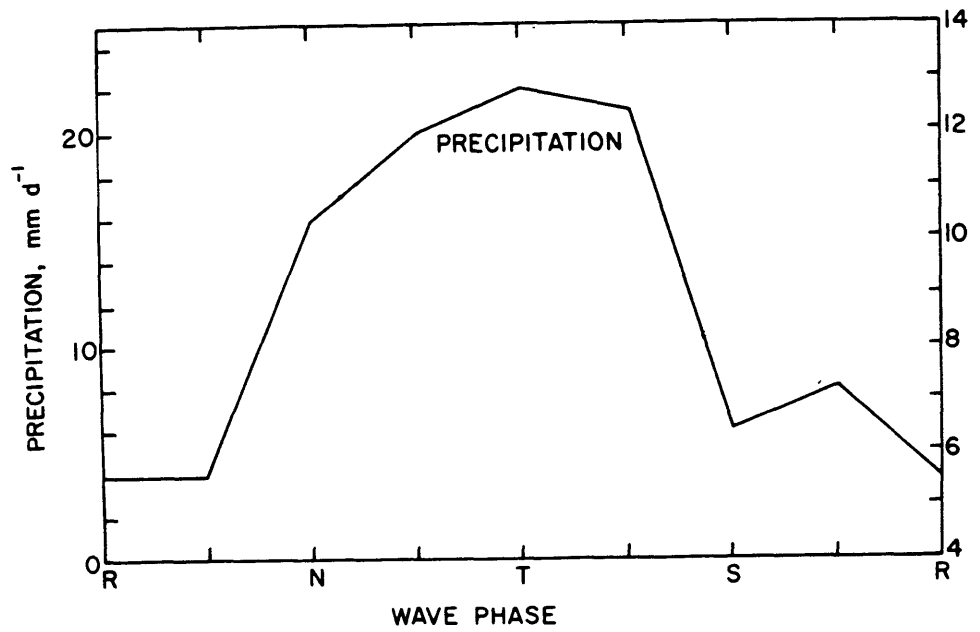


Figure 3.1: Distribution of the precipitation as a function of the easterly wave category during phase III of GATE. (After Thompson et al., 1979). See legend of Figure 1.2 for the definition of the wave category.

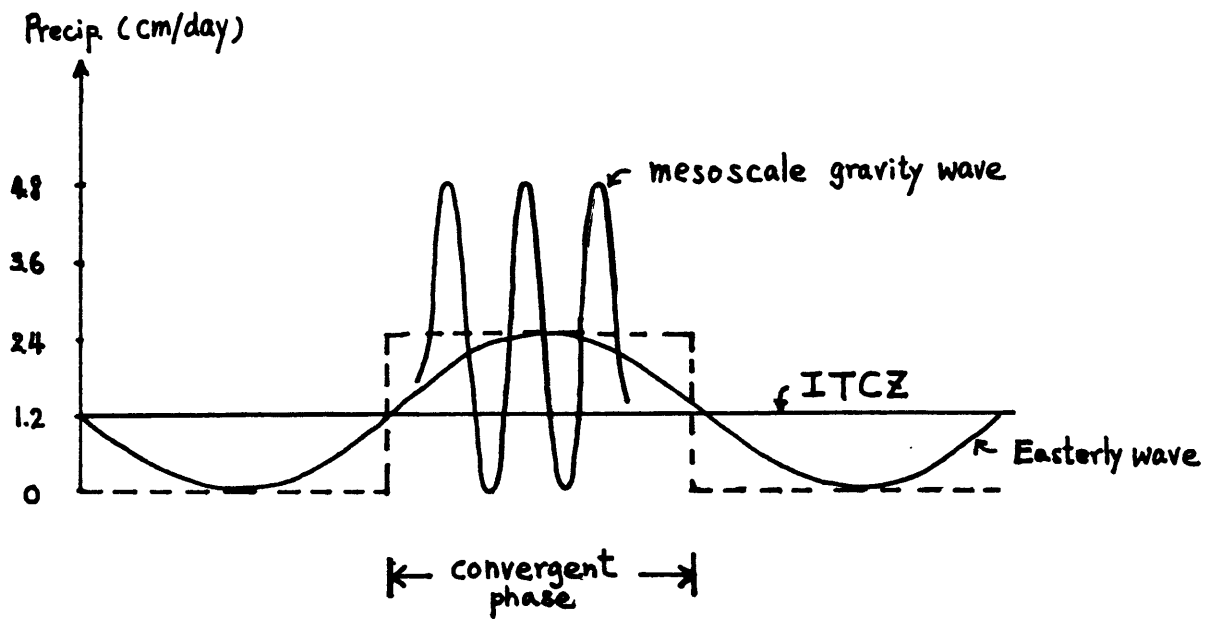


Figure 3.2: Relationship between the mesoscale monochromatic precipitation and the convergent phase of easterly waves.

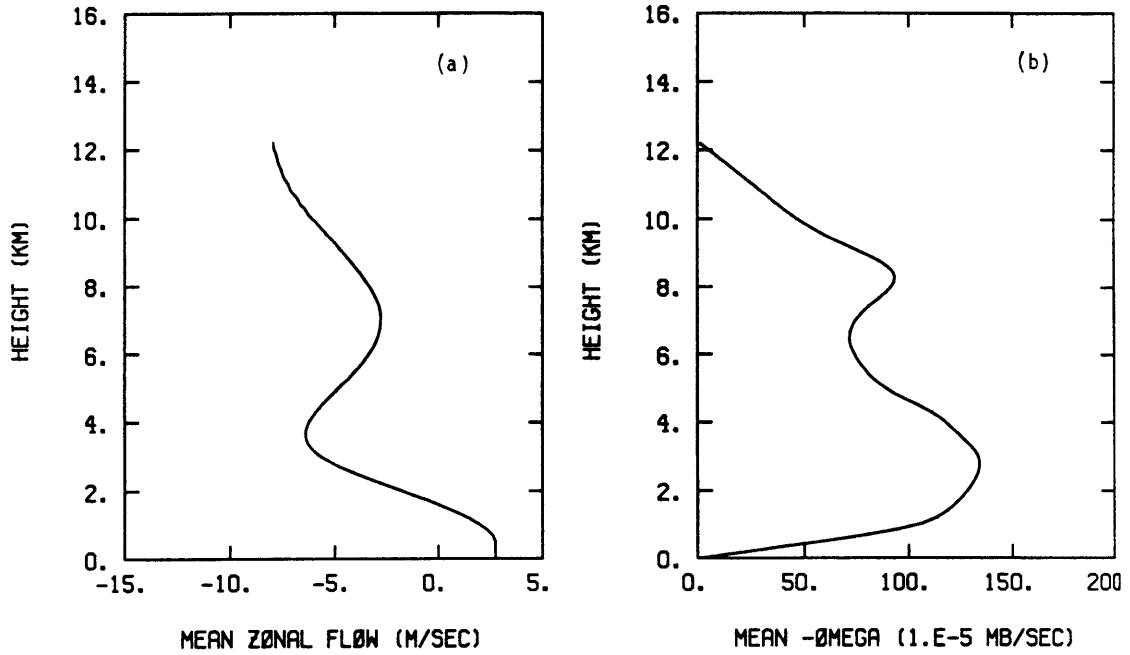


Figure 3.3: Vertical distributions of (a) Mean zonal flow (in m/sec), and (b) Mean vertical p-velocity (in  $10^{-5}$  mb/sec) for the convergent phase of easterly waves observed during GATE. (After Thompson et al., 1979).

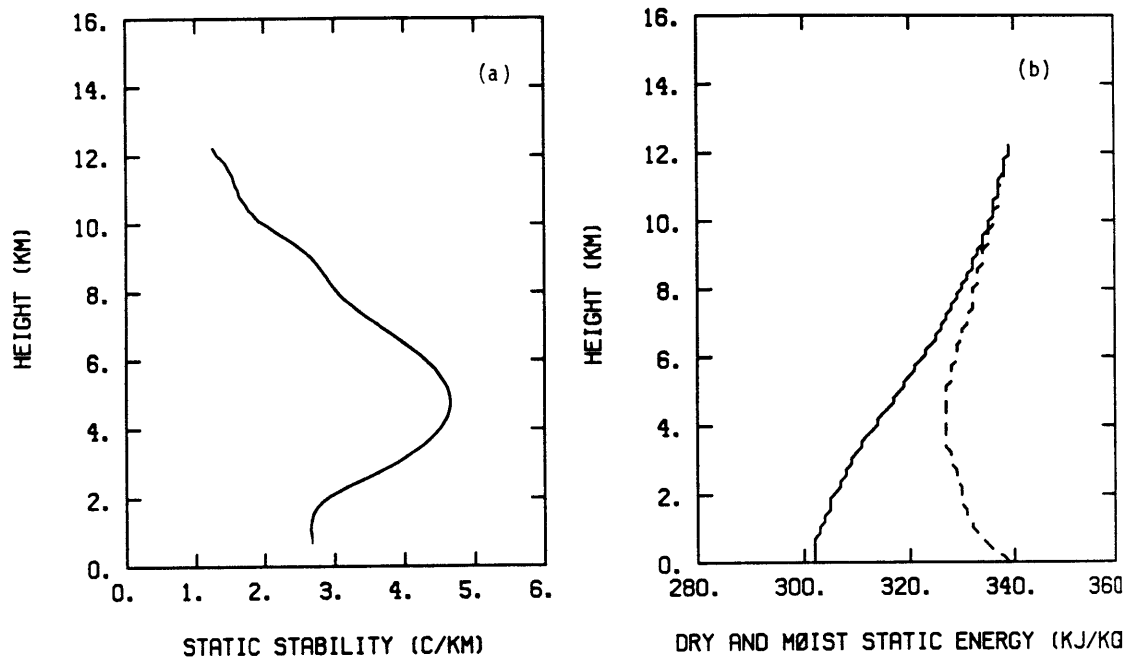


Figure 3.4: Vertical distributions of (a) Static stability parameter ( $dT/dz+g/c_p$ , in  $^{\circ}\text{C}/\text{km}$ ), and (b) Dry static energy (solid,  $s=c_p+gz$ , in  $\text{kJ}/\text{kg}$ ) and moist static energy (dashed,  $h=s+Lq$ , in  $\text{kJ}/\text{kg}$ ) for the convergent phase of easterly waves observed during GATE. (After Thompson et al., 1979 and Augstein et al., 1974).

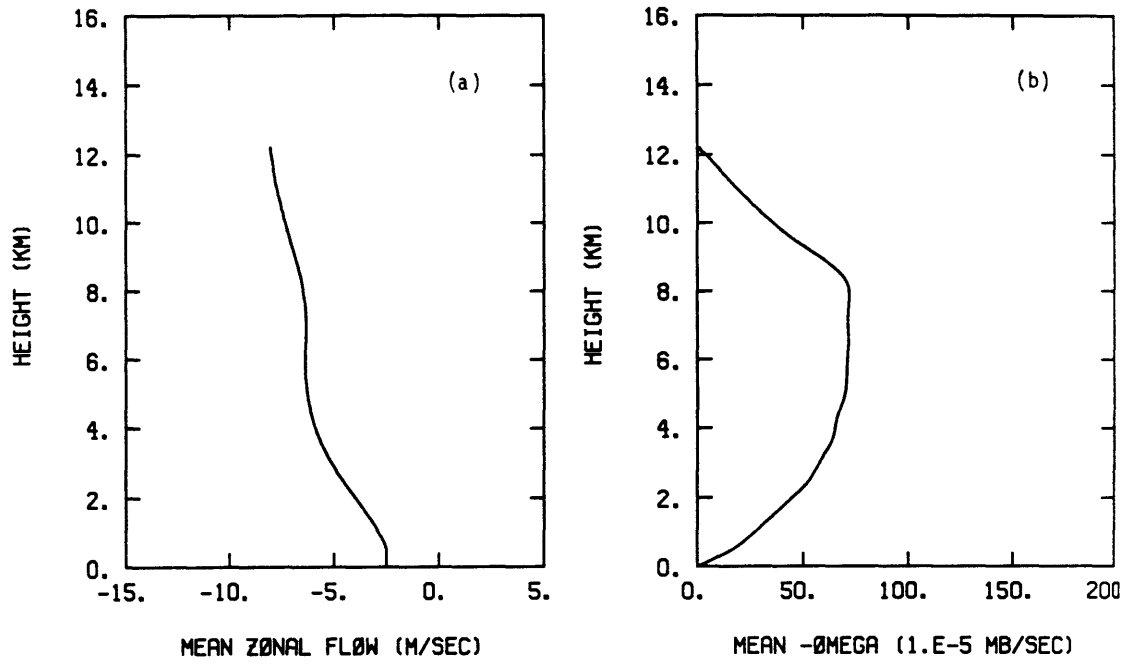


Figure 3.5: Same as Figure 3.3 but for the Marshall Islands tests. (After Reed and Recker, 1971).

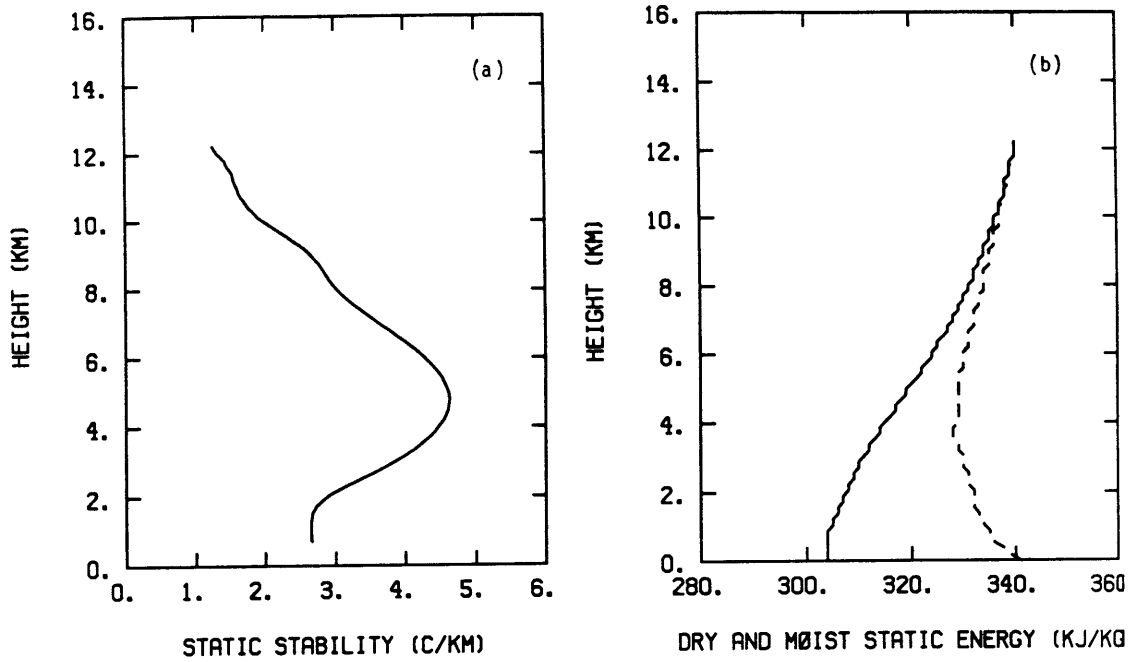


Figure 3.6: Same as Figure 3.4 but for the Marshall Islands tests. (After Reed and Recker, 1971).

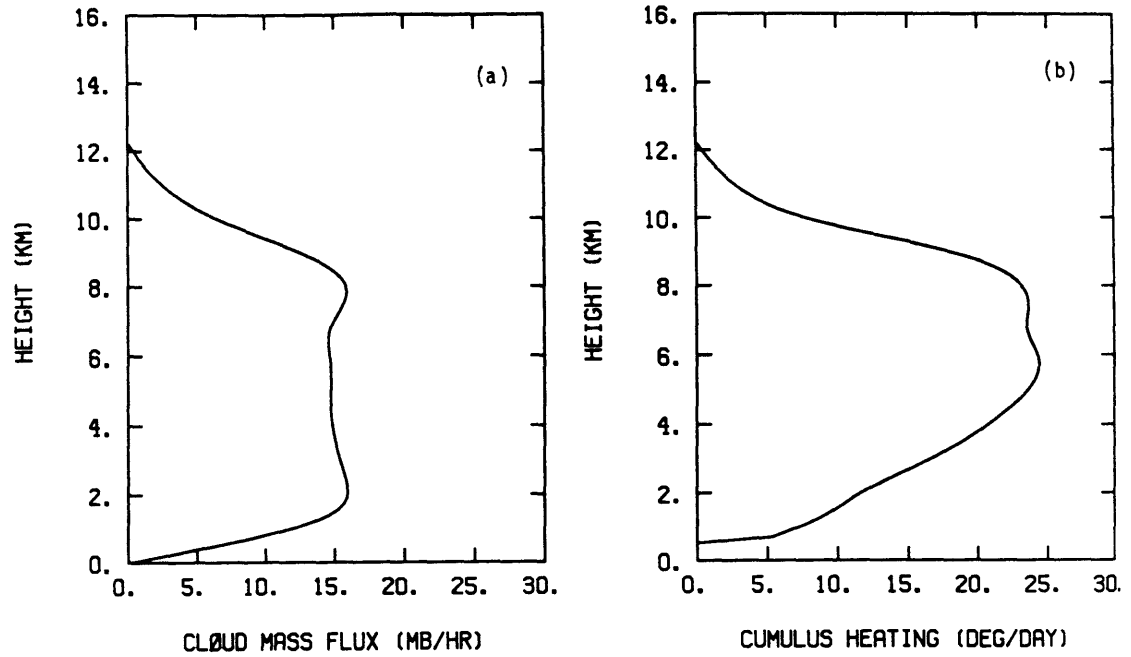


Figure 3.7: Vertical distributions of (a) cloud mass flux (in mb/sec), and (b) cumulus heating (in °C/day) obtained from the cumulus parameterization scheme described in text for GATE. Magnitudes of (a) and (b) are normalized according to precipitation rate = 4.8 cm/day.



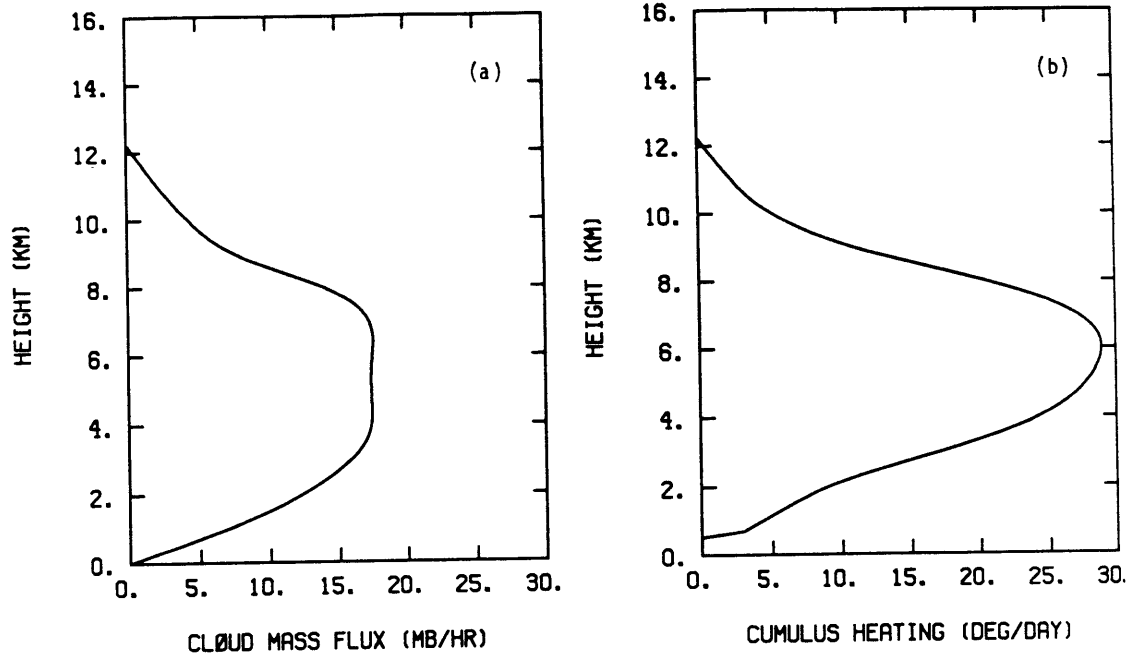


Figure 3.8: Same as Figure 3.7 but for the Marshall Islands tests.

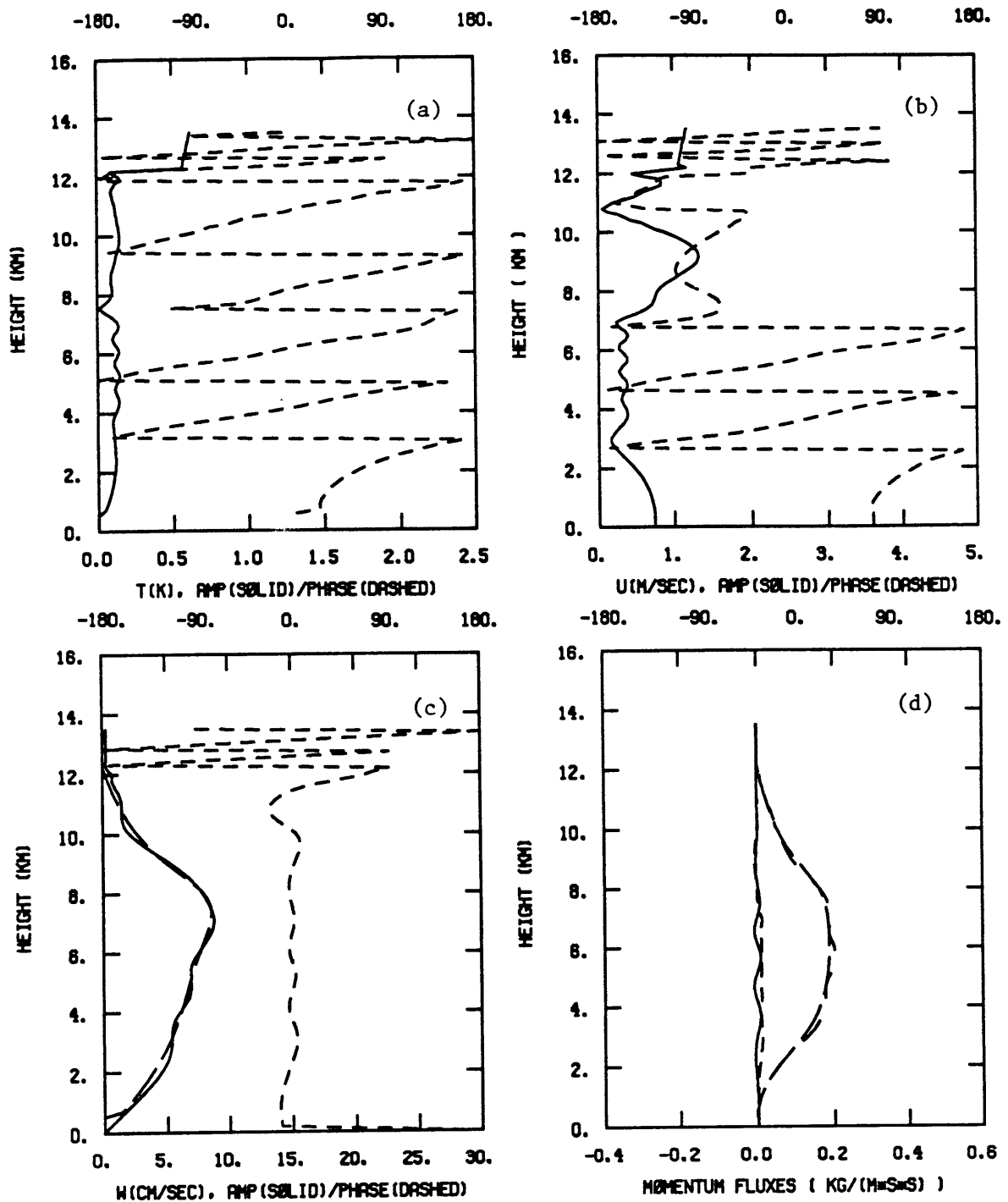


Figure 4.1: Results using the monochromatic precipitation for Marshall Islands profiles, with phase speed = -10 m/s, wavelength = 200 km, and mean and perturbation precipitation = 4.8 cm/day. Cumulus friction and  $\bar{w}$  are included. (a) Amplitude (solid, scale shown at the bottom) and phase (short dashed, scale shown at the top) for the vertical structure of T (in °C). (b) Same as (a), but for u (in m/s). (c) Same as (a), but for w (in cm/sec), plus the direct response of w (long dashed) to cumulus heating (see text). (d) Different components of momentum fluxes (in Pa) averaged over one wavelength (200 km), including that due to gravity waves ( $\overline{\rho u' w'}$ , solid), perturbation cloud transport ( $-\overline{M'_c(u' - u'_c)}$ , short dashed), mean cloud transport ( $-\overline{M_c(\bar{u} - \bar{u}_c)}$ , long dashed) and the sum of all three components (medium dashed).

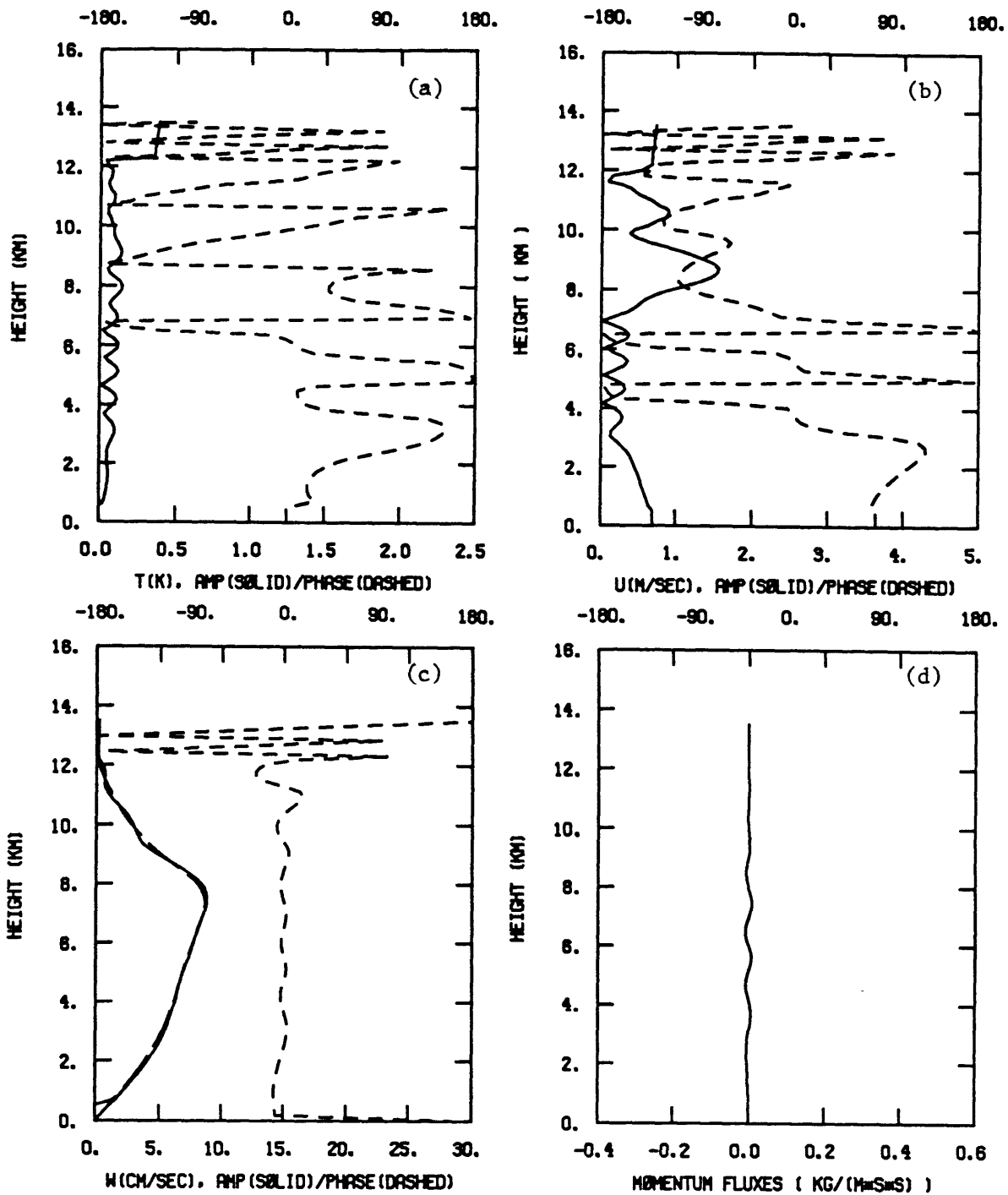


Figure 4.2: Same as Figure 4.1, but without cumulus friction and  $\bar{w}$ . Thus in (d) only a solid line is drawn.

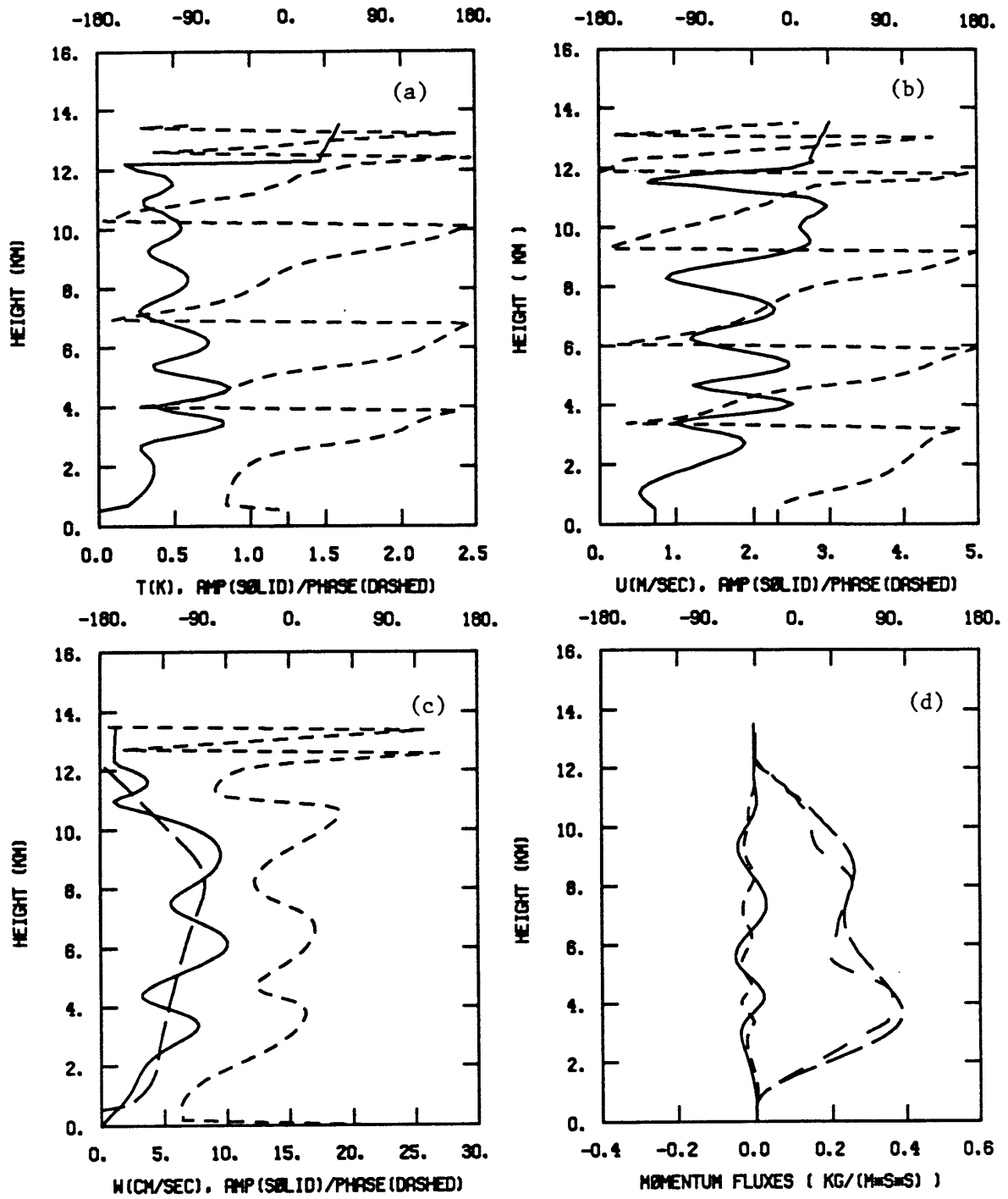


Figure 4.3: Same as Figure 4.1, except that GATE profiles are used with phase speed = -11 m/s.

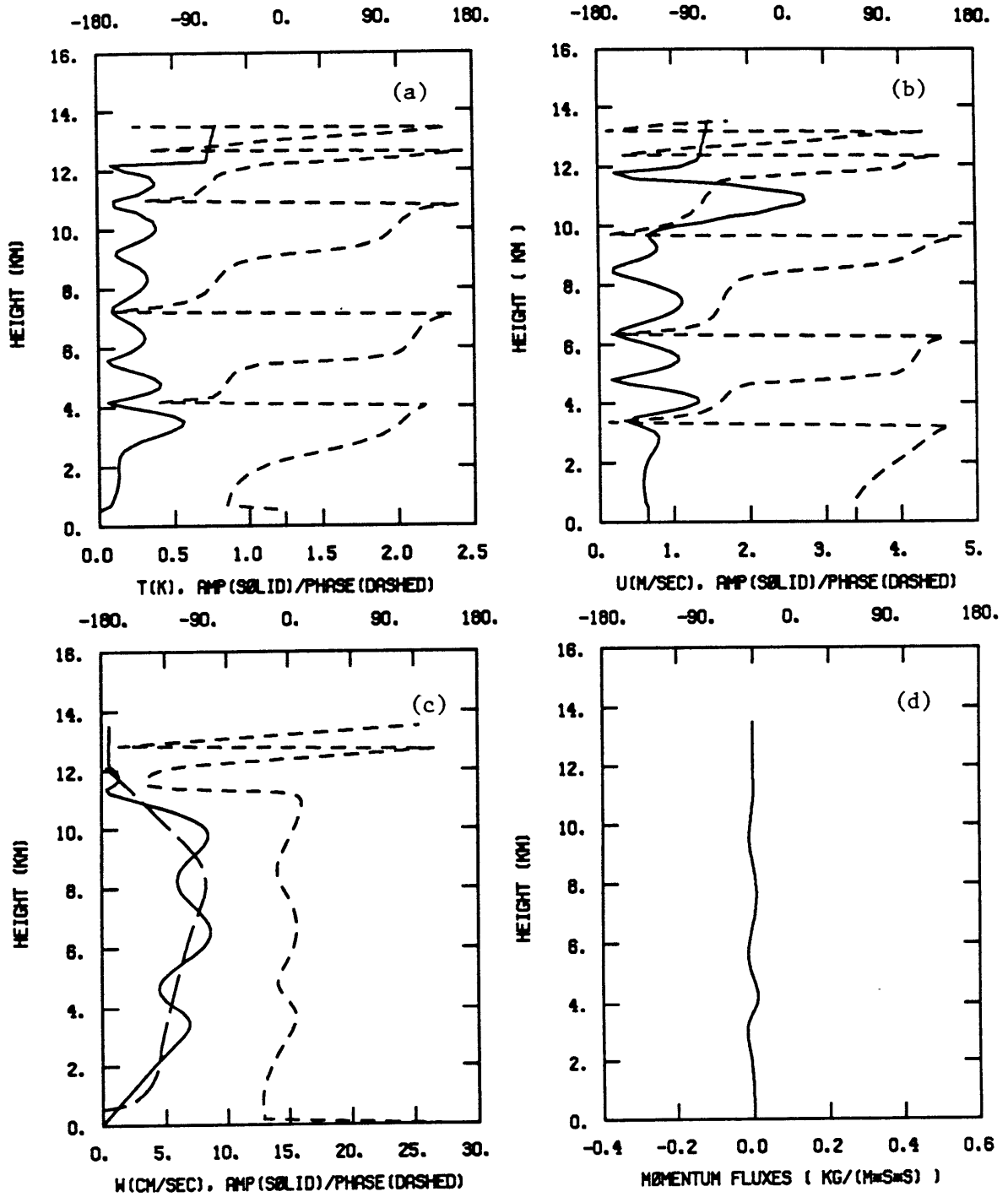


Figure 4.4: Same as Figure 4.3, but without cumulus friction and  $\bar{w}$ . Thus in (d) only a solid line is drawn.

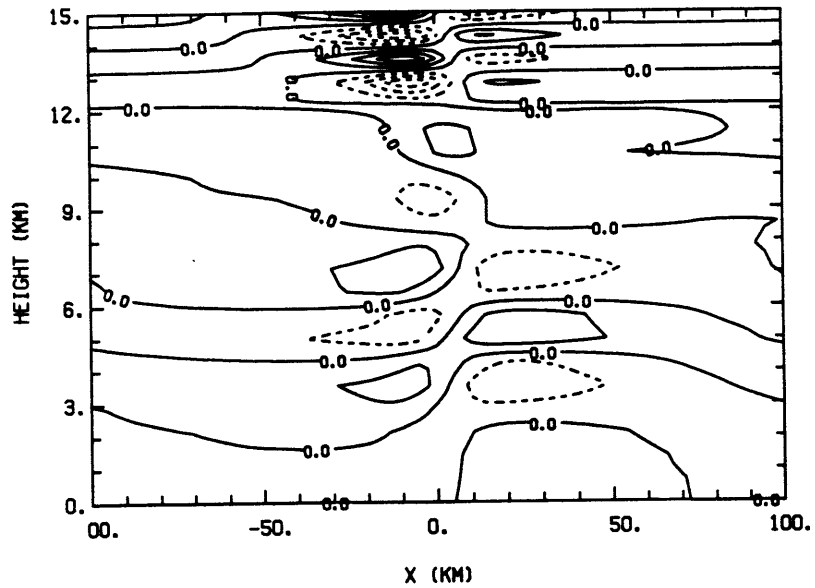


Figure 4.5: Results using the Gaussian precipitation for Marshall Islands profiles, with phase speed = -13 m/s, hypothetical domain = 200 km,  $P_0 = 60$  cm/day and  $x_0 = 10$  km. Cumulus friction and  $\bar{w}$  are included.  
 (a) Full solution of  $T$  (in  $^{\circ}\text{C}$ ) on an  $x$ - $z$  plane. The contour interval is  $0.5$   $^{\circ}\text{C}$ .

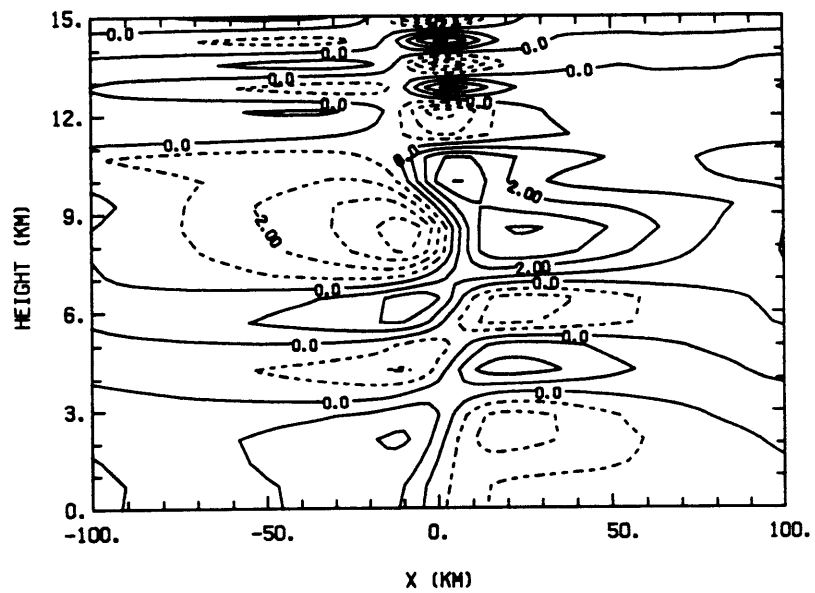


Figure 4.5(b): Same as Figure 4.5(a), but for  $u$  (in m/s). The contour interval is 1 m/s.

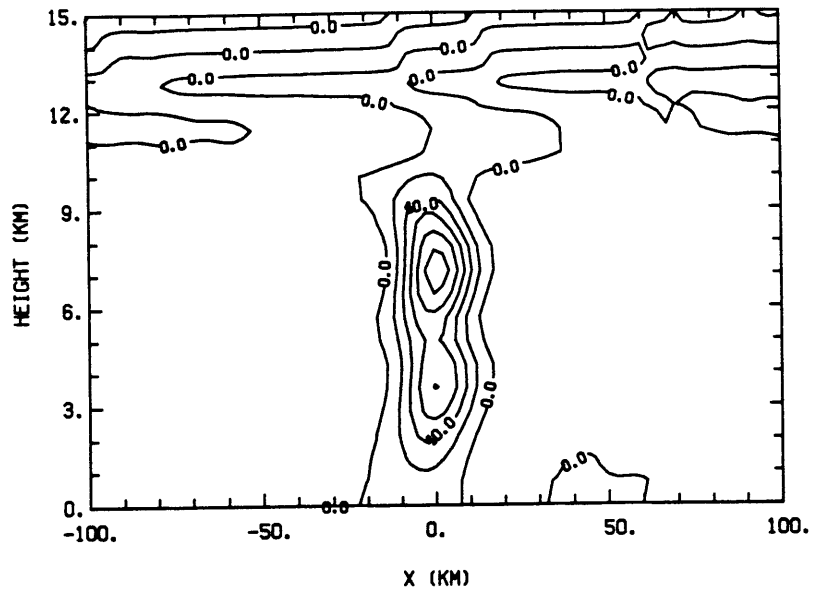


Figure 4.5(c): Same as Figure 4.5(a), but for  $w$  (in cm/sec). The contour interval is 20 cm/s.

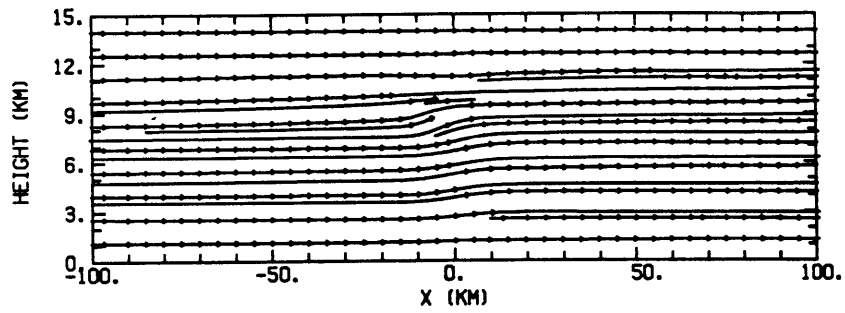


Figure 4.5(d): Streamline pattern relative to the the squall line.

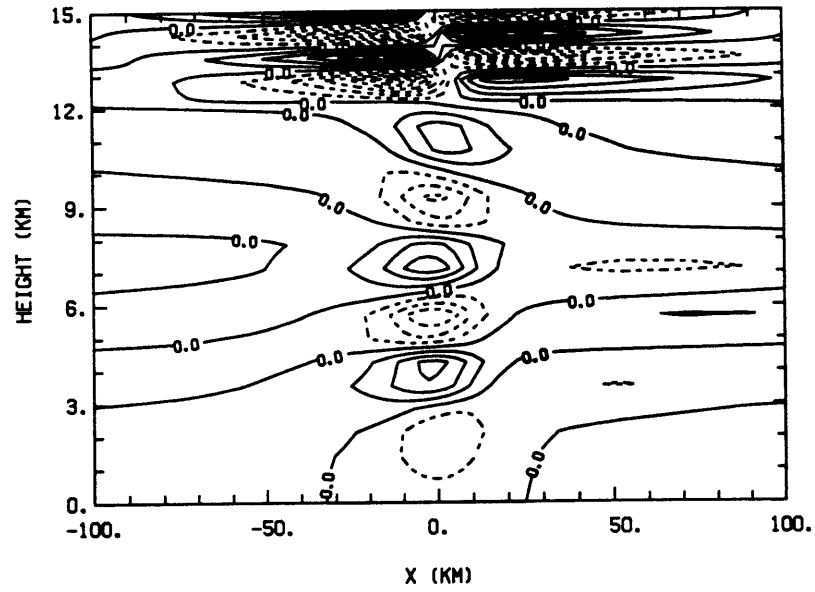


Figure 4.6(a): Same as Figure 4.5(a), but without cumulus friction and  $\bar{w}$ . The contour interval is 0.5 °C.

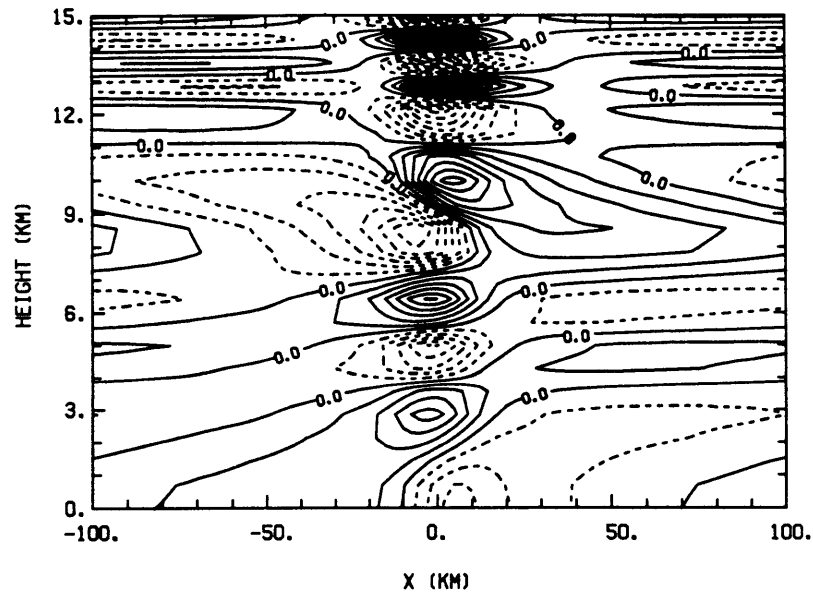


Figure 4.6(b): Same as Figure 4.6(a), but for  $u$  (in m/s). The contour interval is 1 m/s.



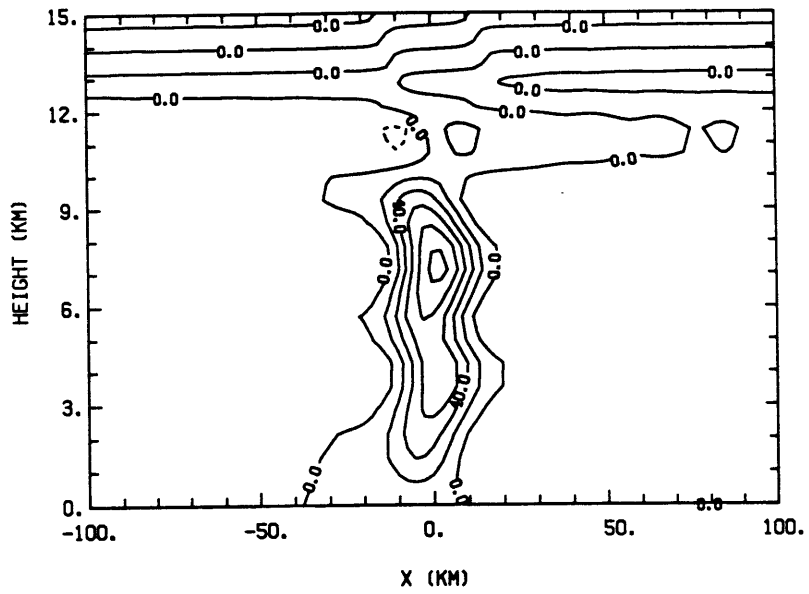


Figure 4.6(c): Same as Figure 4.6(a), but for  $w$  (in cm/sec). The contour interval is 20 cm/s.

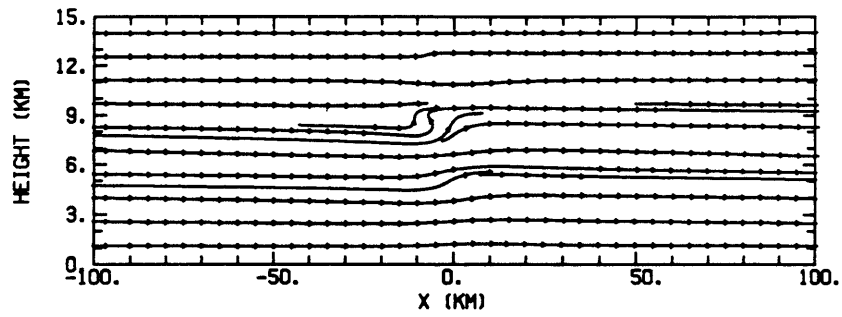


Figure 4.6(d): Streamline pattern relative to the the squall line.

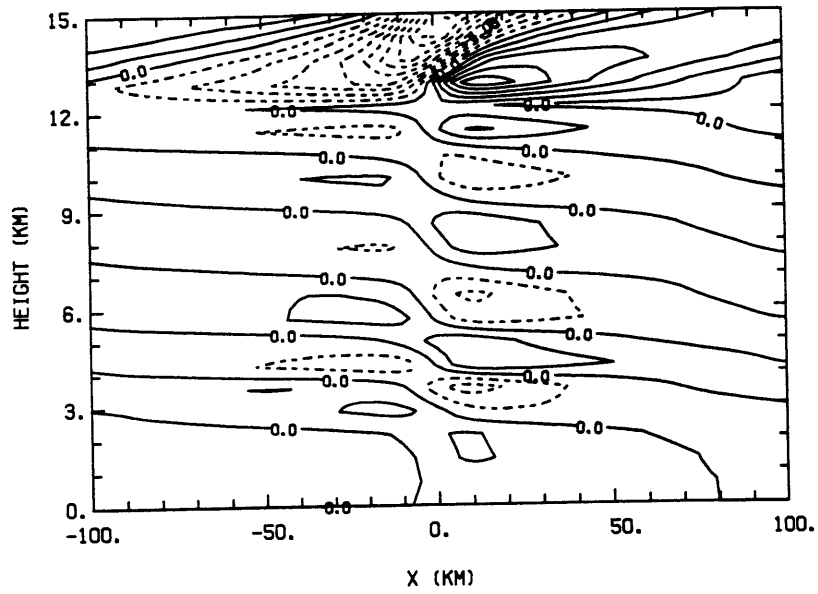


Figure 4.7(a): Same as Figure 4.5(a), except that GATE profiles are used with phase speed = -11 m/s. The contour interval is 1.0 °C.

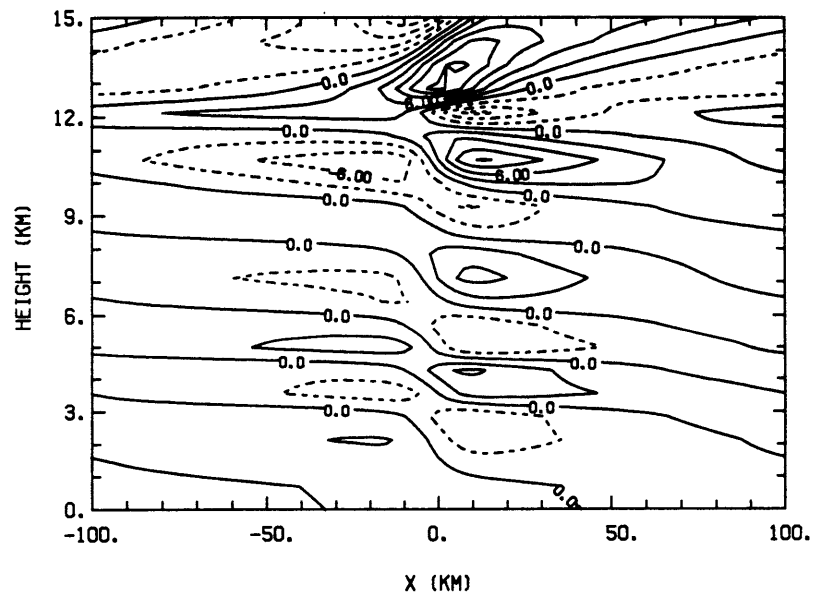


Figure 4.7(b): Same as Figure 4.7(a), but for  $u$  (in m/s). The contour interval is 3 m/s.

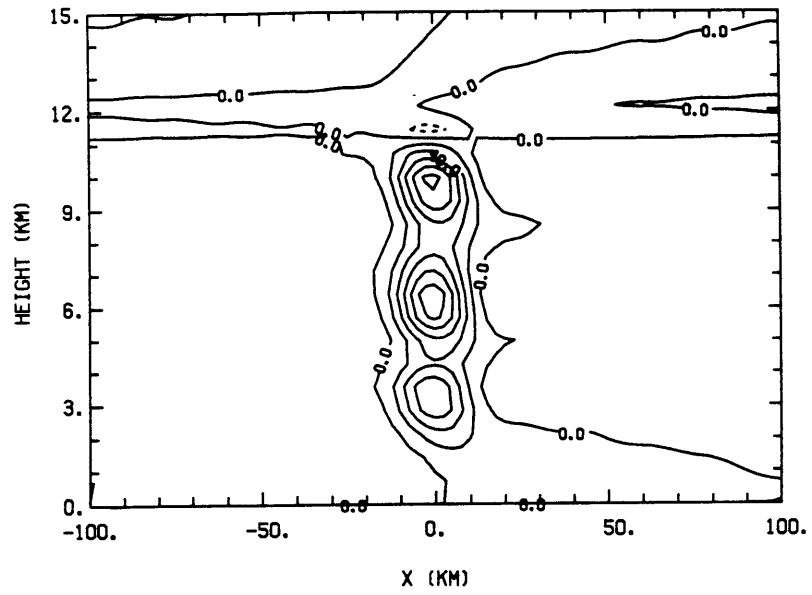


Figure 4.7(c): Same as Figure 4.7(a), but for  $w$  (in cm/sec). The contour interval is 20 cm/s.

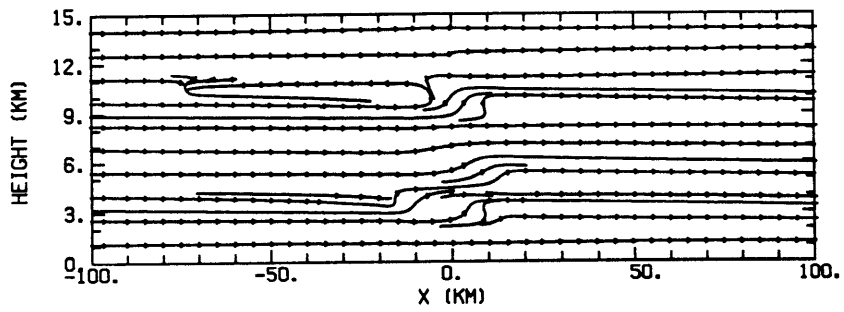


Figure 4.7(d): Streamline pattern relative to the the squall line.

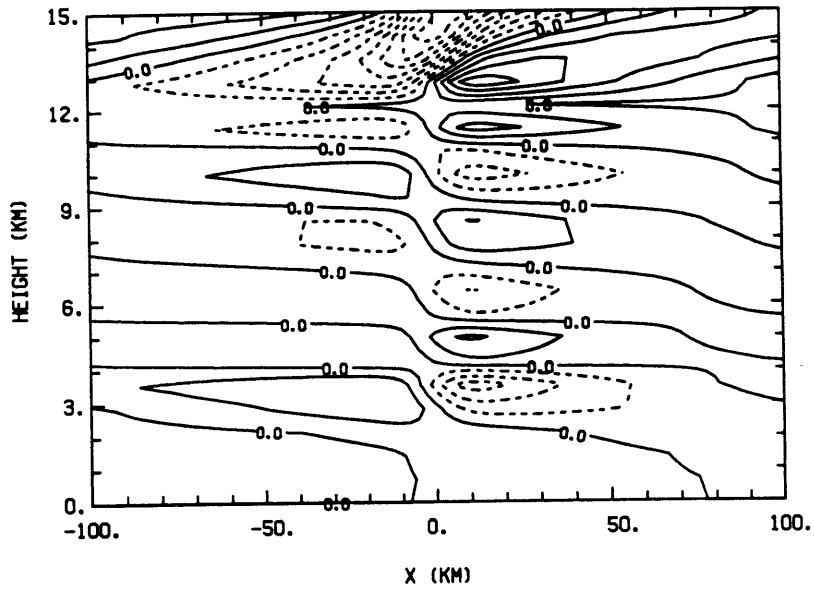


Figure 4.8(a): Same as Figure 4.7(a), but without cumulus friction and  $\bar{w}$ . The contour interval is 0.5 °C.

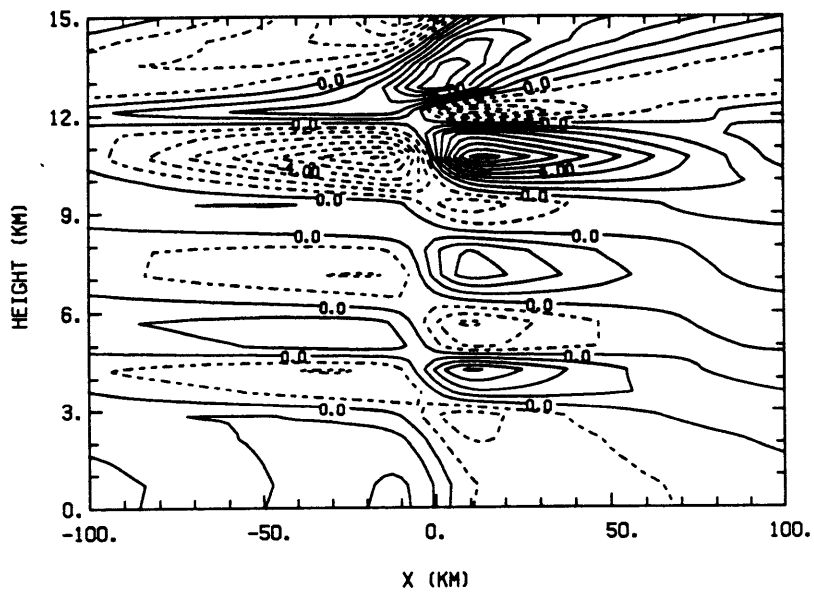


Figure 4.8(b): Same as Figure 4.7(a), but for  $u$  (in m/s). The contour interval is 1 m/s.

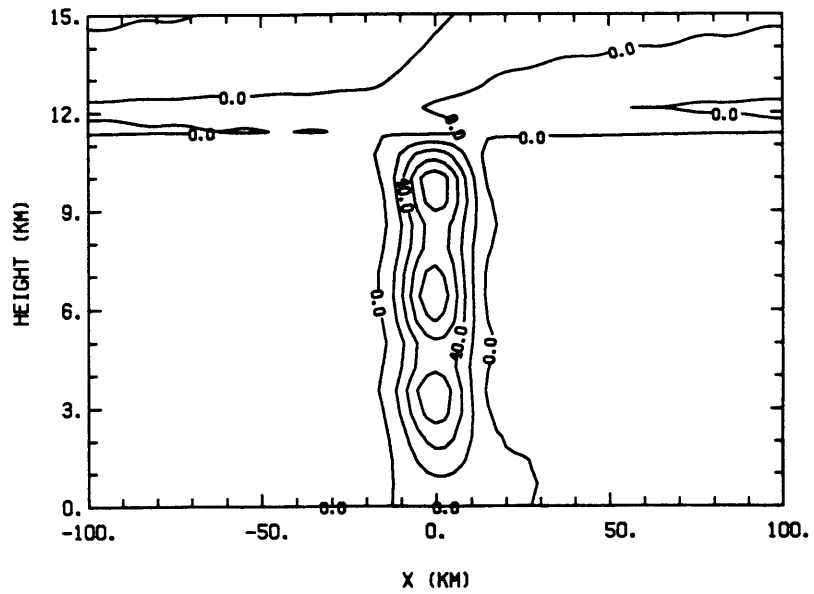


Figure 4.8(c): Same as Figure 4.7(a), but for  $w$  (in cm/sec). The contour interval is 20 cm/s.

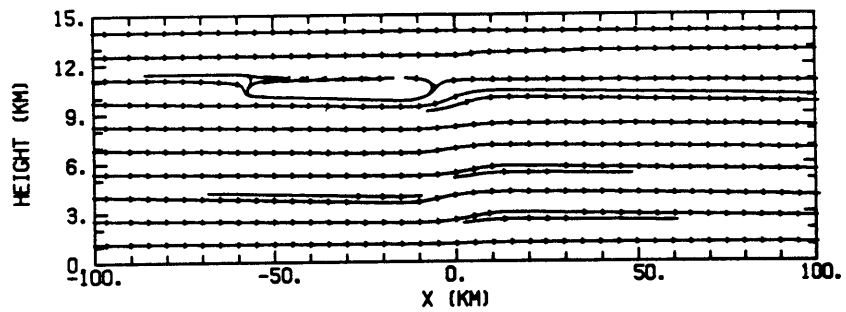


Figure 4.8(d): Streamline pattern relative to the the squall line.

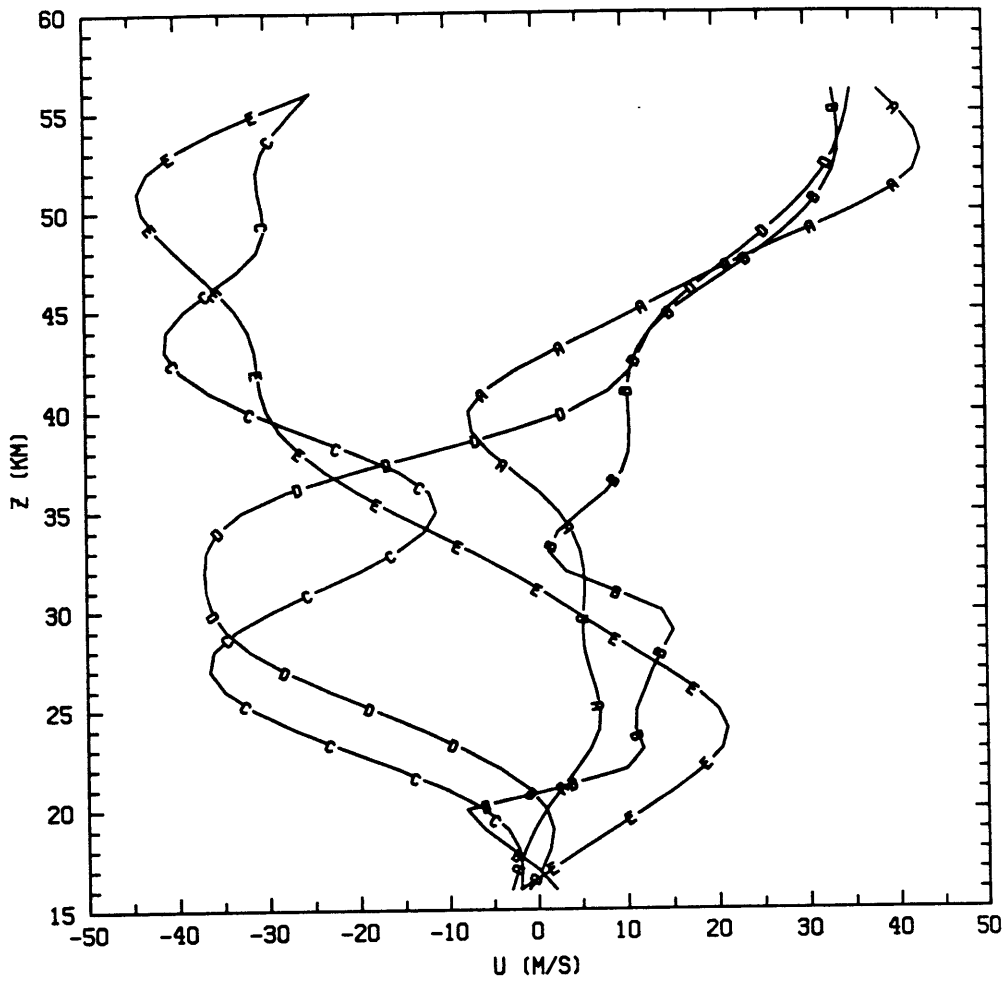


Figure 4.9: Mean zonal wind profiles (with annual cycle removed) representing different phases of the quasi-biennial oscillation used for calculate the second breaking levels of the gravity wave generated by cumulus convection. (After Wallace, 1973).

	Average		Range	
	Viscous	Inviscid	Viscous	Inviscid
u (m/s)	1.22	1.21	0.8 to 2.0	0.7 to 3.0
w (cm/s)	9.00	9.00	omitted	omitted
T (°C)	0.40	0.41	0.2 to 0.8	0.2 to 1.0

Table 4.1 Composites of results (both viscous and inviscid) in the interior of the troposphere for the monochromatic precipitation with  $\bar{P} = P' = 4.8$  cm/day and wavelength = 200 km.

	Average		Range	
	Viscous	Inviscid	Viscous	Inviscid
u (m/s)	1.38	1.38	0.2 to 2.9	0.3 to 3.1
w (cm/s)	0.96	0.99	0.1 to 1.5	0.1 to 2.6
T (°C)	0.77	0.73	0.2 to 2.2	0.1 to 1.8
$(\rho w)_{\text{global}} (10^4 \text{ Pa})$	-1.25	-1.40	-0.01 to -4.4	-0.006 to -6.9

Table 4.2 Same as Table 4.1 but for the lower stratosphere. See text for the definition of  $(\rho w)_{\text{global}}$ .

Region	phase speed	$\Gamma=80$	$\Gamma=30$
GATE	-11	1.30	1.80
	-12	0.18	0.25
Marshall	-11	0.38	0.54
Islands	-12	0.84	1.01

Table 4.3  $w$  (cm/sec, enclosed by double-solid lines) at 16 km using different values of  $\Gamma$  (static stability, in  $^{\circ}\text{C}$ ) in the stratosphere, no cumulus friction is considered. Phase speeds of -11 and -12 m/s and profiles for both GATE and Marshall are considered here.

Region	phase speed	$\Gamma=80$	$\Gamma=30$
GATE	-11	1.78	2.68
	-12	0.83	1.12
Marshall	-11	0.68	0.89
Islands	-12	0.71	0.83

Table 4.4 Same as Table 4.3, but with cumulus friction.



	Average		Range	
	Viscous	Inviscid	Viscous	Inviscid
u (m/s)	4.22	4.08	2. to 10.	1. to 6.
w (cm/s)	108	109	omitted	omitted
T (°C)	1.07	1.15	0.3 to 2.	0.3 to 2.

Table 4.5 Composites of results (both viscous and inviscid) in the interior of the troposphere for the localized precipitation with  $P_0 = 60$  cm/day,  $x_0 = 10$  km, and the hypothetical domain = 200 km.

	Average		Range	
	Viscous	Inviscid	Viscous	Inviscid
u (m/s)	7.04	6.81	2 to 12	0.3 to 18
w (cm/s)	9.72	10.1	3 to 19	0.5 to 35
T (°C)	3.71	3.51	1 to 7	0.2 to 8
$(\rho w)_{\text{global}} (10^4 \text{ Pa})$	-9.5	-10.2	-1.2 to -22.6	-0.22 to -59

Table 4.6 Same as Table 4.5 but for the lower stratosphere. Note that the statistics shown here have not taken into account the possible wave breaking below the cloud top. See text for the definition of  $(\rho w)_{\text{global}}$ .

	M=200	M=400
GATE	-21.	-24.
Marshall Islands	-3.0	-3.1

Table 4.7  $(\rho w)_{\text{global}}$  (in  $10^4 \text{ Pa}$ ) for different values of the hypothetical domain (M). Two values of M (200 and 400 km), two profiles (GATE and Marshall Islands), together with  $c = -11 \text{ m/s}$  are used for the calculations. Cumulus friction is included.

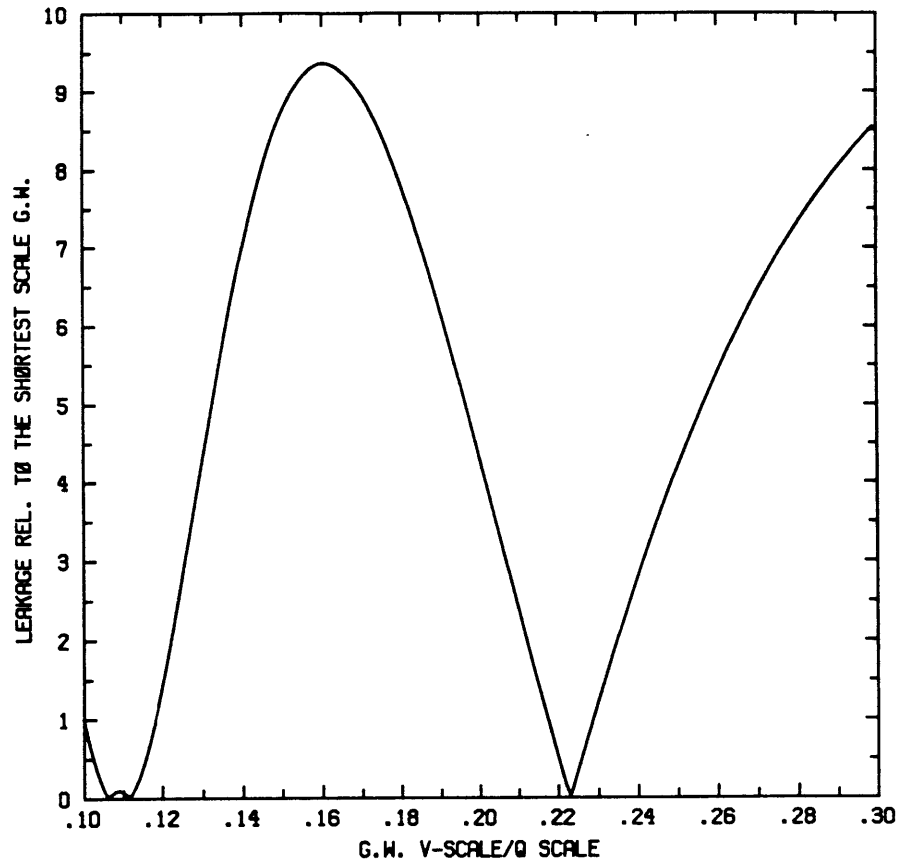


Figure A.1: Responses ( $w$ ) at the top of the domain for different vertical scales ( $L_z$ ) of the gravity wave. The domain of calculation is (0, 60 km). The thermal forcing is  $= \sin(\pi(z-2\text{km})/10\text{km})$  for  $z \in (2, 12 \text{ km})$ , and vanishes otherwise. The abscissa shows the ratio of  $L_z/10 \text{ km}$ . The ordinate shows responses relative to the case when  $L_z/10 \text{ km} = 0.1$  where the amplitude of the response is set arbitrarily to one. Radiation boundary condition is applied at the top, and no-slip boundary condition is applied at the bottom. Note that the wavelength of the gravity wave is defined as  $2\pi L_z$ .

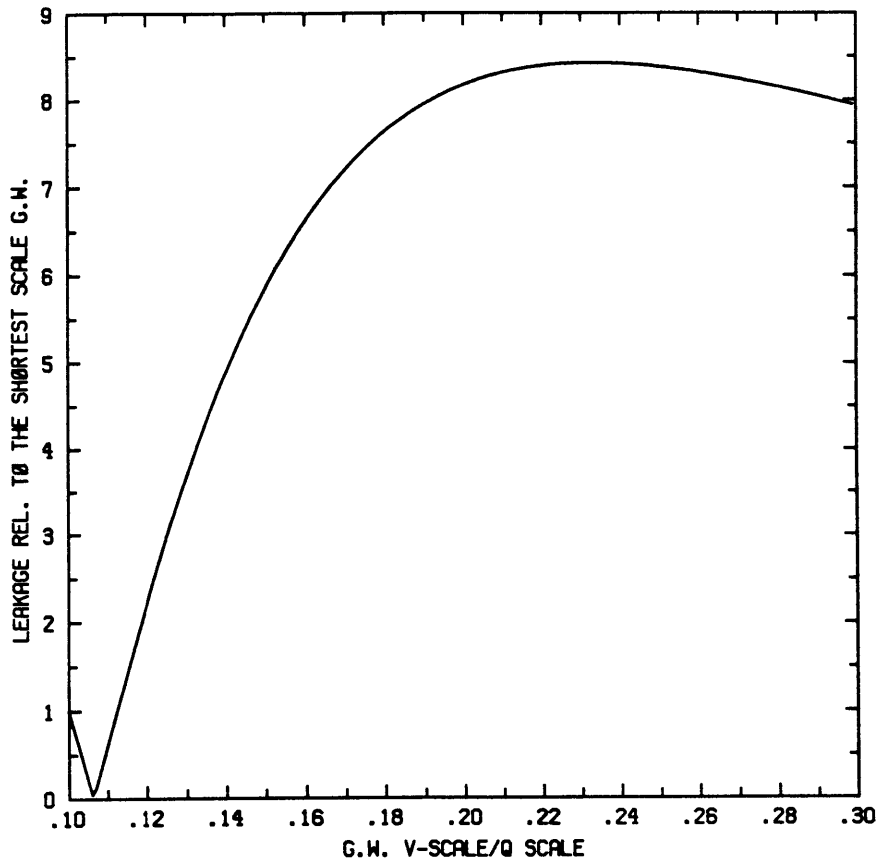


Figure A.2: Same as Figure A.1, except that radiation condition is also applied at the bottom.

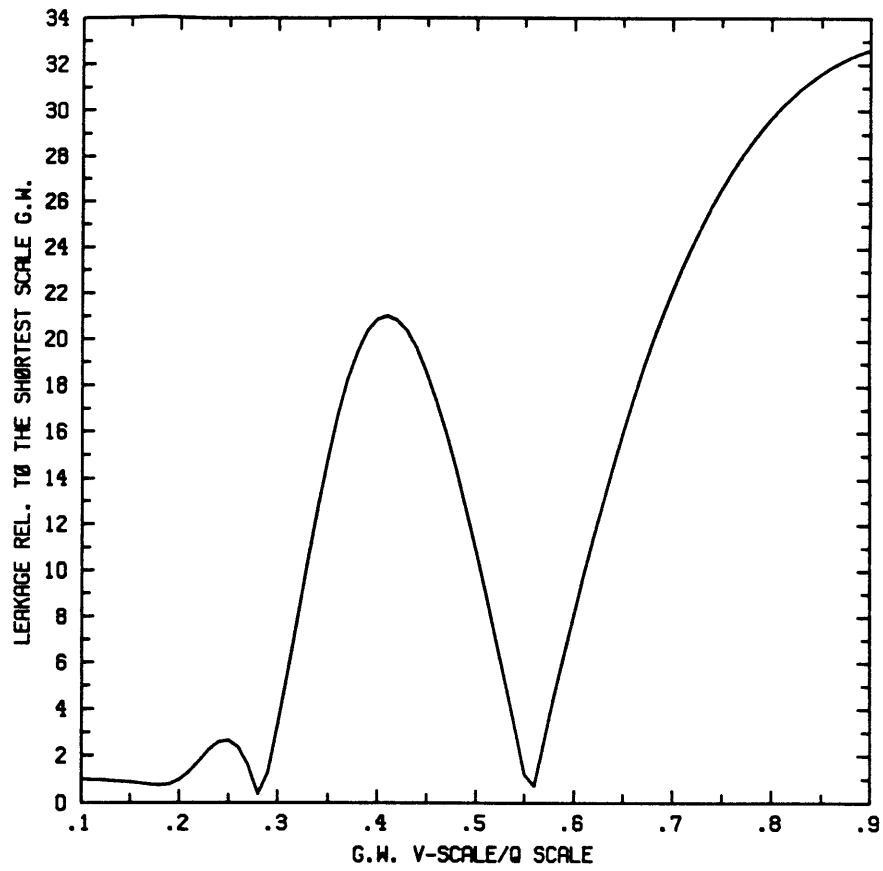


Figure A.3: Same as Figure A.1, except that the thermal forcing is  $= \exp(-((z-7\text{km})/4\text{km})^2)$ , and the abscissa shows the ratio of  $L_z/4 \text{ km}$ .

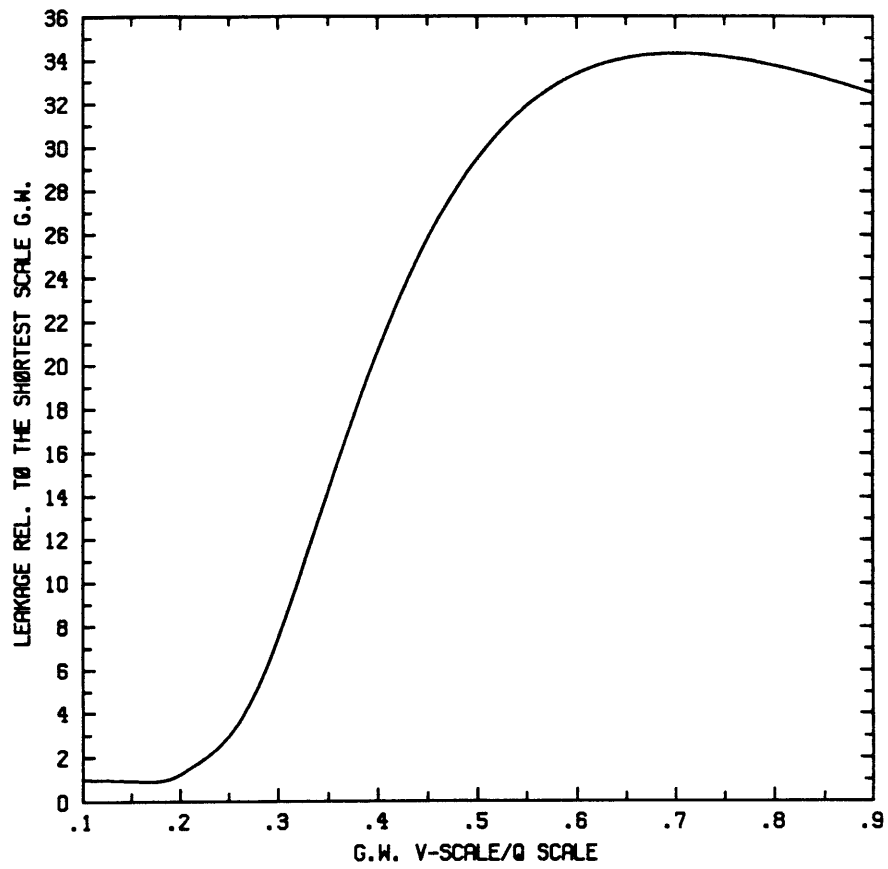


Figure A.4: Same as Figure A.3, except that radiation condition is applied at the bottom.

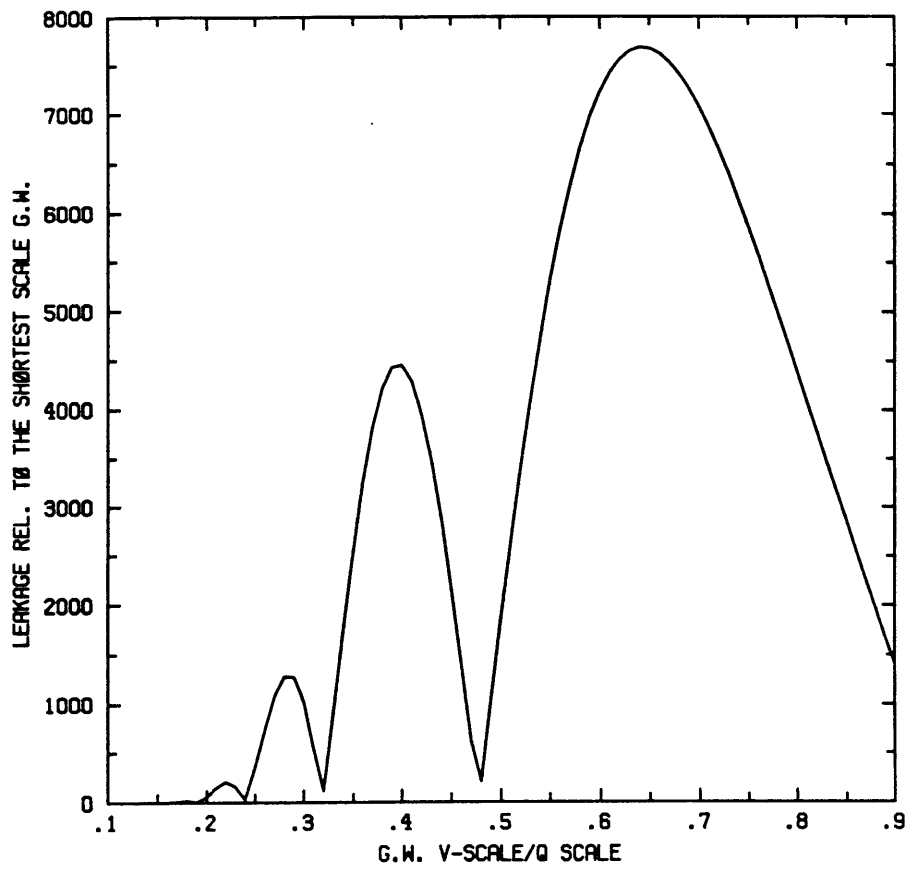


Figure A.5: Same as Figure A.3, except that the thermal forcing is  $= \exp(-((z-30\text{km})/10\text{km})^2)$ , and the abscissa shows the ratio of  $L_z/10 \text{ km}$

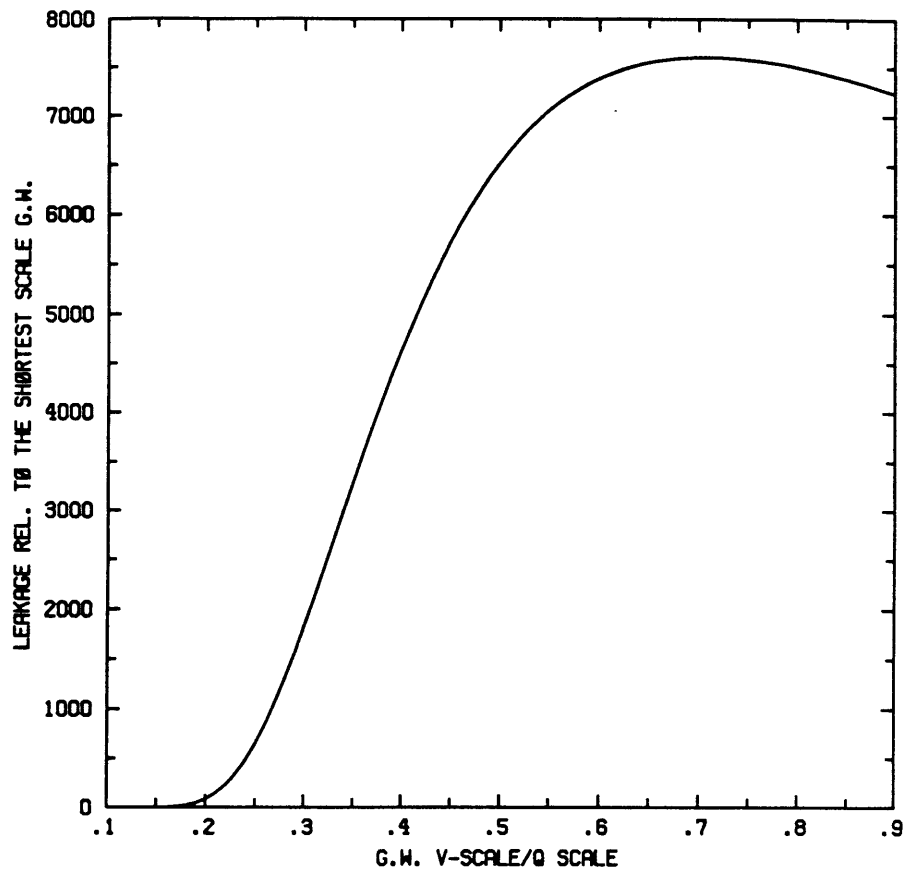


Figure A.6: Same as Figure A.5, except that radiation condition is applied at the bottom.